Technical Note 1970-20

The Millstone Hill Propagation Study: Progress in FY 1970

J. V. Evans
Editor

2 December 1970

Prepared for the Office of the Chief of Research and Development,
Department of the Army,
under Electronic Systems Division Contract F19628-70-C-0230 by

Lincoln Laboratory

MASSACHUSETTS INSTITUTE OF TECHNOLOGY

Lexington, Massachusetts

MASSACHUSETTS INSTITUTE OF TECHNOLOGY

LINCOLN LABORATORY

THE MILLSTONE HILL PROPAGATION STUDY: PROGRESS IN FY 1970

J. V. EVANS, Editor

Group 21

TECHNICAL NOTE 1970-20

2 DECEMBER 1970

LEXINGTON MASSACHUSETTS

The work reported in this document was performed at Lincoln Laboratory, a center for research operated by Massachusetts Institute of Technology. The work is sponsored by the Office of the Chief of Research and Development, Department of the Army; it is supported by the Advanced Ballistic Missile Defense Agency under Air Force Contract F19628-70-C-0230.

Abstract

This report summarizes the work carried out during the period 1 September 1969 through 31 August 1970 as part of the propagation studies being conducted jointly by the Bell Telephone Laboratories and the Lincoln Laboratory for the Advanced Ballistic Missile Defense Agency. These studies are centered on the Millstone Hill Field Station where an 84' fully steerable parabolic reflector is to be employed for simultaneous angle-of-arrival measurements of signals at UHF and L-band. These measurements are expected to permit refraction effects introduced by the auroral regions of the ionosphere to be investigated.

Work to date has largely been concerned with modifying the equipment in order to undertake the observations. A limited number of tracking observations have been carried out which yield useful measurements of angular scintillation. Additional measurements to study the extent and cause of auroral clutter have been undertaken. The Millstone Hill Thomson Scatter radar has also been employed to study F-region irregular behavior associated with auroral precipitation and the presence of Traveling Ionospheric Disturbances.

Accepted for the Air Force
Joseph R. Waterman, Lt. Col., USAF
Chief, Lincoln Laboratory Project Office

Contributors

D. E. Cunnold

J. V. Evans (editor)

A. Freed

T. Hagfors

J. L. Mann

J. M. Moran

R. J. Riley

M. L. Stone

CONTENTS

I. Introduction 1

II. Instrumentation 3

a) General 3

b) Frequency-Selective Subreflector 3

c) Servo System and Shaft Encoders 10

d) The UHF/VHF Receiver System 21

e) Interface Modifications 26

III. Refraction Studies 28

a) Calibration of the Antenna 28

b) Observations of Radio Star Scintillations 40

c) Satellite Tracking Experiments 42

IV. Auroral Studies 62

a) L-band Backscatter Measurements 62

b) Coordinated Satellite-Radar Observations 69

c) Theoretical Studies 83

V. Ionospheric Studies 86

a) Introduction 86

b) The Incoherent Scatter Radar 89

c) F Region Electron Density above Active Aurorae 91

d) Traveling Ionospheric Disturbances 94

Appendix A 106

I. Introduction

Defensive radar systems for detecting and locating ballistic missiles must be designed to combat the degradation in system performance that can result from tropospheric and ionospheric refraction effects, scintillation and clutter. These phenomena become increasingly severe at low elevation angles. At high latitudes there is a broad azimuthal sector where the effects are especially severe owing to the very irregular nature of the polar ionosphere and the presence of the aurora.

A program of measurements and data analysis is in progress, primarily centered at the Millstone Hill radar facility, that is designed to evaluate tropospheric and ionospheric effects on the capability of BMD radars operating at UHF, with emphasis upon disturbed ionospheric conditions (e.g., when radio aurorae exist). The work is being undertaken jointly by staff members of the Lincoln Laboratory and the Bell Telephone Laboratories. Currently the emphasis in these measurements is on attempting to separate and characterize the ionospheric and tropospheric components of refraction and scintillation. In order to do this, a UHF lobe-comparison satellite-beacon tracking capability has been added to the precise L-band tracking radar at Millstone. This permits simultaneous dual-frequency measurements of angle-of-arrival, amplitude and phase fluctuations for paths traversing the polar ionosphere as well as in other directions less subject to propagation effects.

A second major part of the program is concerned with determining the extent to which the aurora gives rise to interfering clutter echoes and, if possible, elucidating the relationship between the occurrence of aurorae and anomalous refraction effects. To this end some effort is being devoted to try to understand the physical mechanism responsible for auroral radar reflections. Accordingly, auroral radar reflections are being studied at L-band to determine their intensity as functions of Doppler shift and the orientation of the radar beam to the direction of the magnetic field.

The program outlined above has been described in some detail in an earlier Technical Note (TN1969-51, hereafter referenced as Evans 1969a). The present report provides a brief review of the work carried out during the period 1 September 1969 through 31 August 1970. Much of this period has been spent in developing the necessary instrumentation to make the measurements, and the section that follows summarizes this work. A limited number of refraction observations have been carried out employing radio stars and satellite-borne beacons, and these measurements are discussed in Section III. A number of auroral radar observations were undertaken during the year, and together with some theoretical studies on the mechanism for generating the radar aurora, these are presented in Section IV. The last section describes work being carried out as part of the program, using the Millstone Hill UHF incoherent scatter radar, to obtain ionospheric electron density profiles from which ionospheric refraction effects can be computed by ray-tracing.

II. Instrumentation

a) General

In order to carry out the work proposed earlier (Evans 1969a) it has been necessary to modify the antenna to permit simultaneous operation at two frequencies, and to improve the digital read-out and servo-system. In addition, a UHF beacon-tracking receiver system has been constructed and interconnected through the azimuth and elevation bearings of the antenna by cable-wraps which have been installed specifically for this purpose. The only particularly novel element in the system is the new frequency-selective subreflector. However, the accomplishment of all these changes represents a large fraction of the work carried out to date, and in addition, has controlled the rate with which new measurements can be undertaken. Accordingly, it seems worthwhile providing brief descriptions of some of the more important changes that have been made and these are presented in the following subsections.

b) The Frequency-Selective Subreflector

A key feature of the new instrumentation is the ability to perform simultaneous radar and beacon angular-tracking measurements from a single fully-steerable antenna. The radar measurements are carried out at L-band, using a 12-horn monopulse-feed located at the Cassegrainian focus of an 84' diameter parabola shown schematically in Fig. 1. The reception of satellite beacon signals at UHF is performed by a 4-element turnstyle-feed located at the Newtonian focus of the paraboloid. This arrangement is permitted by the use of a frequency-selective surface on the hyperboloidal subreflector of the Cassegrainian system. The subreflector is transparent to signals in the VHF and UHF bands but reflects at L-band. The antenna is shown in Fig. 2 together with the location of the frequency-selective subreflector and the L-band feed assembly.

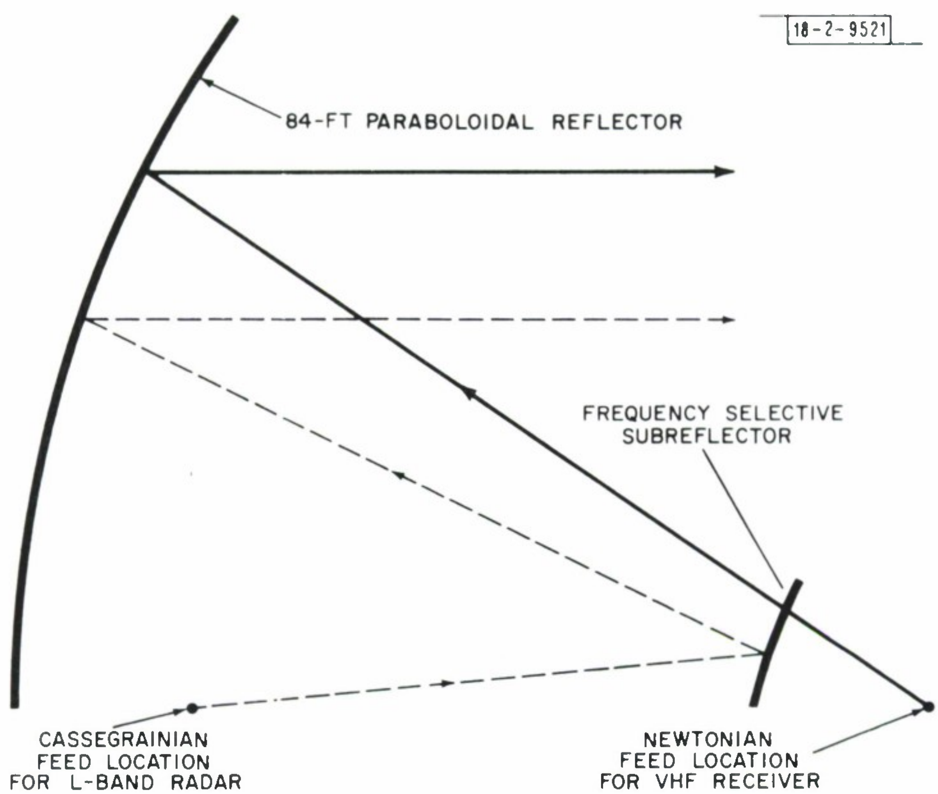

Fig. 1. Optical arrangement that permits Millstone Hill 84-foot parabolic reflector to be used at two frequencies simultaneously.

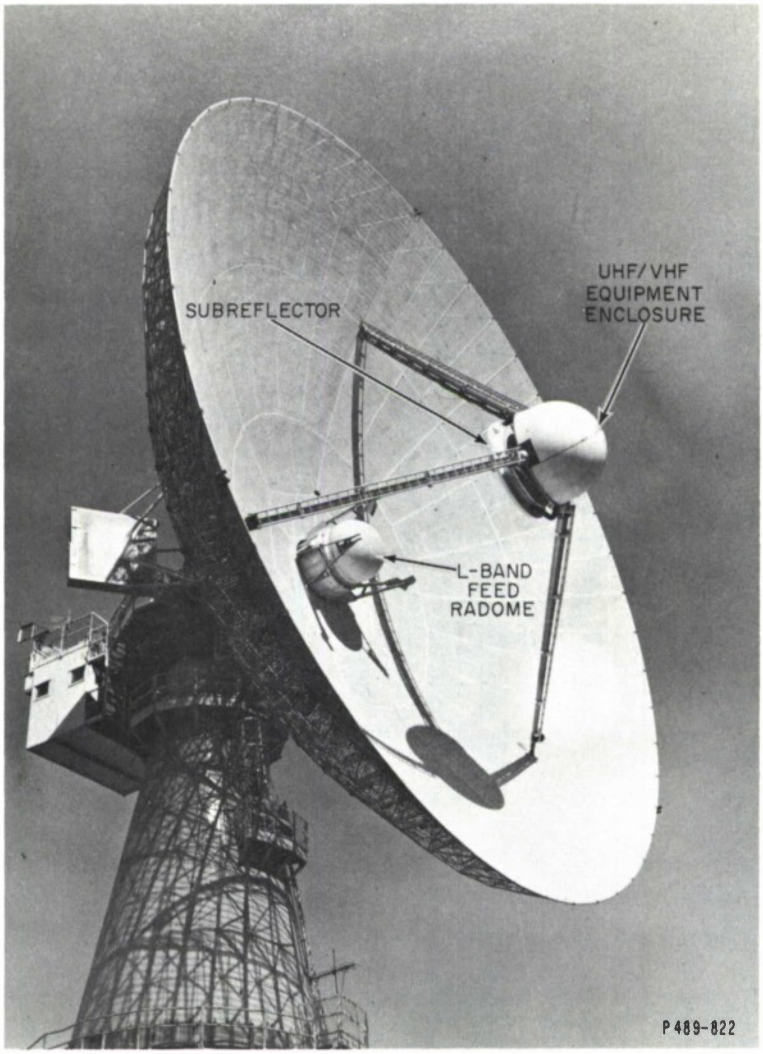

Fig. 2. View of Millstone Hill 84-foot parabolic reflector showing locations of L-band feed assembly, frequency-selective subreflector, and equipment shelter that houses UHF receiver preamplifiers and mixers.

The arrangement described above was chosen to permit the continued use of the 12 horn L-band tracking feed already installed on the Millstone antenna and provides the most efficient use of the antenna collecting area for receiving UHF beacon signals. The length of the dipoles required to form the reflecting surface is slightly less than a half-wavelength at the frequency which must be reflected, and these elements are spaced approximately at intervals of one-half wavelength.

The frequency-selective subreflector has the following properties:

1. Reflects radiation from an hyperboloidal surface at 1295 MHz.
2. Passes radiation at frequencies below 450 MHz with very little loss or phase distortion.
3. Withstands irradiation at a power density of approximately 3 kw per square foot produced by a 150 kw average power transmitter.

As originally designed it was planned to use thin etched-foil crosses embedded on the inside surface of an hyperboloidal plastic shell to form the frequency-selective subreflector. While this arrangement had worked satisfactorily in previous applications involving high peak power, the local dielectric heating which occurred when the surface was irradiated by a high average power source caused a catastrophic and irreversible failure of the dielectric. This would manifest itself as a breakdown along the air-dielectric interface between the tips of the dipoles. These deleterious effects were discovered during the evaluation of flat-plate replicas of the reflector in tests performed at Millstone Hill with the L-band transmitter connected to a standard gain horn. The design concept was modified to alleviate this problem; 1/8 inch thick crossed-dipole elements supported on insulated columns were used to form the reflecting surface. These air-insulated crossed-dipoles were free of voltage breakdown, and a complete subreflector was built and delivered to Millstone in late 1969 employing this form of construction. Unfortunately, the array configuration failed to produce an effective reflecting surface because

of an improper choice of element spacing. Thus the subreflector delivered by the vendor could not be used in operations requiring the full average power capability of the transmitter because the excessive leakage through the reflecting surface caused overheating of the materials mounted behind. This leakage was caused by the existence of grating lobes produced by the wide separation of elements which was thought to be necessary to prevent breakdown.

Subsequently, a successful frequency-selective surface was achieved using 9/16 inch thick crossed, cylindrical dipole elements arrayed with graded spacing of the center-to-center distance which decreases as a function of the radial distance away from the axis of the hyperboloid. This design is shown in Figures 3 and 4. A specimen array was successfully tested at 12 kw/ft^2, i.e., four times the rating required in the operating system. The graded spacing employed eliminated grating lobes and increased the number of dipoles per unit area with a corresponding decrease in the power reflected by each element. In tests of this specimen array, it was found that there was heating of the dielectric surface when the dipoles were mounted a distance of only $\lambda/4$ above it. In the construction of the final subreflector this dielectric stress in the hyperboloidal plastic shell was markedly reduced by supporting the scattering elements on half wavelength insulators. This successful subreflector was delivered in May 1970.

The UHF and VHF feeds are located behind the L-band resonant surface of the hyperboloid. Negligible transmission and scattering losses are produced at the lower frequencies by the presence of the frequency-selective array. The UHF feed consists of four turnstile elements in a diamond configuration. All four elements are combined to form the main beam illumination pattern; pairs of elements are combined to form the elevation and azimuth monopulse beams. A 'strip-line', hybrid network performs the arithmetic operations and simultaneously synthesizes two orthogonal polarizations. Tracking may be performed with either sense of circular polarization by connecting to the appropriate set of taps of the hybrid.

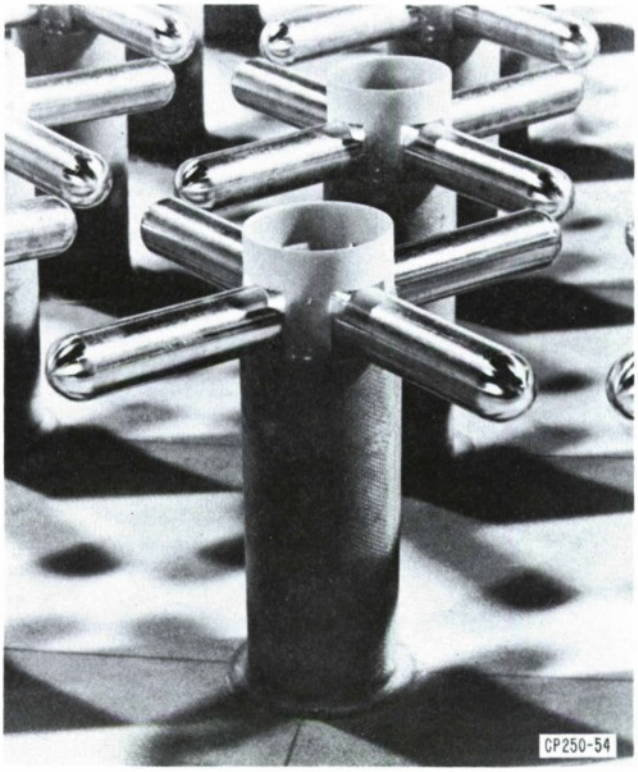

Fig. 3. View of some crossed half-wave dipoles employed in successful version of high-power subreflector. Stand-off insulators are half wave in length and serve to reduce currents induced in plastic subreflector surface.

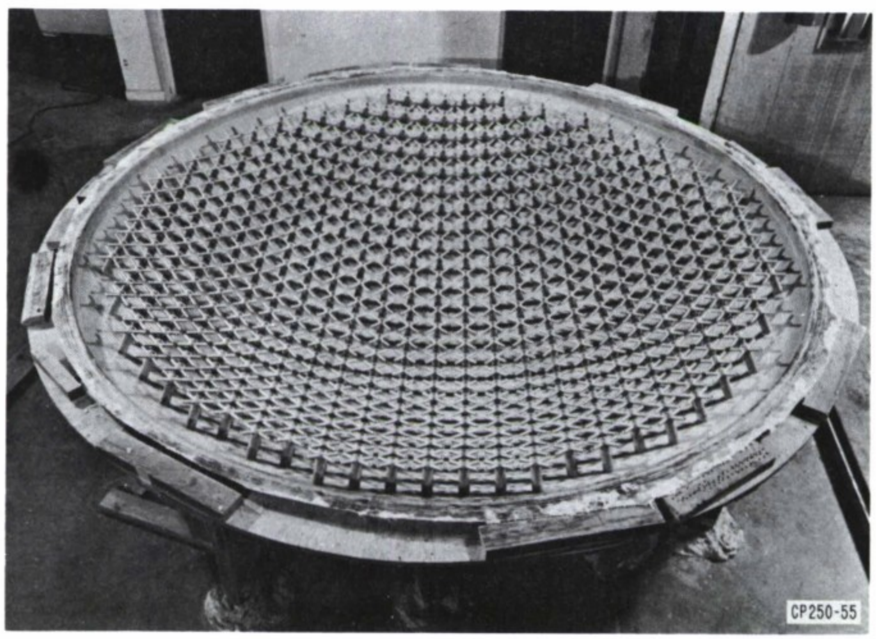

Fig. 4. View of interior lower face of frequency-selective subreflector showing location of all dipoles. Spacing of elements is least in center where power density is a maximum.

The VHF (150 MHz) receiving capability is provided by a loop antenna at the prime focus. This loop, which has a circumference of one wavelength, is supported a quarter wave above a metal ground plane. The loop provides one sense of linear polarization and is fed through a coaxial cable balun which provides a VSWR of about 1.2.

Primary patterns were taken on the VHF loop and the UHF monopulse dipoles by the vendor (Philco Ford Corporation). The principal effect of the loop on the UHF patterns was to broaden the sum pattern and decrease the monopulse null. The illumination of the main reflector provided by the loop is between 12 to 15 dB down at the edge. The VHF/UHF feed assembly is shown in Figure 5.

c) Servo System and Shaft Encoders

The basic servo control system for the Millstone Hill 84' antenna is shown in Figure 6. Position control can be effected in a number of ways via switch S1. For the connection shown in Figure 6 the demanded position and actual positions are compared via synchro units in which directly driven (1x) and geared up (36x) syncho-resolvers are employed.

As shown in Figure 7 the antenna is driven in each axis by a pair of D. C. motors via gear reducers providing a total reduction of 2230 in elevation and 2150 in azimuth. The current for the armatures of the D. C. motors is supplied by motor generator sets, whose field winding currents are governed by Silicon Control Rectifier (SCR) units. The SCR units are not linear but have a threshold which must be reached before they provide any output. By adjusting the thresholds to be slightly different, one of the drive motors can be made to be more effective than the other. By this means some counter-torque is introduced in the system which should serve to minimize the effects of play in the gears.

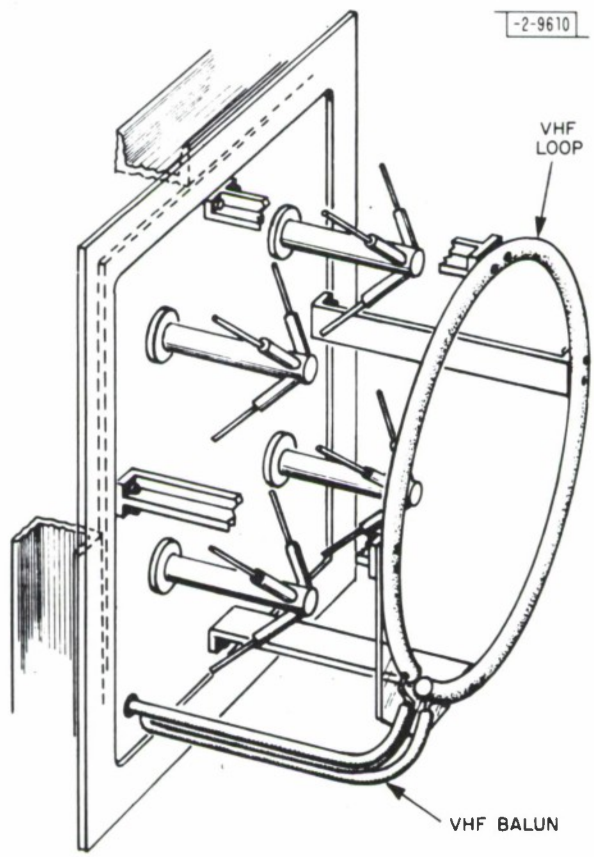

Fig. 5. View of UHF feed assembly employed with frequency-selective subreflector.

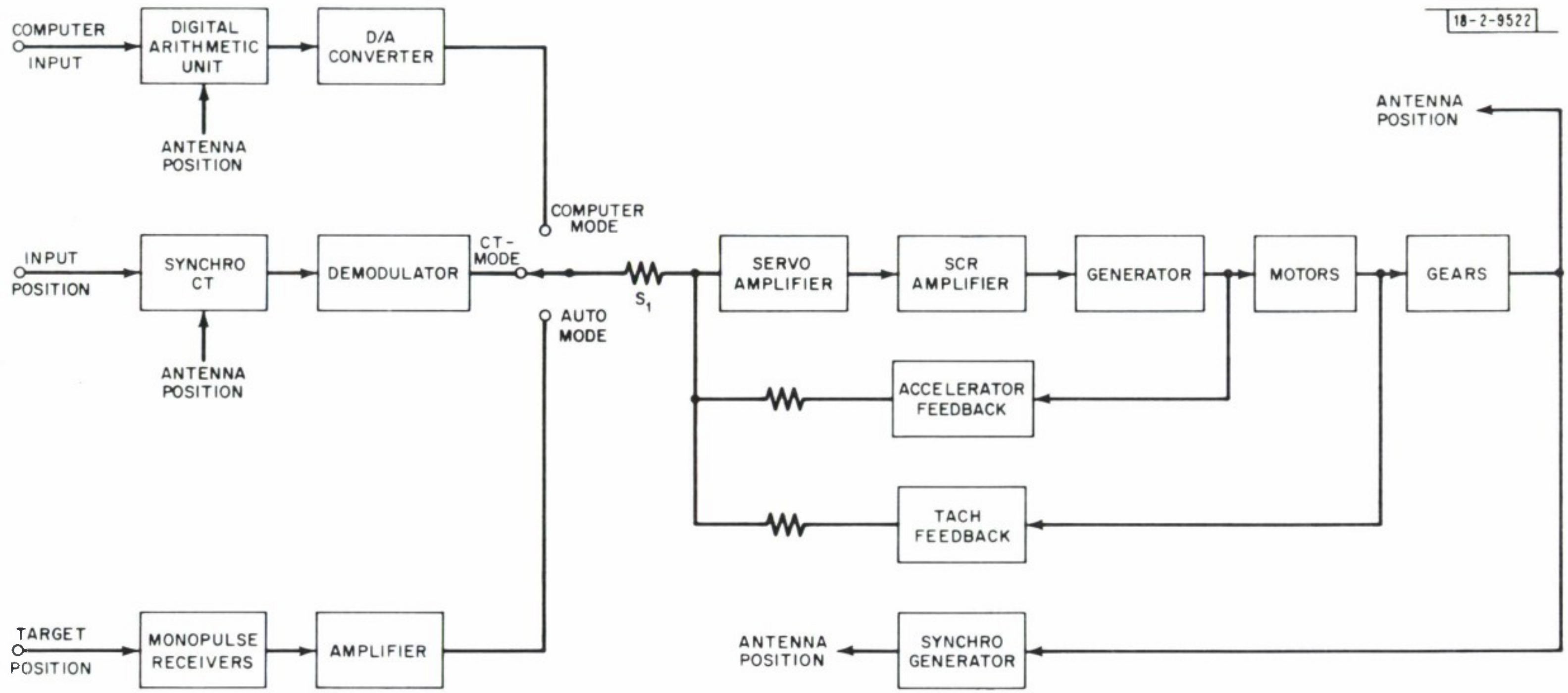

Fig. 6. Basic position servo-control system used to drive Millstone Hill antenna in both azimuth and elevation.

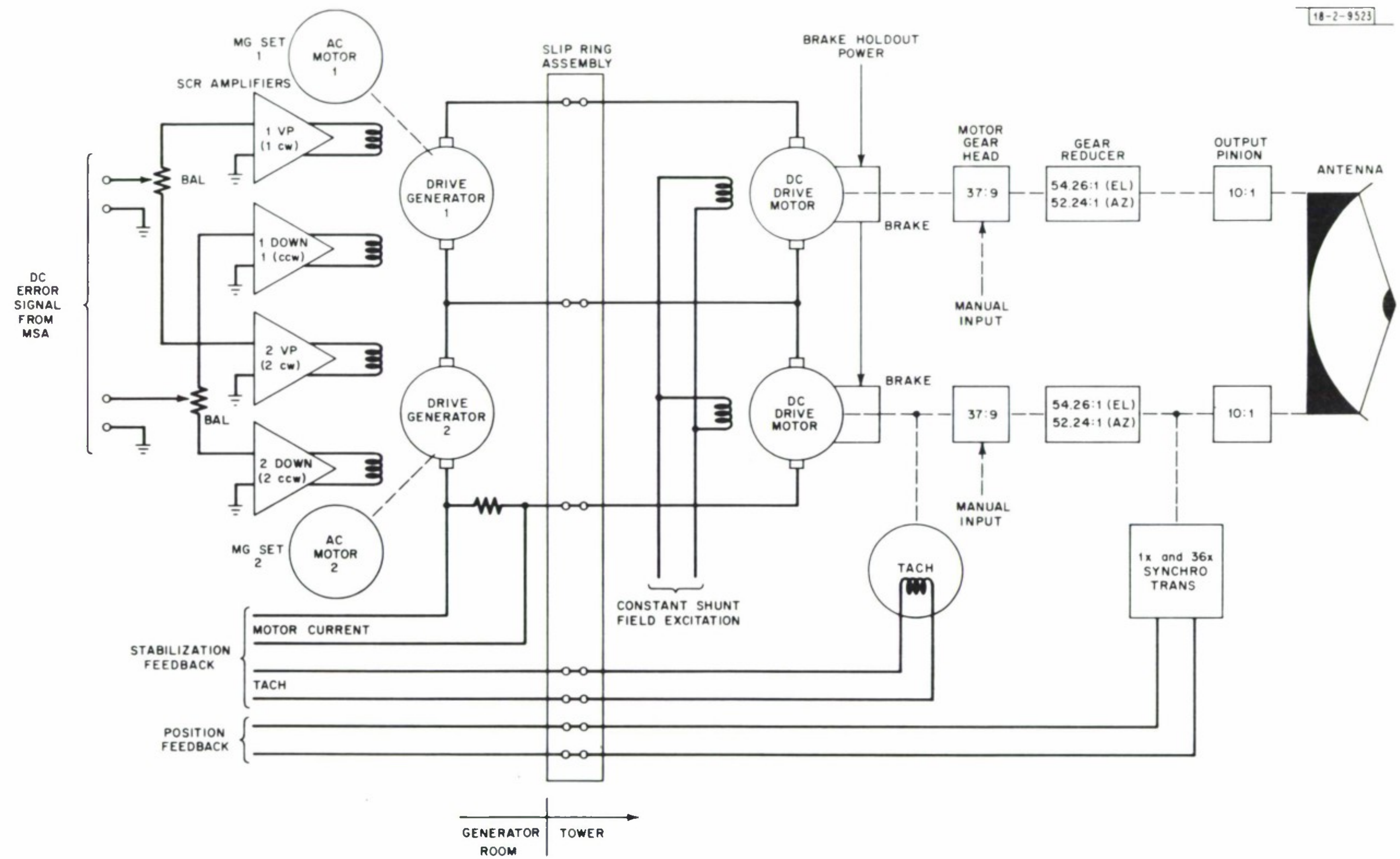

Fig. 7. Arrangement of DC motors, motor generators, and gear reducers employed to drive Millstone Hill antenna prior to modification.

This scheme has serious drawbacks in that small transients are introduced in the motion by the turn-on and turn-off of the SCR units. More seriously since the SCR units are not push-pull only a single field winding in each motor generator is energized at any one time, and hence the counter-torque applied can be different in the two directions. In addition, the threshold settings on the SCR units could not be held constant so that the amount of counter-torque applied would vary with time, causing the overall response of the servo to be different from day-to-day. Further, because of coupling between the windings the amount of counter-torque also varied with the value of the demanded torque.

These problems have all been remedied in the new system, which is shown in Figure 8. The four SCR units have been replaced by two 1 kw solid-state D.C. amplifiers which have the advantage of greater stability, linearity, and of providing a positive or negative output. One amplifier is used to drive one field winding on each motor generator in response to the position error voltage. The second amplifier is used to establish the amount of counter-torque. This is accomplished by driving a current through the remaining pair of field windings in opposite directions. The value of the counter-torque current so produced ($\sim$ 40 amps) is sensed by including a small series resistor R in the return path for both motors. The voltage appearing across this resistor is compared with a fixed applied voltage V at the input to the D.C. amplifier. This arrangement largely eliminates the effects of coupling between windings and ensures that counter-torque is always applied (until the total drive current exceeds 40 amps).

These improvements have made it possible to increase the gain of the servo amplifier (Figure 6) without introducing oscillations of the antenna. As a result the variable gain adjustments on the servo amplifiers have been removed and day-to-day changes can no longer be made by the operators.

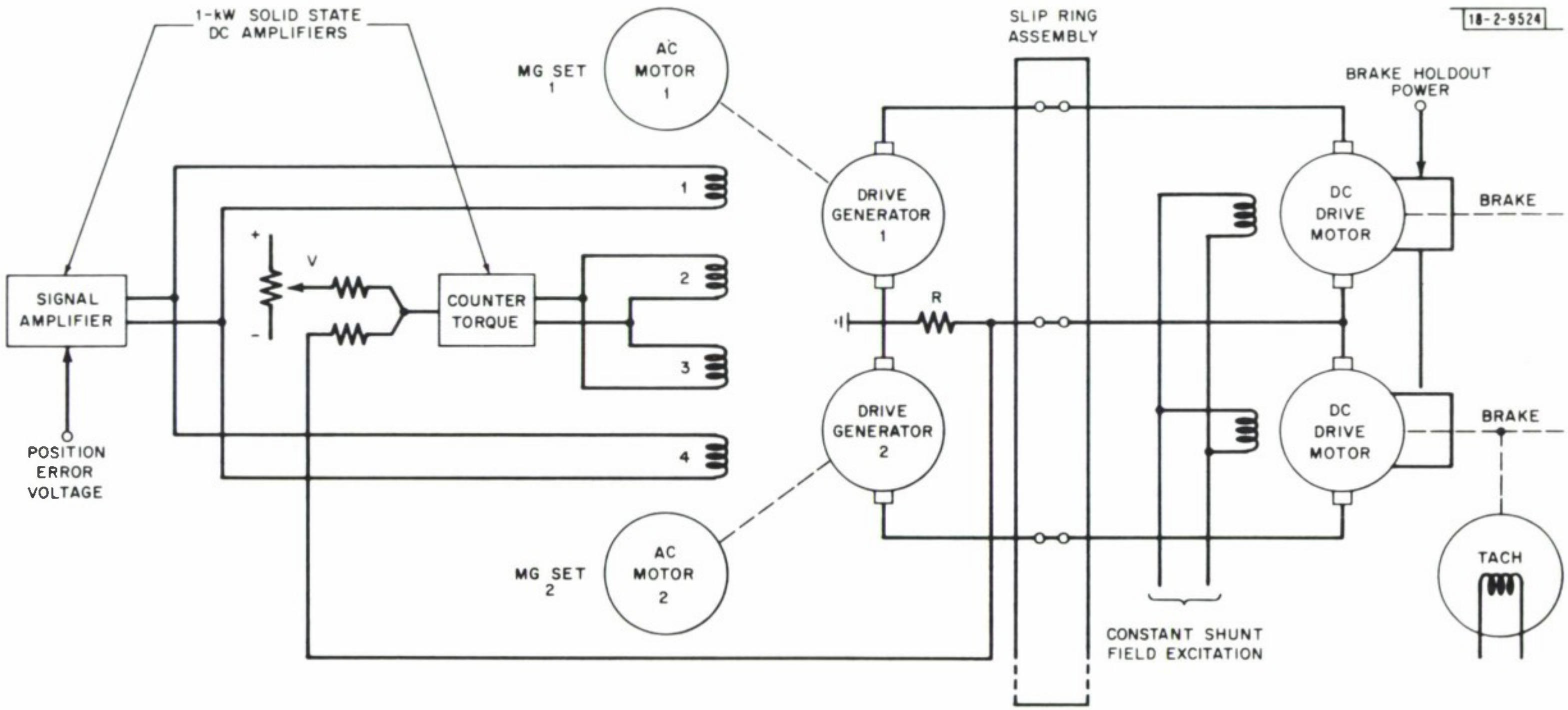

Fig. 8. Arrangement of DC motor generators and drive motors following modifications described in text.

To obtain a digital estimate of the antenna position a synchro-repeater is employed to drive a 13-bit digital shaft-encoder via a 1:4 gear box as shown in Figure 9. This gives the equivalent of 15-bit digital encoding, and makes the least significant bit correspond to 0.011° of antenna rotation in either axis. Unfortunately, as can be seen in Figure 7 the synchro-transmitters do not sense the positions of the antenna shafts, but rather the positions of shafts of the final pinion drive gears. Further, a similar 10:1 gear box must be used to drive the synchro-transmitter. Thus, play in the gears together with any error introduced by the inability of the synchro-repeater to accurately follow the transmitter adds uncertainty to the true antenna positions.

To improve the determination of the antenna position new 17-bit digital encoders (giving 0.003° resolution) have been connected directly to measure the antenna shaft positions. For the elevation axis this was accomplished by connecting a 'spider' inside the elevation axis torque-tube which drives a shaft coupled to the encoder. The determination of the azimuth position presented considerably more difficulty owing to the fact that the region along the azimuth axis in the vicinity of the bearing is occupied by the waveguide rotary joint, slip rings and R.F. 'choke' joints. Thus, there is no way in which the encoder can be placed on the azimuth axis of the antenna. This problem has been overcome in a novel manner through the use of a cam-follower arrangement developed by Lincoln Laboratory engineers.

A plan view of the cam-follower system is shown in Figure 10. The cam consists of an octagon, attached to the rotating structure at the level of the bearing, comprised of eight metal rails that are flat

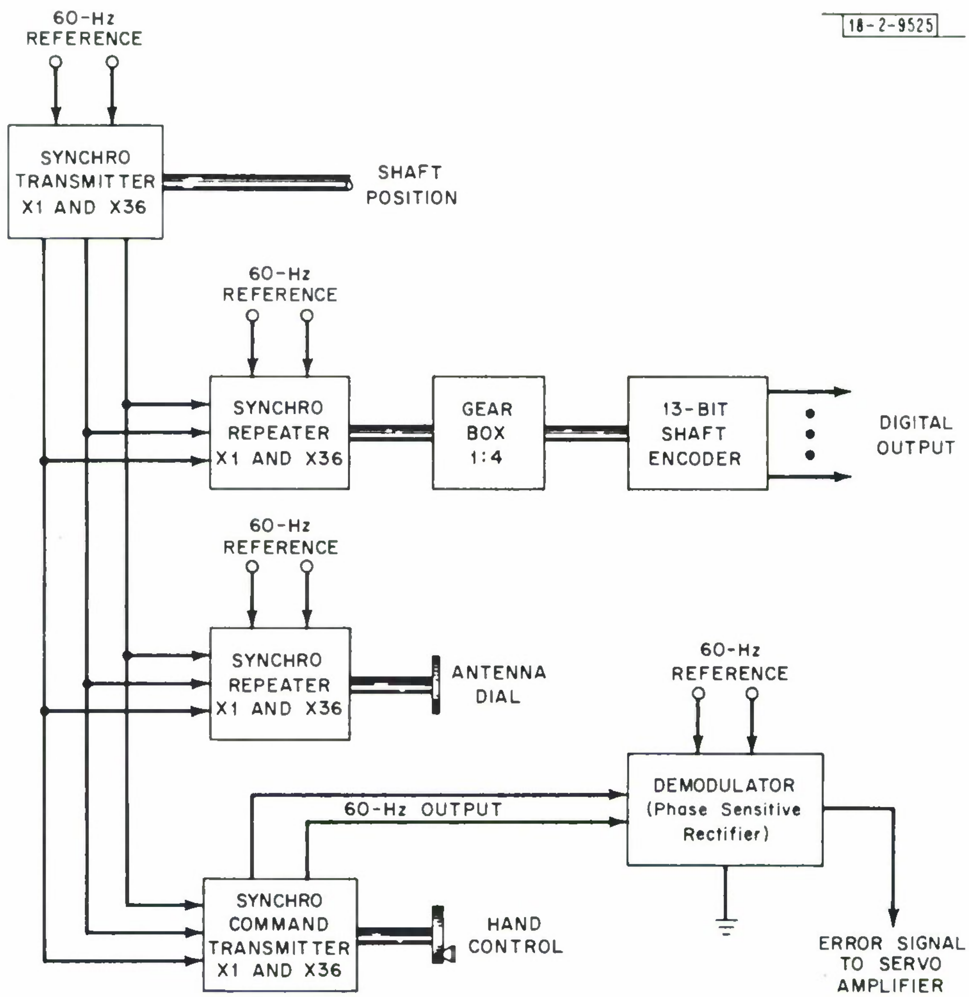

Fig. 9. Arrangement of synchro-repeaters for presenting antenna shaft positions to computer and operators prior to modifications described in text.

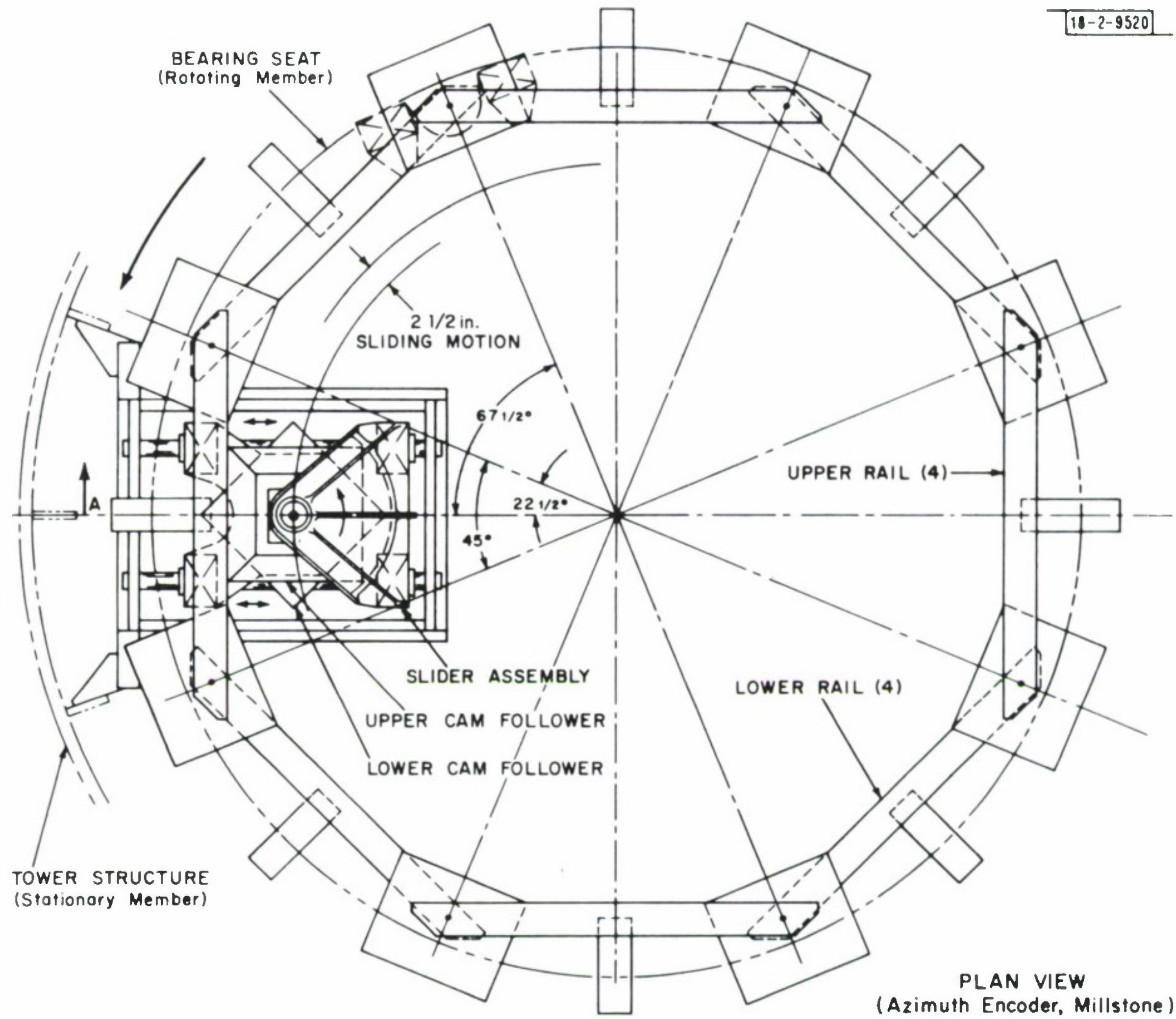

Fig. 10. Plan view of azimuth encoder cam-follower arrangement employed now to measure bearing of antenna.

to 10^{-3} milliradian. The rails are mounted alternately above and below each other so that no true corners are produced where they meet. The angle included by any pair of rails may be changed by micrometer adjustment to be exactly 135°.

The follower unit, shown in Figure 11, is attached to the antenna tower and consists of a smaller rotating octagon held in contact with the large fixed one. This arrangement produces one rotation of the shaft of the small octagon for a complete revolution of the antenna, and thus the digital encoder can be coupled directly to the follower shaft. In order to allow for the sideways motion of the follower the entire assembly is free to move laterally along two cylindrical rails on roller races. A metal tensioning spring pulls the assembly forward to keep the two sliding surfaces in contact at all times.

In order to check the accuracy of this arrangement tests were carried out in which the system was supported on a rotating, air-bearing table with a second identical shaft-encoder mounted on the table axis. A digital comparison of the two encoders, one driven directly and the other through the coupling, provided an indication of the accuracy of the coupling, backlash and other effects. The two encoder readings were compared automatically for every encoder position and the results plotted. It was found that some of the rails were distorted and required regrinding. After the grinding process, the encoders agreed to within 2 angular increments. This is the maximum resolution of the measurement technique, and indicates that the coupling properly reproduces the angular position of the bearing. These measurements were made with both forward and reverse motion of the bearing in order to detect any backlash effects; other than a one count shift introduced by the measurement system none could be detected.

Additional tests were made as the coupling passed through corners where the cam-follower transfer from one rail to the next. At a rotation

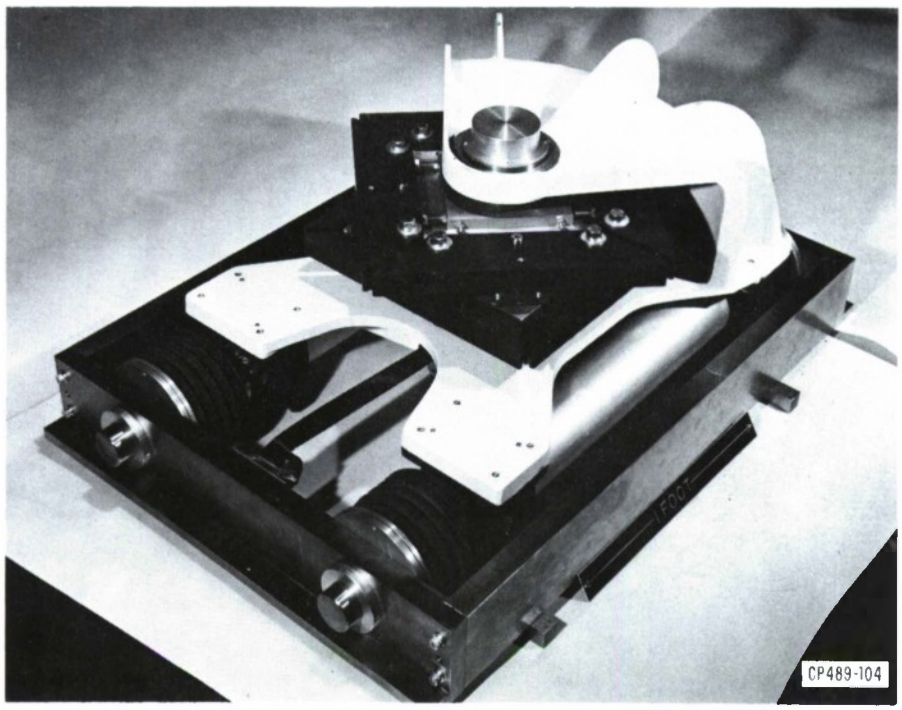

Fig. 11. View of azimuth encoder cam-follower assembly. This unit comprises two square cams arranged at 45° to one another and free to move laterally on a pair of rails through roller races. (Bellows in picture cover rails and serve to keep them clean.) One side of square cams is always held in contact with one rail of an octagonal set of rails (Fig. 10).

speed comparable to normal antenna tracking rates (1°/sec) no irregularities were encountered. However, when the rotation rate was raised to 3°/sec a 2-4 count error was generated as the corners were traversed.

These new encoders allow the computer to direct the antenna with considerably greater accuracy than previously. In addition, the absolute position of the antenna when operating in the closed-loop track mode (Figure 6) is now better determined, and consequently the true position of a target is also more accurately known since it is determined by converting the receiver error voltage to an angular offset that is added to the digitally-encoded position.

d) The UHF/VHF Receiver System

The installation at the Millstone Hill Radar facility of a UHF/VHF receiver system for use in the refraction measurements program has been completed. Simplified block diagrams of the receiver system and its interconnection with the L-band radar, antenna control, and data processing are shown in Figures 12 and 13. Table 1 summarizes the characteristics of these receivers.

The UHF monopulse receiver is used for multi-frequency observations of the Navy Transit series of satellites. These orbiting satellites transmit on two phase-related frequencies near 400 MHz and 150 MHz. The passive UHF measurements together with the L-band radar measurements (1295 MHz) yield simultaneous angle-of-arrival and amplitude scintillation observations as discussed in Section III-c) of this report. The UHF and VHF receivers are used for dispersive Doppler experiments that are also discussed in Section III-c). The UHF receiver has been modified to permit monopulse error tracking (MOPET) of certain radio stars as a means of calibrating the pointing of the Millstone antenna system. This calibration technique is discussed in Section III-a).

The RF sections of the receivers are housed in an environmental enclosure located at the apex of the 84-foot diameter dish antenna (Figure 2). Four crossed-dipole UHF feeds and a comparator-polarizer unit installed

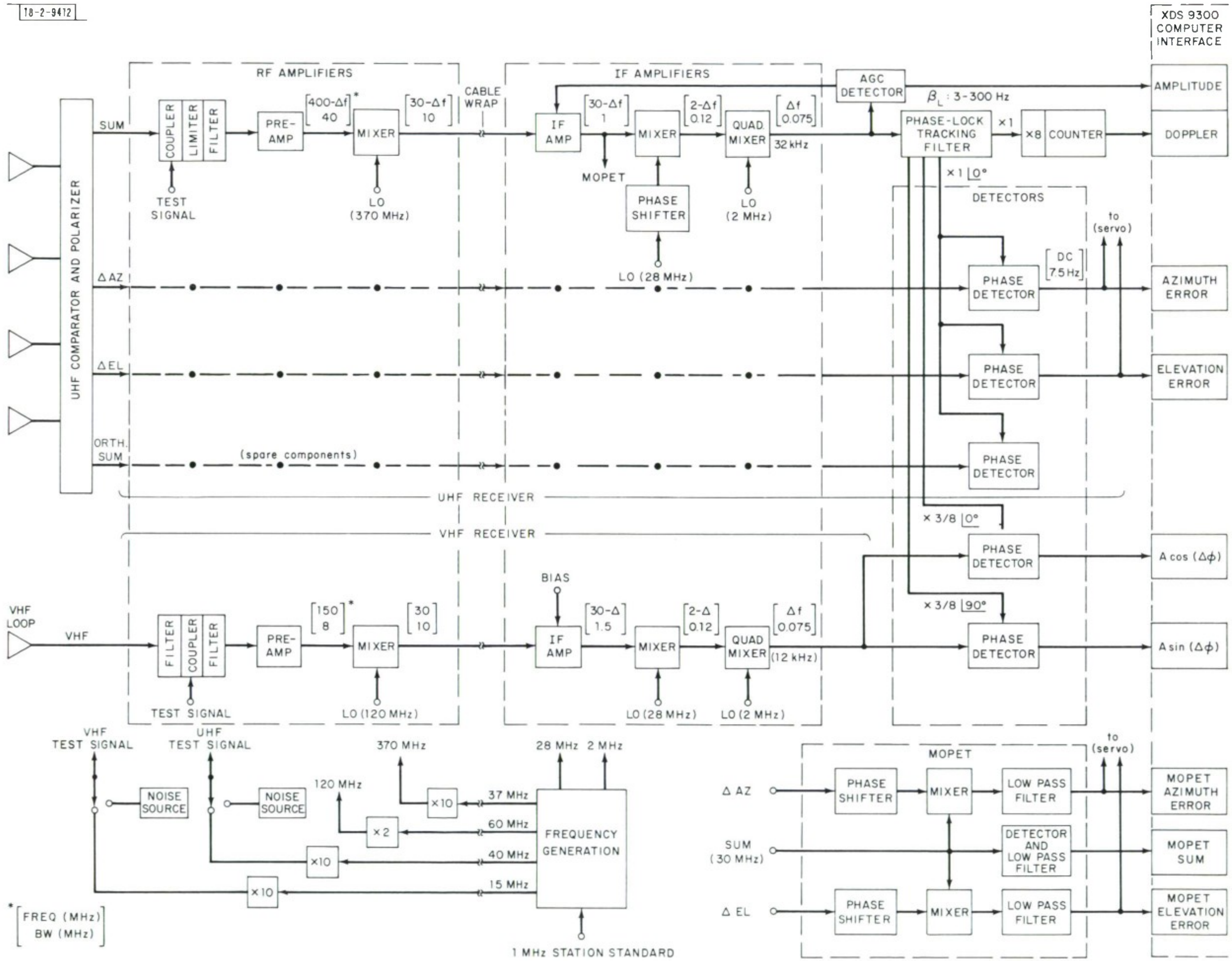

Fig. 12. Block diagram of UHF/VHF receiver system as assembled.

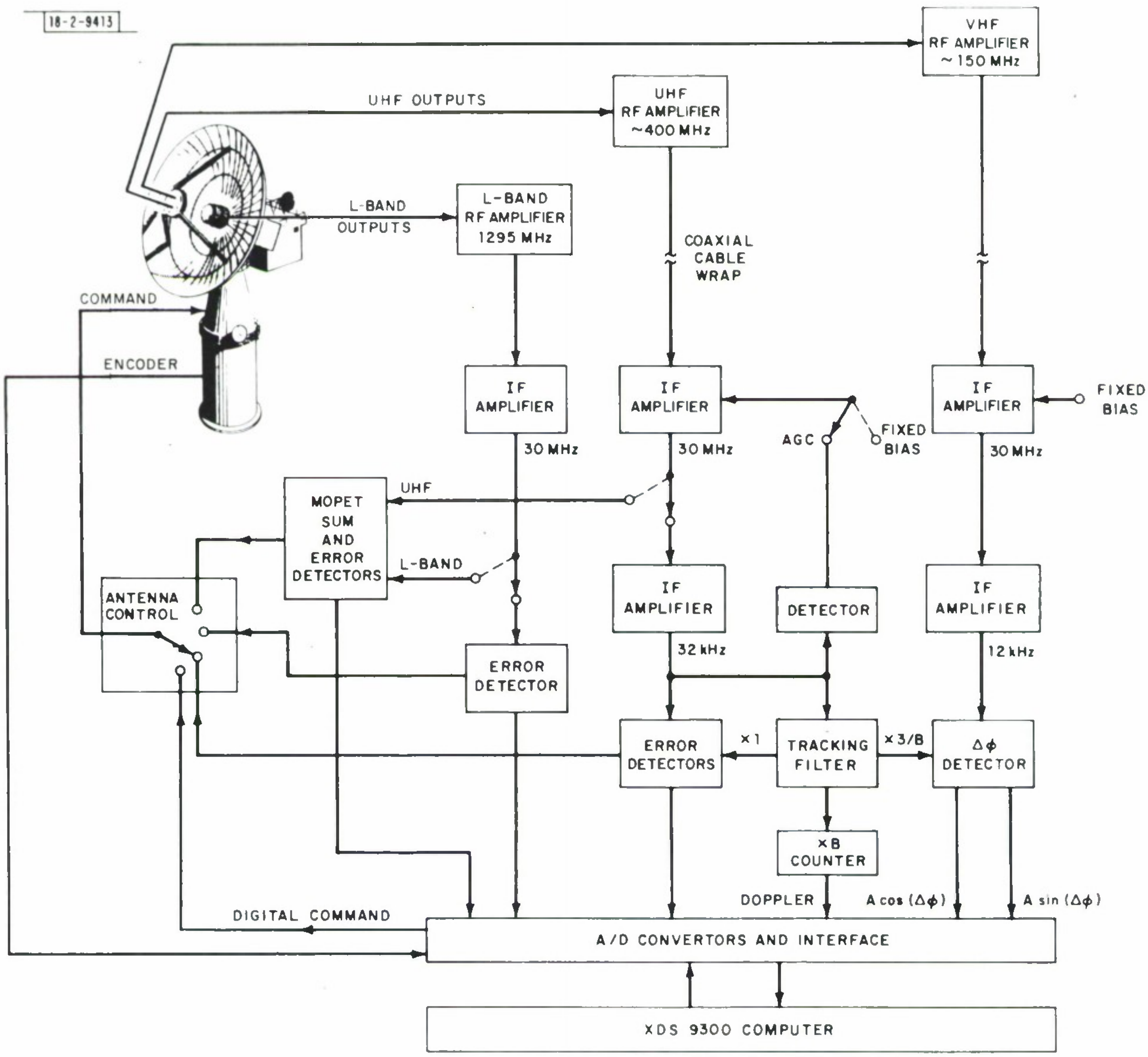

Fig. 13. Diagram showing various options for controlling antenna position.

	UHF	VHF
Frequency	400 MHz	150 MHz
System Temperature	$390^{\circ}K$	$500^{\circ}K$
Antenna		
Collecting Area	~200 m^2	-
Gain	~37 dB	-
Beamwidth	2.6°	5.6°
Feed	4-cross dipole (monopulse)	Loop
Polarization	Circular	Linear
RF Receiver		
Gain	47 dB	47 dB
Bandwidth (RF)	40 MHz	1.5 MHz (preselector)
Bandwidth (30 MHz)	10 MHz	10 MHz
Dynamic Range	60 dB	60 dB
IF Receiver		
Gain (sat. track mode)	Variable (AGC)	Fixed
Gain (MOPET)	Fixed	NA
Dynamic Range	50 dB(AGC)	50 dB
AGC Time Constant	.1 - .2 sec	NA
Bandwidth (30 MHz)	1 MHz	1.5 MHz
Bandwidth (2 MHz)	120 kHz	120 kHz
Nominal Final Frequency	32 kHz	12 kHz
Low-Pass Filter Bandwidth	75 kHz	75 kHz
Detector		
Post-Detection Bandwidth	7.5 Hz	7.5 Hz
Off-Axis Error	.125 volt/min	NA
Tracking Filter		
Loop Bandwidth (B_L)	3-300 Hz	NA
Loop Order	3rd	NA
Max Slew rate	B_L	NA

Table 1 Summary of UHF/VHF Receiver Characteristics

behind the FSS provide the circularly polarized monopulse signals to the UHF receiver system. A linearly polarized VHF signal is obtained from a loop antenna feed which is also mounted behind the FSS. The RF signals are amplified by a low-noise solid-state preamplifiers, converted to 30 MHz, and transferred via coaxial cable to the main receiver room where the IF amplifiers are located. The first local oscillator frequency of the UHF receiver is derived from a frequency synthesizer and may be adjusted to allow reception of RF signals within a band 20 MHz wide centered at 400 MHz. Provision for inserting known test signals and a calibrated noise source has been made for test and calibration purposes. The nominal noise figure of the UHF receiver channels is 3.7 dB, while at VHF the nominal noise figure is 4.5 dB.

The beacon transmitter frequencies of the Navy Transit satellites are offset by 80 parts per million. The 30 MHz IF signal is converted down to the offset frequency (32 kHz at UHF - 12 kHz at VHF) in two steps. The final IF signal in the 'sum' channel of the UHF receiver is detected, amplified, and distributed to the IF amplifiers in all the receivers as an AGC voltage. In this way the error channel signal voltages are normalized with respect to the signal level in the 'sum' channel. The 'sum' channel final IF signal is also employed as input to a 3rd-order phase-lock tracking-filter which has selectable loop bandwidths of 3-300 Hz. The locked- oscillator output of the tracking filter is then taken as the reference signal to the phase detectors employed in the azimuth and elevation error channels. After low-pass filtering (7.5 Hz) and D.C. amplification, the error voltages and the AGC (signal strength) voltage are routed to the A/D converters of the XDS9300 computer interface equipment. The monopulse error voltages are also sent to the antenna servo control equipment to permit the option of closed-loop tracking (Fig. 13). The Doppler frequency obtained from the tracking filter is amplified by a frequency counter whose output is also transferred into the XDS computer [Sec. e) below].

For the purpose of carrying out the dispersive Doppler experiment, the locked-oscillator output of the tracking-filter is multiplied by 3/8 and this signal is then used as the reference signal for the phase detectors connected to the output of the VHF IF amplifier. The resultant outputs of these phase-detectors are low-pass filtered and amplified to provide the real and imaginary components of the UHF/VHF differential phase; these are also routed to the XDS 9300 interface equipment for data processing.

In the MOPET mode of operation, Sec. IIIa) the UHF receiver is run with the 30 MHz IF amplifiers operated at fixed gain. These amplifiers are then employed to drive wide-band phase-detectors which are followed by RC filters (τ = .2 sec) to provide the MOPET error voltages. The sum signal in the 30 MHz IF channel is detected and filtered to provide a record of the signal amplitude. The error voltages generated in the MOPET system are routed to the computer for data processing, and are available at the selector switch for the servo control system to permit automatic tracking of the radio star if desired.

e) Interface Modifications

Significant changes to the previous radar/computer interface equipment were required in order to provide a dual-frequency tracking capability (L-band active/UHF passive) complete with real-time computer-steering functions and recording of all raw track data. The augmented L-band data transfer now includes UHF monopulse error signals, UHF sum-channel AGC voltage, UHF Doppler shift count, and also the differential phase between the received UHF and VHF beacon signals.

Following a number of tracking exercises, using only UHF beacon signals, it was found that the Doppler measuring system as originally implemented was inadequate, and thus the system was changed so that the Doppler frequency is multiplied by a factor of four before being applied to the frequency counter. In addition the counting scheme was changed to sense all zero-crossings. Doppler resolution to the nearest one-eight cycle is now

obtained over each counting interval which for convenience is made equal to the L-band interpulse period. UHF range-rate resolution of less than two meters per second within a single interpulse period (1/15th second) is thus achieved.

Included in the new system are antenna control indicators to register the tracking mode in use, and provisions have been made to permit the computer to control the L-band radar range-gate and coarse Doppler setting. A specially developed software package is employed for recording raw data, providing in real-time an orbit-fit to the processed data, and transmitting steering commands from predictions so generated (Section IIIc).

Extensive interface modifications have also been carried out to accommodate the data transfer requirements of the new two-pulse ionospheric scatter and auroral scatter measurements (Sec. IV and Sec. V).

III. Refraction Studies

a) Calibration of the Antenna

i) Method

An automated procedure for calibrating the offsets between the nulls in the L-band and UHF error patterns has been developed and is known as MOno Pulse Error Tracking (MOPET). For these measurements the receiver is operated in the manner described in Sec. IId) and illustrated in Figure 14. The antenna is placed under the control of the XDS computer which commands it to follow the known position of one of a number of bright celestial radio sources having small angular diameter (usually Cassiopeia A or Cygnus A). The computer then superimposes on this sidereal motion a scan in either azimuth or elevation. The width of the scan is 12° and usually an elevation scan is carried out first followed by a scan in azimuth. The output of the sum channel and phase detected error voltages along with the shaft encoder positions are read into the computer every 0.1 second. Figure 15 shows the receiver outputs for a typical sequence of scans.

The apparent position of the source can be determined either by examining the sum or the difference channels. Since the difference channel yields greater accuracy the latter has been chosen as the reference, and the radio source is taken to be on axis when the error voltage goes through zero. In order to determine this point the samples of the receiver voltage are sorted according to the angular distance of the antenna (as indicated by the shaft encoders) from the computed position of the source. Each $.011^{\circ}$ interval over the 12° scan is tested separately and all receiver voltage samples taken within each interval are averaged. In this way, the results do not depend on how well or how quickly the antenna follows the computer commands.

The zero voltage point is determined in the manner illustrated in Figure 16. A straight line fitted to the two portions of the scan where the source is well outside the beam is used to establish the baseline of the phase detector outputs and serves to remove effects due to D.C. offsets in the amplifiers. A second straight line is then fitted to the center portion of

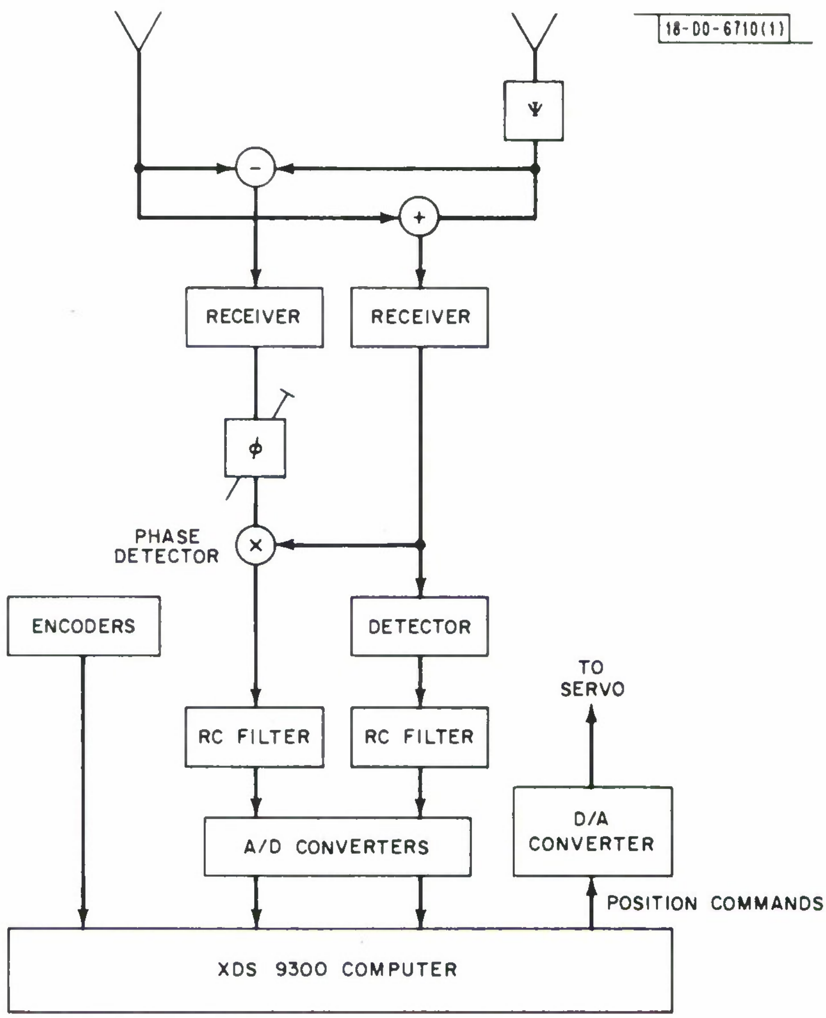

Fig. 14. Diagram showing manner in which sum channel and error channel signals are developed in UHF receiver system. Ψ is an unwanted phase error that may be present on one side of feed assembly due, for example, to cables that are of unequal electrical length.

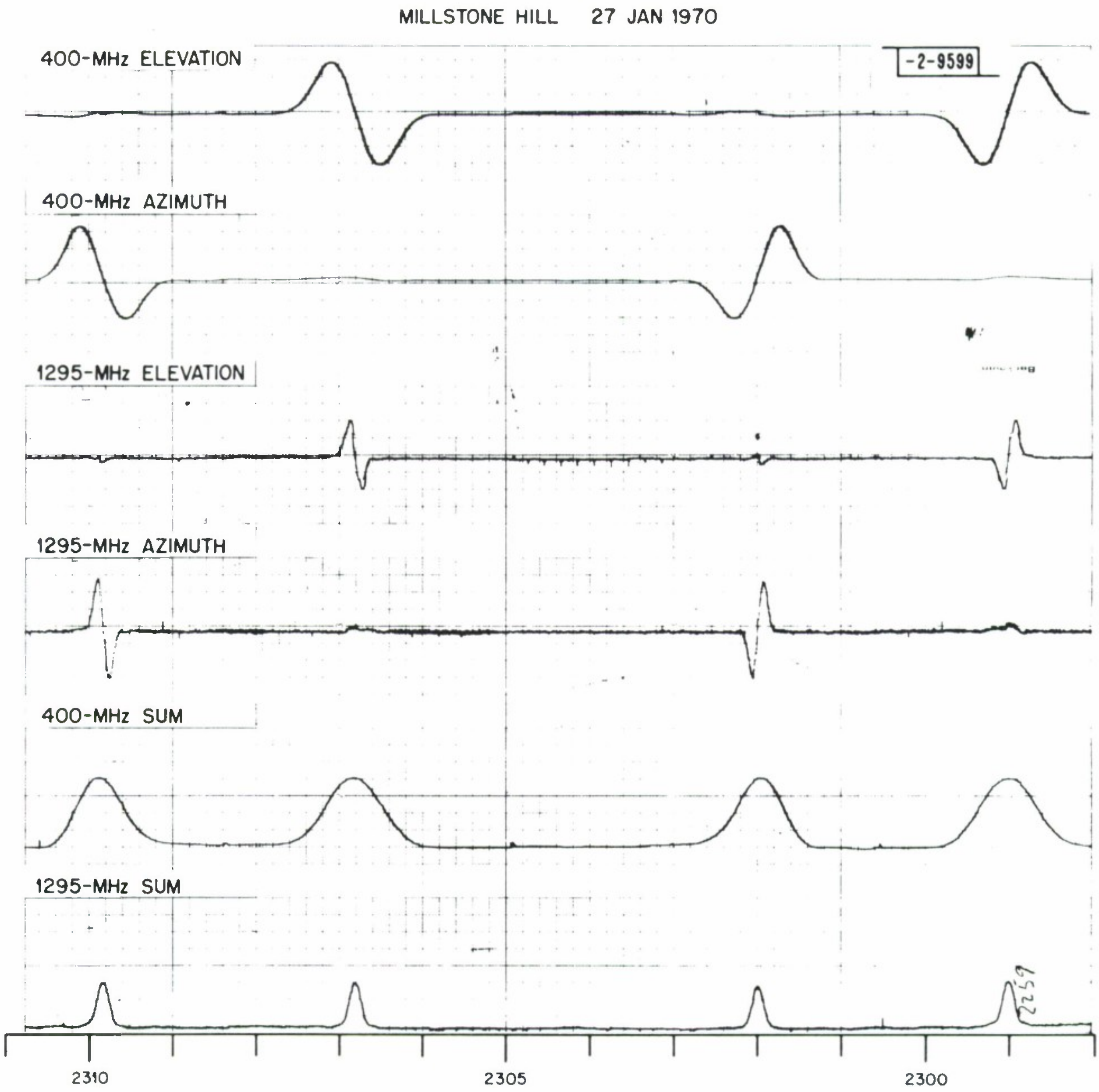

Fig. 15. Analog chart recordings of sum and difference signals observed at L-band and UHF when antenna is scanned through radio star Casseopeia A in azimuth and elevation.

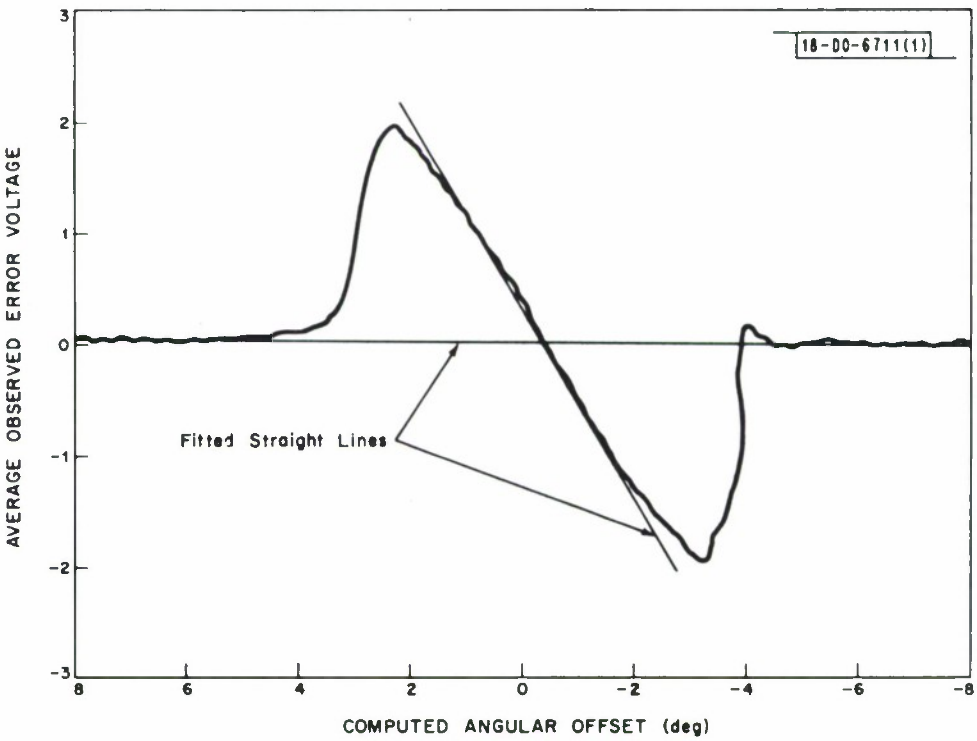

Fig. 16. Diagram indicating manner in which recorded error channel voltages are analyzed to determine exact position at which source lies on axis of beam. Straight lines are fitted to baseline and transition region and their intersection is taken to be exact point of zero offset.

the track and the intersection of these two lines defines the apparent source position.

The accuracy $\Delta\theta$ with which the center position of the beam can be established is determined by (Evans 1969a).

$$\frac{\Delta\theta}{\theta_o} \approx .37 \left[\frac{T_R}{T_A} + \left(\frac{T_R}{T_A}\right)^2 \right]^{\frac{1}{2}} / [BT]^{\frac{1}{2}} \tag{1}$$

where

θ_o = antenna beamwidth

T_R = receiver noise temperature

T_A = antenna temperature of radio source

B = predetection bandwidth

T = integration time

For the observations made on Cassiopeia A the relevant parameters are thosegiven in Table 2.

	400 MHz	1295 MHz
θ_o =	2860 m.deg.	600 m.deg.
T_R =	350^oK	150^oK
T_A =	230^oK	147^oK
B =	10^6 Hz	10^6 Hz
T =	8 seconds*	3 seconds*
$\Delta\theta$ =	2.0 m.deg.	0.3 m.deg.
*	But see text.	

Table 2. Parameters for passive observations of the source Cas A.

The integration times available for establishing the baseline on a standard scan are 24 and 32 seconds at 400 and 1295 MHz respectively and the integration times available for establishing the position of the second straight line (Fig. 16) and 8 and 3 seconds respectively. Hence, under ideal conditions, i.e., when the uncertainty $\Delta\theta$ in the source position is determined only by signal-to-noise ratio considerations (Eq. 1), we would expect

$\Delta\theta \approx 1.0$ and 0.25 m.deg. at 400 and 1295 MHz respectively. In practice this threshold is never reached because of many factors such as the influence of wind on the antenna pointing, receiver gain changes, and various forms of radio interference. On one day, September 3, 1970 for example, when the interference was low, 15 successive scans gave an rms scatter of 6.5 and 3.0 millidegrees at 400 and 1295 MHz respectively.

ii) Sources of Error

The results of antenna pointing measurements, can be biased by several possible sources of error whose effects have been investigated are discussed here.

Squaring at the Phase Detector

If the input signals to the phase detector are v_S and v_D then the output may be written

$$v_o \propto \{v_S\, v_D + \alpha v_S^{\,2} + \beta v_D^{\,2}\} \tag{2}$$

The desired component is $v_S v_D$ and the output is filtered to ensure that the squared terms are small. If, however, α is not identically zero then the baseline will be increased when the antenna is pointed at the source compared to when it is off the source. This has been investigated at 1295 MHz by coupling a noise source to the sum channel. It was found that there was no detectable change in the multiplier output. This implies that biases introduced by this effect are less than 10 millidegrees.

Effects of Receiver Time Constant and Encoder Backlash

The receiver post-detection time constant (0.2 second) must be known and accounted for, since it will cause a linear increase in pointing error with scan velocity. To investigate this effect the pointing errors were measured using scan velocities from 4 to 24°/minute for directions of scan with increasing coordinates and also with decreasing coordinates. From these measurements the effect of the receiver time constants could be determined and removed from data taken at the standard scan speed. These measurements also disclosed that there were no discrepancies attributable to

backlash greater than 10 m.deg.

Improper Phasing of the Feed System

The receivers have phase shifters in the I.F. sections which can be used to balance differences in the phase delays between receivers (Figure 14). These phase shifters are normally adjusted by holding the antenna position slightly off the source and maximizing the power out of the phase detectors. This should not alter the position of the zero crossing unless there is an unwanted phase shift in the RF section before the sum and differencing networks. If indeed there is a phase shift ψ between the two RF signals, then by deliberately introducing a shift ϕ in the phase of one of the I.F. channels, the null in the error beam will be moved by the amount*

$$\Delta\theta = 0.18\, \theta_o \tan \phi \sin \psi \tag{3}$$

Measurements were made to determine the magnitude of any phase unbalance ψ with results that are presented in Table 3. Equivalent lengths of coaxial cable are also given in Table 3 since any phase error in the 400 MHz receiver might be due to cables of unequal length

Channel	ψ	Equivalent Length in Coaxial Cable
400 azimuth	$16^\circ \pm 4$	2 cm
400 elevation	$-2^\circ \pm 4$	-0.2 cm

Table 3. Measured values for the phase unbalance between the signals at the difference element (Fig. 14) of the receivers.

* This expression is derived in Appendix A, together with more general expressions for the case where there are both unequal amplitude and unequal phases for the signals collected by the dipole pairs.

Subsequent examination of all the coaxial cables failed to turn up differences in length as large as 2 cm indicating that amplitude differences may partly be responsible for the effects observed (Appendix A).

Effects of Tropospheric Refraction

An attempt has been made to remove tropospheric refraction using a model that has surface refractivity as a parameter. This model is based on results obtained by R. Crane (Gp. 61) who employed a ray-tracing program together with radiosonde data taken at Albany, New York to explore the refraction as a function of elevation angle and refractivity at the ground. In analyzing the measurements discussed here the ground refractivity was taken to be 313 whereas the actual values ranged from 311 to 378 during the observing period. This corresponds to a spread of 20 m.deg. in the total refraction of the lowest elevation angle (10°) employed.

iii) Results of the Observations

During August and September 1970 about 700 scans of Cassiopeia A and Cygnus A were made. Of these 130 were selected as satisfying the following criteria: a) the scan was on Cas A, b) the receiver baseline noise was less than 5 times expected noise level, c) the scan was taken at 4°/min in a positive direction. The criterion b) was included to remove scans badly corrupted by radio interference.

The pointing errors obtained in these 130 scans are plotted as a function of azimuth and/or elevation in Figure 17ab-19ab. The points have been averaged together to obtain the mean pointing errors and the results are shown in Table 4.

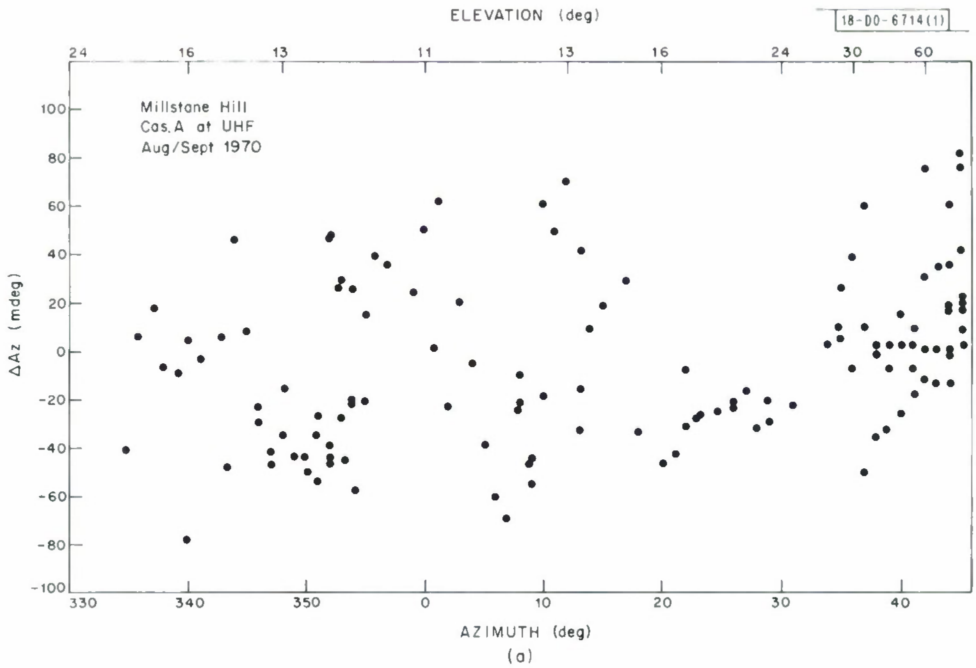

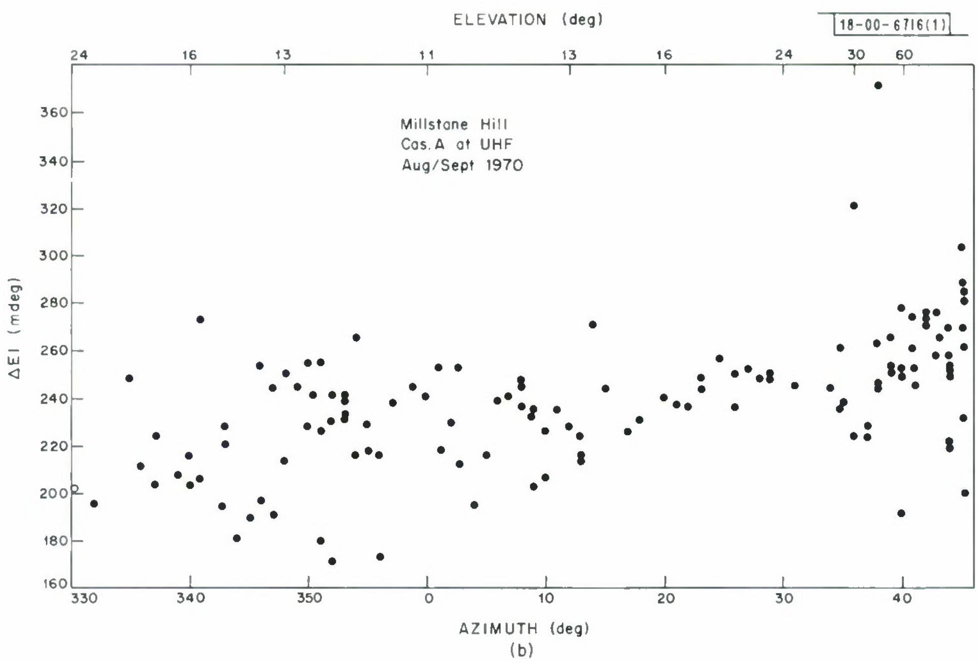

Fig. 17. Deviations (true-observed position) vs azimuth for source Cas A observed at UHF in August and September 1970. Corresponding elevations are shown at top. (a) Azimuth, (b) elevation.

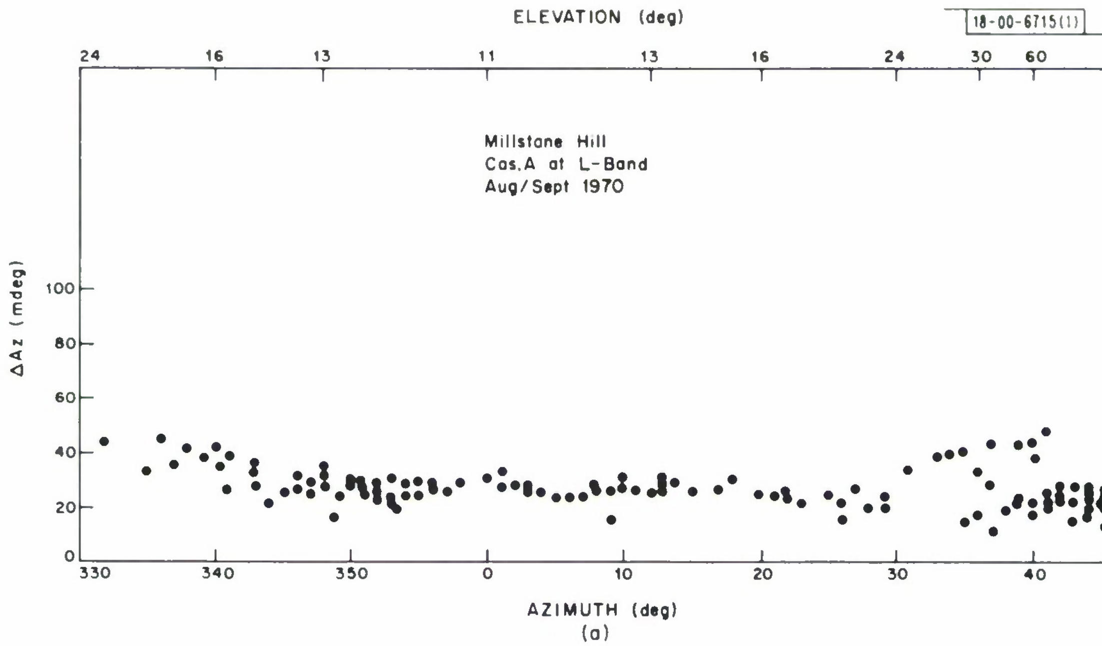

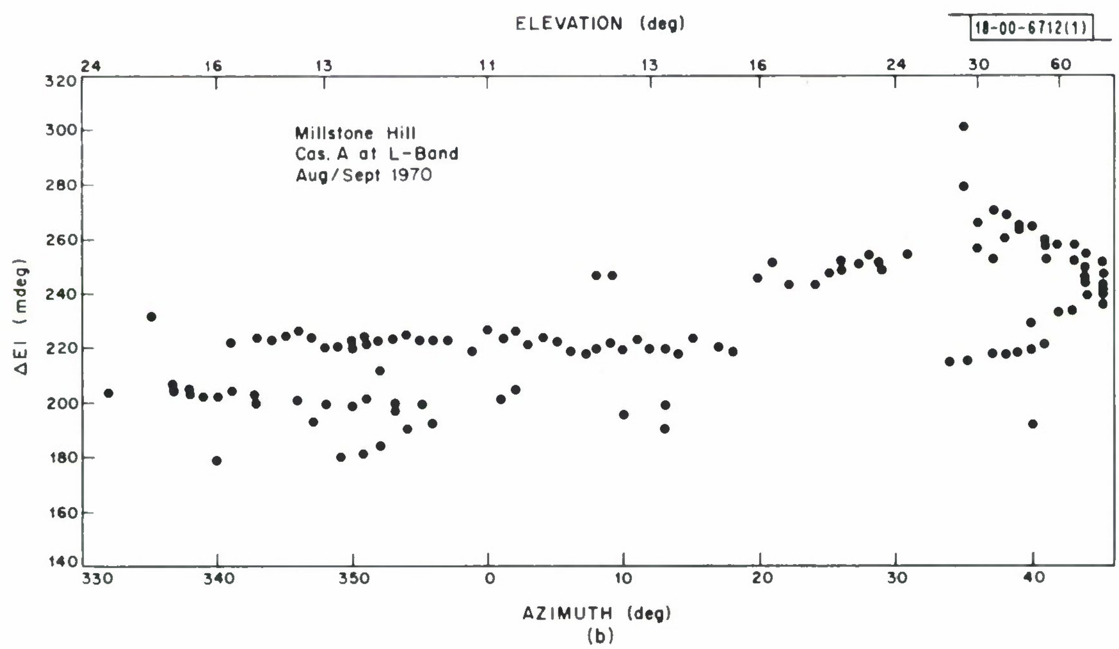

Fig. 18. Deviations (true-observed position) vs azimuth for source Cas A observed at L-band in August and September 1970. Corresponding elevations are shown at top. (a) Azimuth, (b) elevation.

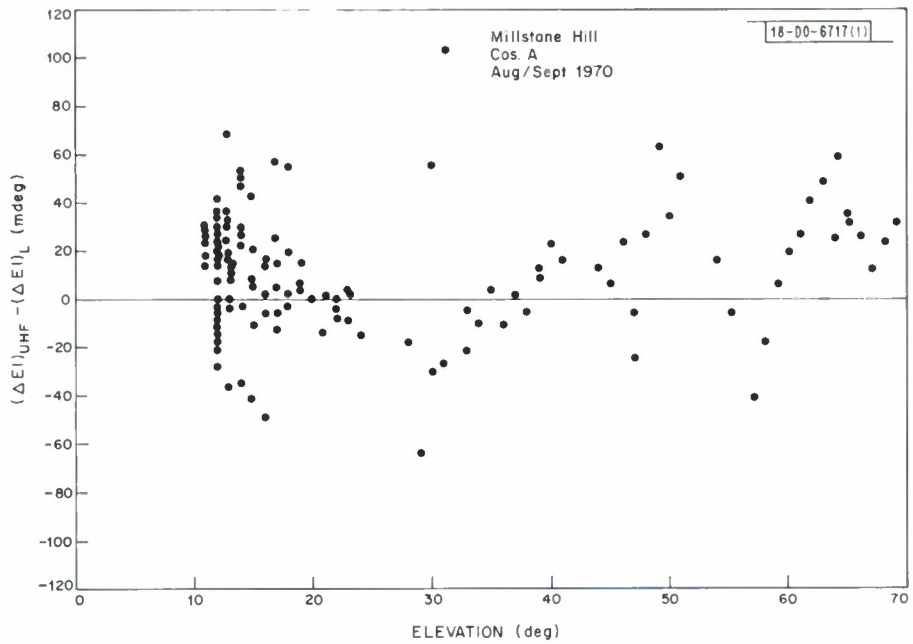

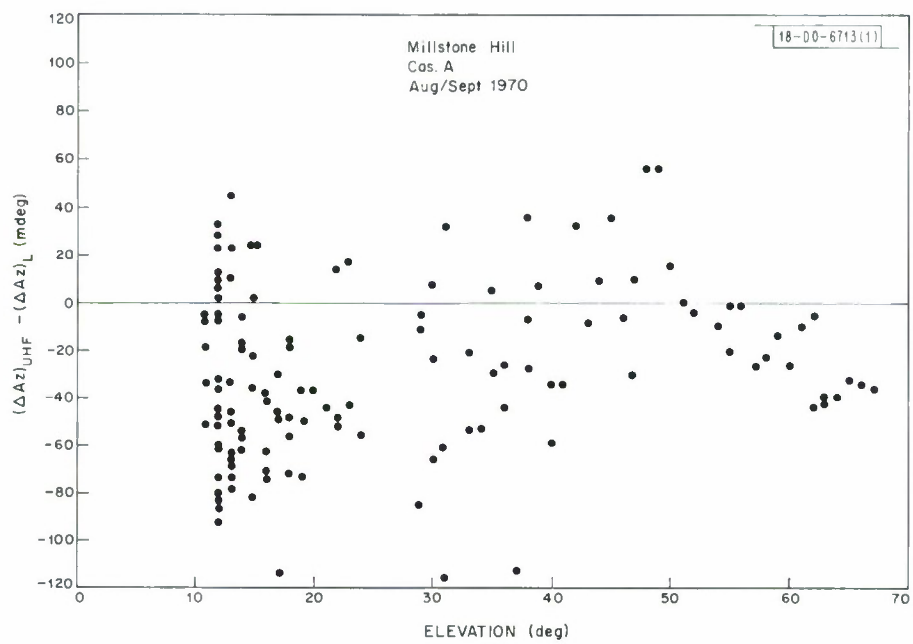

Fig. 19. Differences between UHF and L-band beams observed for source Cas A as a function of elevation in August and September 1970. (a) Elevation, (b) azimuth.

Channel	Pointing Offset (m. deg.)	rms deviation (m. deg.)
400 azimuth	-2 ± 4	37
400 elevation	236 ± 3	31
1295 azimuth	27 ± 1	8
(400-1295) azimuth	-29 ± 4	36
(400-1295) elevation	9 ± 2	23

Table 4. Results of the calibration measurements made in August-September 1970

The uncertainties given in Table 4 for the pointing offset are probable errors computed by dividing the measured standard deviation by $(130)^{\frac{1}{2}}$. It can be seen from Table 4 that the 1295 MHz beam is a better indicator of the true position of the 400 MHz beam than the shaft encoders. That is, the rms uncertainty in the 400 MHz beam with respect to the L-band beam is 36 m.deg. and 23 m.deg. in azimuth and elevation respectively compared with 37 and 31 m.deg. with respect to the encoder readings.

iv) Absolute Gain Measurements

The gain and beamwidth achieved with the new subreflector was determined from measurements on Cas A of the antenna temperature, and beamwidth. The results are summarized in the following table.

Date	Frequency	Subreflector	T_A(Cas A)	η	G	Beamwidth (Elevation)	Beamwidth (Azimuth)
			°K	%		Deg.	Deg.
7/31/69	1295	Solid	165 ± 3	44	47.2	0.596±.003	0.606±.003
2/12/70	1295	FSS I	75 ± 3	22	43.8	0.649±.003	0.685±.003
5/29/70	1295	FSS II	147 ± 10	40	46.7	0.610±.006	0.602±.006
2/12/70	400	FSS I	230 ± 15	20	33.6	2.91±.02	2.68±.02
5/29/70	400	FSS II	220 ± 20	19	33.4	2.86±.05	2.64±.04

Table 5. Comparison of the gain and beamwidth obtained with various subreflectors. FSS II is the frequency selective subreflector now in use.

b) Observations of Radio Star Scintillations

The radio star Cygnus A was tracked at low elevation angles with the Millstone antenna at 400 MHz to measure the fluctuation in signal level and apparent angle-of-arrival. This source rises and sets near 30° and 330° azimuth respectively. During each observation the antenna continually followed the predicted source position under computer control. The receiver sum and error voltages were sampled every 0.1 second and via the computer were recorded on magnetic tape for later analysis. Subsequently, these data were averaged over intervals of 10 seconds (100 samples) and the rms deviation of the samples in each 10 second interval was calculated. Figure 20 shows the mean signal amplitude and mean elevation offset measured on one such observation along with rms deviation. The expected rms amplitude fluctuation due to receiver noise is given by

$$\sigma_A = \frac{T_A + T_R}{\sqrt{BT}} \tag{4}$$

where

T_R = system temperature ≈ 350°K

T_A = antenna temperature ≈ 180°K

B = predetection bandwidth ≈ 1MHz

T = sample period = 0.1 second

which yields an rms deviation of about 2°K or 1% of the signal amplitude. Above 7° elevation this is the fluctuation level observed in Figure 20. At elevation angles below 7° the fluctuation level steadily increases. The contribution of the receiver noise and encoder granularity to the rms deviation in angle offset is about 8 mdeg. and this is the level observed in Fig. 20 at elevation angles above about 3°, but below 3° the angular fluctuations are larger.

There are two causes for the variations observed: ionospheric irregularities and ground reflections. A signal entering the antenna which has been reflected off the ground interferes with the direct signal to

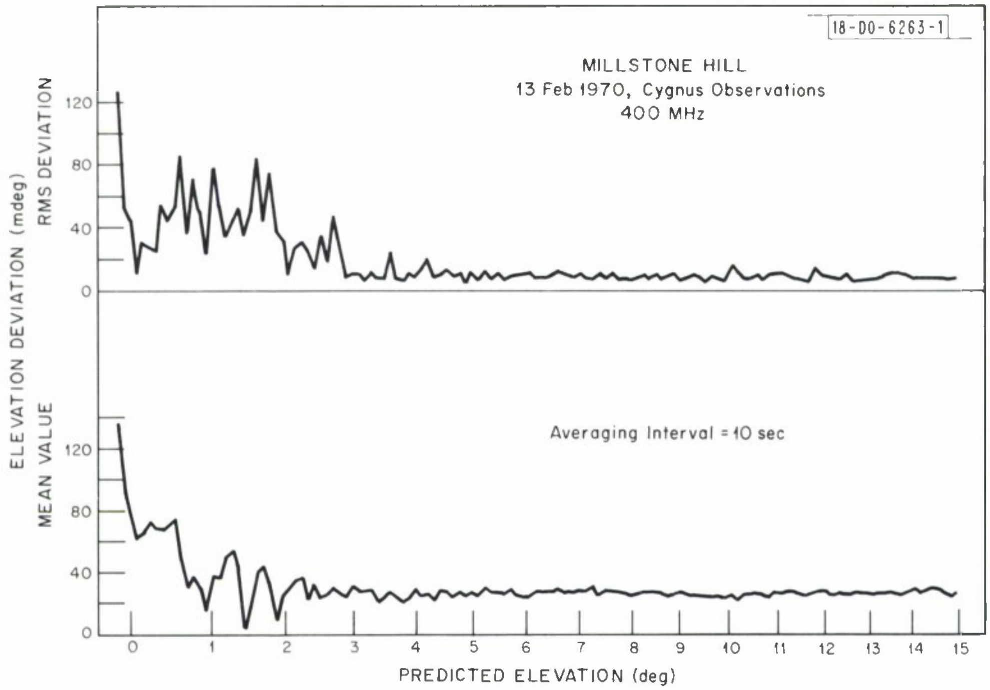

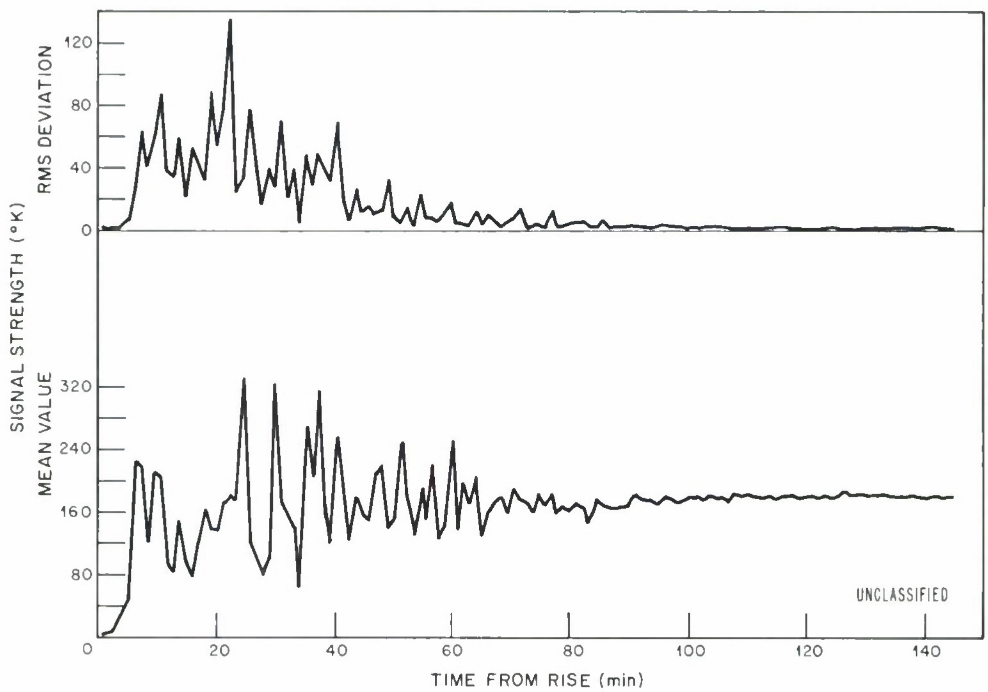

Fig. 20. Elevation fluctuations observed at 400 MHz for source Cygnus A when rising on 13 February 1970. Lower curve in each block is average for 10-second intervals; upper curve is rms deviation about this average.

produce variations in the apparent angle-of-arrival and signal intensity. If the ground in front of the antenna were a smooth plane, then maxima and minima would appear in the signal intensity with a frequency

$$f = \frac{2 \cdot h}{\lambda} \cdot \cos E \frac{dE}{dt} \tag{5}$$

where h = height of antenna above reflecting surface

E = elevation of source

λ = wavelength

The height h of the Millstone Hill antenna above the surrounding terrain is about 80 meters. Applying Eq.(5) to the case of Cygnus A observed near the horizon at 400 MHz one finds a frequency f of about 1 cycle per 180 seconds. Although the actual terrain is not perfectly smooth, this frequency should still be the principal periodicity. Therefore, the variations visible in Fig. 20 of the signal amplitude and angle-of-arrival with a period of several minutes time are attributable to ground reflections. However, the rms variation with respect to the 10 second average should be due almost exclusively to the irregular structure in the ionosphere. That is the short period fluctuations are thought to be caused by irregularities in the F region having a scale size of the order of a Fresnel zone (600 meters).

Observations of Cygnus A were made on four days in early 1970. The results of these are summarized in Table 6 and Figure 21. As expected, the occurrence of amplitude and angle scintillation is well correlated, and there is also some suggestion that the scintillation is correlated with the planetary magnetic index K_p.

c) Satellite Tracking Experiments

i) Computer-Aided Satellite Tracking (CAST)

The current period has been one of extensive hardware upgrading aimed at developing a dual-frequency precision tracking capability. Considerable progress has also been made with respect to computer software. In particular, Millstone's unique real-time program for providing Computer-Aided Satellite

DAY (1970)	RISE/ SET	ELEVATION (DEG)	% AMPLITUDE FLUCTUATIONS	ELEV BIAS mdeg	ELEV FLUCT mdeg 10 sec average	K_p
24	S	7	4	0	7	2-
		5	10	0	7	
		3	10	40	15	
		2	10	120	20	
		1	20	280	25	
43	S	7	1	0	7	1-
		5	2	0	7	
		3	2	0	7	
		2	2	40	15	
		1	4	300	20	
44	R	7	1	0	7	2
		5	5	0	7	
		3	10	20	10	
		2	20	30	25	
		1	40	140	55	
72	R	7	1	0	8	1+
		5	1	0	8	
		3	3	0	8	
		2	4	40	8	
		1	4	120	8	

Table 6 Results of Observations of Scintillation of the Intensity and Position of the Radio Source Cygnus A in Spring 1970

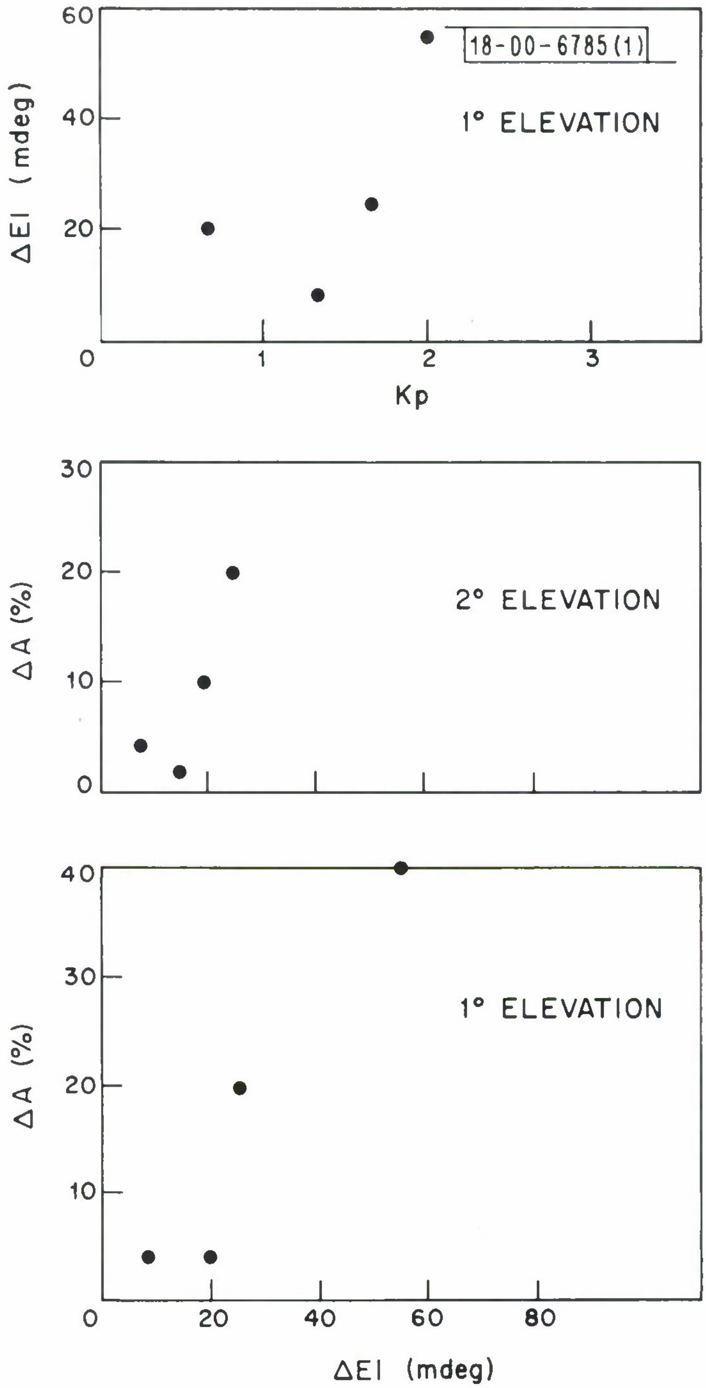

Fig. 21. Top: Variation of rms angular scintillation with magnetic K_p index at 1° elevation. Center and bottom: Variation of amplitude scintillation with angular scintillation or 2° and 1° elevation.

Tracking (CAST) has been successfully modified to operate on angle and Doppler data alone, permitting its use with UHF signals received from satellite-borne beacons. The program was previously operable only at L-band, where active operation of the radar provides a direct measurement of range as well.

Major functions of the CAST software are indicated in Fig. 22. All raw tracking data and computer steering commands are recorded on magnetic tape for later playback and analysis. Meanwhile, raw observations are edited, corrected for known biases, and smoothed using a least-squares fitted polynomial over consecutive ten-second smoothing intervals. Only the smoothed mid-point values are retained (to reduce storage requirements), and an iterated differential correction procedure is employed to best fit an orbit to these smoothed observations. A weighted least-squares criterion is used for this purpose, with weights being derived from the computed standard deviations over the respective smoothing intervals. Steering signals from the computed ephemeris are then available in angle, range, and Doppler. These commands permit a satellite to be smoothly tracked through the elevation range ($\leq 10^{\circ}$) where refraction effects are expected to be largest, and the echo intensity weakest (owing to the increased radar range).

ii) Satellite Tracking Exercises

Earlier in the year a number of potentially interesting satellite tracks were recorded using only the new UHF-beacon tracking capability with polar-orbiting Navy navigation satellites. However, it did not prove possible to obtain repeatable antenna calibrations with the original shaft encoders, so that specifications of models for angle-bias and refraction corrections have had to wait for the completion of the new optical encoder system that has just been installed.

Qualitatively, the evidence at hand shows that amplitude scintillations can be observed with regularity to the North but are rarely present at all to the South. Fig. 23 shows an interesting example of this phenomenon taken from a chart recording of raw servo errors and signal amplitude during UHF autotrack. The pass was observed approximately 20 hours after a severe

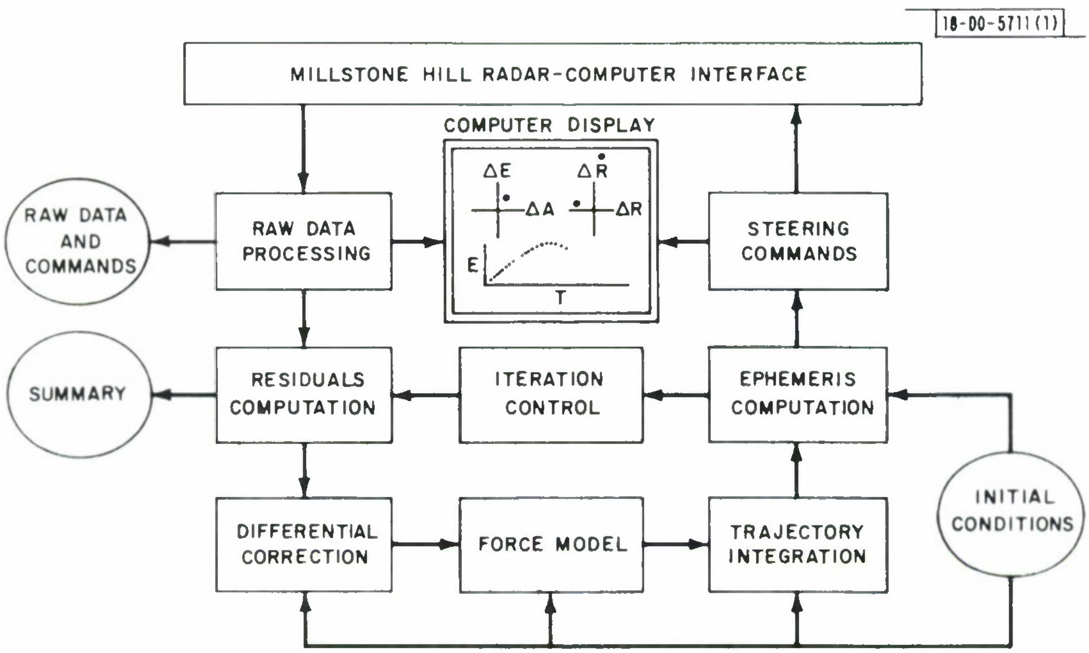

Fig. 22. Diagram showing computation and display functions of Computed Aided Satellite Tracking program (CAST).

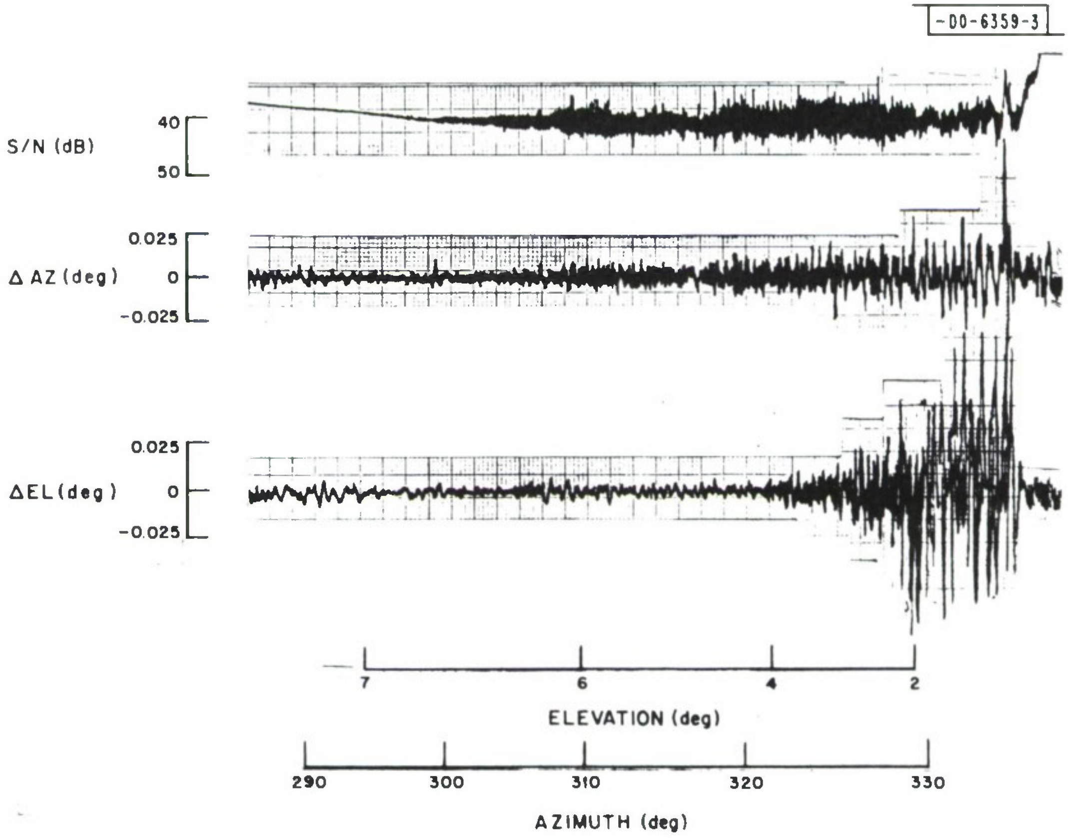

Fig. 23. Analog records of signal intensity (actually AGC voltage) and raw servo-error-voltages while tracking Navy navigational satellite at 1712 EST on 9 March 1970. Note start of scintillation at about 6.5° elevation and corresponding growth in azimuth-error-voltage fluctuations.

magnetic disturbance when visible aurora was seen locally. Incoherent scatter data were recorded earlier during this event (see Section Vc). Quantitative estimates of the tracking perturbations which accompany such disturbances cannot yet be made with confidence. An examination of some of the tracking residuals suggests that gross refraction effects are also occurring at low elevations. To illustrate this, we show in Fig. 24 the elevation residuals remaining after an orbit has been fitted to the pass in the manner outlined above. The tight grouping of the plotted raw data deviations shows that good tracking was present, but the wavy trend resulting from the comparison with a theoretical orbit smoothly fitted to the data discloses deviations in the apparent angle-of-arrival. These are not evident, of course, in a simple record of raw servo error voltage (e.g.Fig. 23).

In April 1970 a test run of a dispersion experiment proposed by G. H. Millman of the General Electric Company was successfully conducted. The purpose of the test was to measure the correlation in integrated electron content between a satellite and two widely separated ground stations, in order to deduce the spatial extent of ionospheric irregularities.

The satellites involved were spacetrack catalog #2754, 2965, 3807 and 3133, of the Navy Navigation series. These satellites transmit coherently at 400 and 150 MHz. The signals are phase modulated, but this is done in a way that does not interfere with experiments of this type. Hence, the signals can be considered to be sine waves. If the transmitted phases are $\phi_1^t = \omega_1 t$ $\phi_2^t = \omega_2 t$, then the phases at the receiving station on the ground will be

$$\phi^r_1 = \omega_1 \left(t - \frac{\Lambda_1}{c}\right) \tag{6}$$

$$\phi^r_2 = \omega_2 \left(t - \frac{\Lambda_2}{c}\right) \tag{7}$$

where Λ_1 and Λ_2 are the path lengths given by

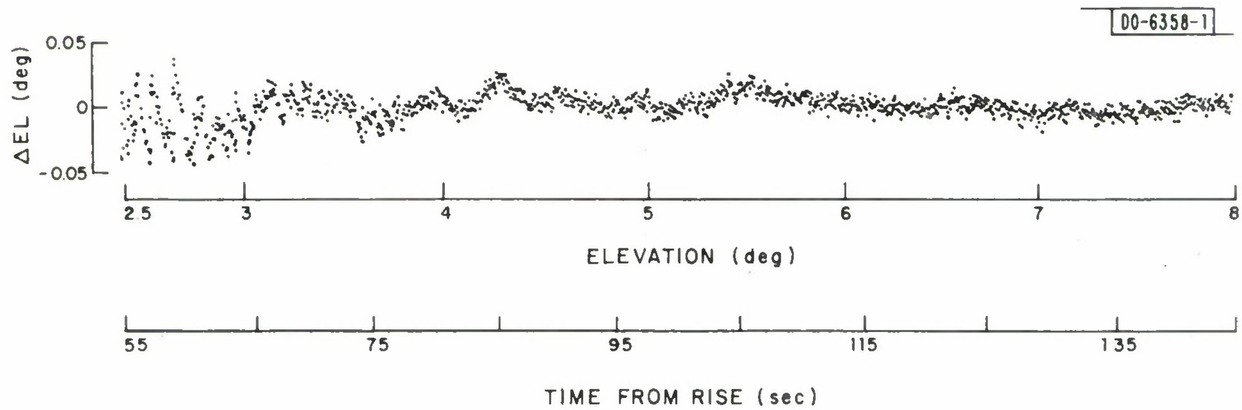

Fig. 24. Elevation residuals after an orbit has been fitted to observations of UHF satellite beacon at 2338 EST on 19 March 1970. Cluster of points suggests that tracking was good and has a noisiness of $\sim 0.01^{\circ}$ rms. Deviations at 5.5°, 4.3°, and 3.7° are thought to be examples of ionospheric refraction. Below 3° there is interference between direct and ground reflected rays.

$$\Lambda = \int (n_i + n_T)\, d\vec{r} \tag{8}$$

in which n_i and n_T are the ionospheric and tropospheric indices of refraction and the integration is over the propagation path $\vec{r}$. Since

$$n_i \approx 1 - \frac{2\pi\, Ne^2}{m\omega^2} \tag{9}$$

where N is the electron density, e the charge and m the mass of an electron, it follows that

$$\phi^r{}_1 \cong \omega_1 t - \frac{\omega_1 R}{c} + \frac{2\pi N_T e^2}{m\omega_1 c} + \frac{\omega_1}{c} \int n_T dr \tag{10}$$

$$\phi^r{}_2 = \omega_2 t - \frac{\omega_2 R}{c} + \frac{2\pi N_T e^2}{m\omega_2 c} + \frac{\omega_2}{c} \int n_T dr \tag{11}$$

where N_T = total electron content along the path (cm^{-2}), and c = velocity of light, R = range.

Hence the terms involving range can be eliminated by computing the phase difference α where

$$\alpha = \phi^r{}_1 - \frac{3}{8} \cdot \phi^r{}_2 = \frac{2\pi N_T e^2}{mc} \cdot \frac{55}{24} \cdot \frac{1}{\omega_2} \tag{12}$$

This yields

$$\alpha = 4.8 \times 10^{-11}\, N_T \text{ radians} \tag{13}$$

The two receiving terminals in the experiment were the 84' antenna at Millstone (Sec. 2) and a 30' antenna operated by the General Electric Company in Schenectady, New York. These stations were each able to measure

directly the phase difference α along with other information; their separation is approximately 200 km east-west.

In the GE system both the 400 and 150 MHz receivers contained phase-locked loops in which oscillators were locked to the incoming signals. The phases of these oscillators were compared to obtain α which was recorded on magnetic tape in analog form and also punched on paper tape at a rate of one sample per second. Signal amplitude data was not considered useful because the satellite tracking was done manually.

At the Millstone site the 400 MHz and 150 MHz signals were successively heterodyned down to their frequency offsets from nominal (32 and 12 KHz respectively) as described in Sec. 2d). The 400-MHz signal (at 32 KHz) was then applied to a phase-lock loop-tracking filter which produced two constant amplitude squarewave signals in phase quadrature whose frequency was equal to 3/8ths of the frequency of the input signal. These signals were then employed as the reference signals to phase detectors driven by the 150 MHz signal (at 12 KHz). The outputs are two voltages, $A \cos \alpha$, and $A \sin \alpha$ where A is the amplitude of the 150 MHz signal. Complete phase coherence in the system is insured by deriving all of the local oscillator signals from the same reference oscillator. The quantities $A \cos \alpha$ $A \sin \alpha$, the 400-MHz signal amplitude, the antenna azimuth and elevation and the monopulse error voltages were sampled, converted to digital form and recorded on magnetic tape at a rate of 15 samples per second.

Data from 18 satellite passes were recorded simultaneously at the two sites. The geometry of one typical pass is shown in Figure 25. The track of the geographic latitude and longitude where the line joining the satellite to the receiving station passes through 350 km altitude is shown along with the time, elevation angles, and aspect angles (at 350 km) for this pass. The data recorded at Millstone were processed on the XDS 9300 computer which calculated the 400 MHz signal amplitude, the 150 MHz signal amplitude, α and $d\alpha/dt$ every 1/15th of a second. These quantities were averaged over 150 samples (10 seconds) and the mean and rms deviation plotted. Figure 26a-c

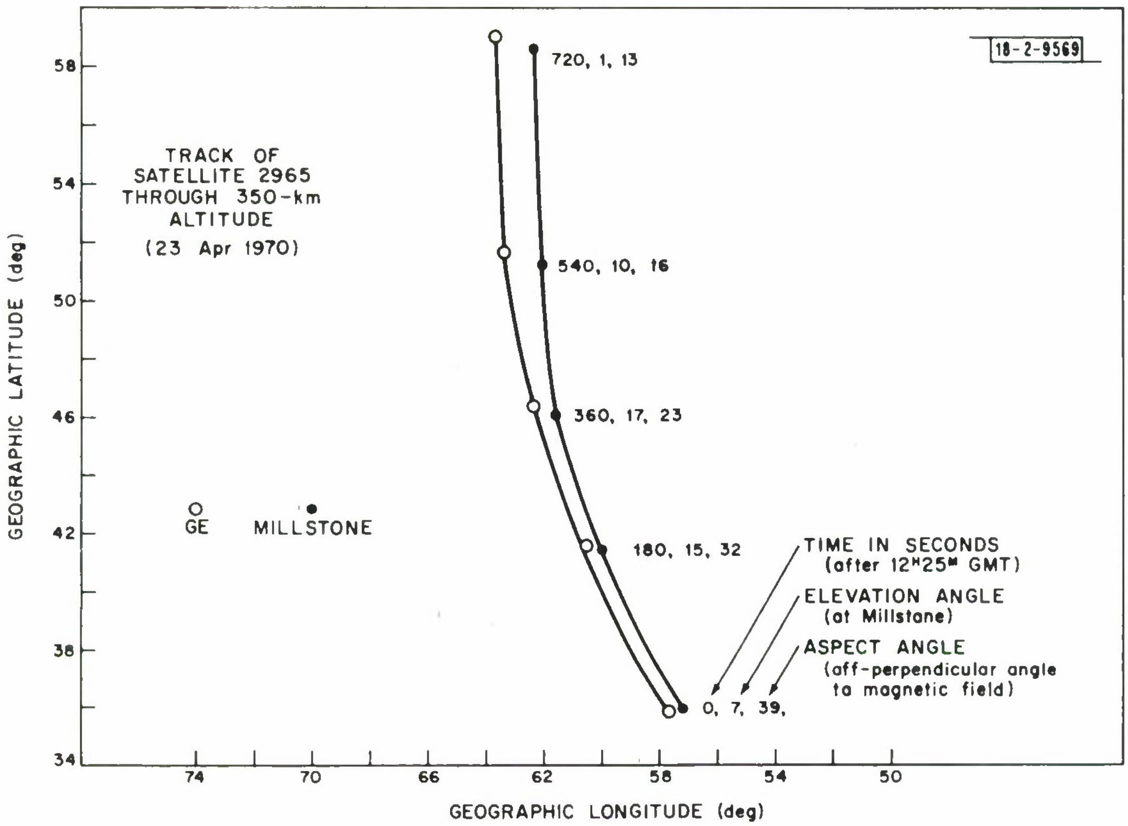

Fig. 25. Locus of intersection of line-of-sight from Millstone Hill and GE, Schenectady tracking stations to satellite with altitude of 350 km for pass on 23 April 1970.

shows some of the results obtained. In Figure 26a, the 150 MHz signal amplitude and rms deviation are plotted as a function of time through the pass. The smooth cyclical fluctuations with period of about 60 seconds are due to Faraday rotation of the plane of polarization which is present because the transmitted polarization is elliptical and the receiving antenna is linear. The rms deviation is expressed as a fraction of the mean signal strength. When the scintillation is strong, the direct ray disappears and the amplitude probability distribution of the received signal becomes a Rayleigh distribution with an rms deviation of 110 percent of the mean. Note that this occurs for the period of the pass beyond 360 seconds. Figure 26b shows the 400 MHz signal amplitude and rms deviation. As expected, the deviations are much smaller than at 150 MHz. At both frequencies the disturbances occurred mainly as the satellite set in the North. Figure 26c shows the phase difference α as a function of time. The general increase of the phase as the satellite proceeds North is attributable simply to the increase in the path length through the ionosphere. The dip near 400 seconds is attributed to the presence of a region of low F-region density known as the Ottawa trough (Muldrew 1965, Andrews and Thomas 1969). The absolute electron content is not directly measurable with this technique because of the unknown constant phase difference. The peak phase fluctuation level during the disturbed portion of the track reaches 10^{-11} electrons/cm^2 which is a fractional deviation of somewhat less than 1 percent. Figure 27 shows α measured both at Millstone and Schenectady with a 10-second smoothing time. The values of α at each site have been set equal at the beginning of the track. Figure 27 shows (at bottom) the phase difference α observed at the two sites as well as the fluctuation remaining when the 10-second running mean is removed to emphasize the fluctuating component. The similarity in the measured values of α and the fluctuating component is very great.

During the period of these tests, disturbances were noted on almost every pass when the satellite's geomagnetic latitude was greater than 50°. These disturbances were characterized by large signal amplitude and phase

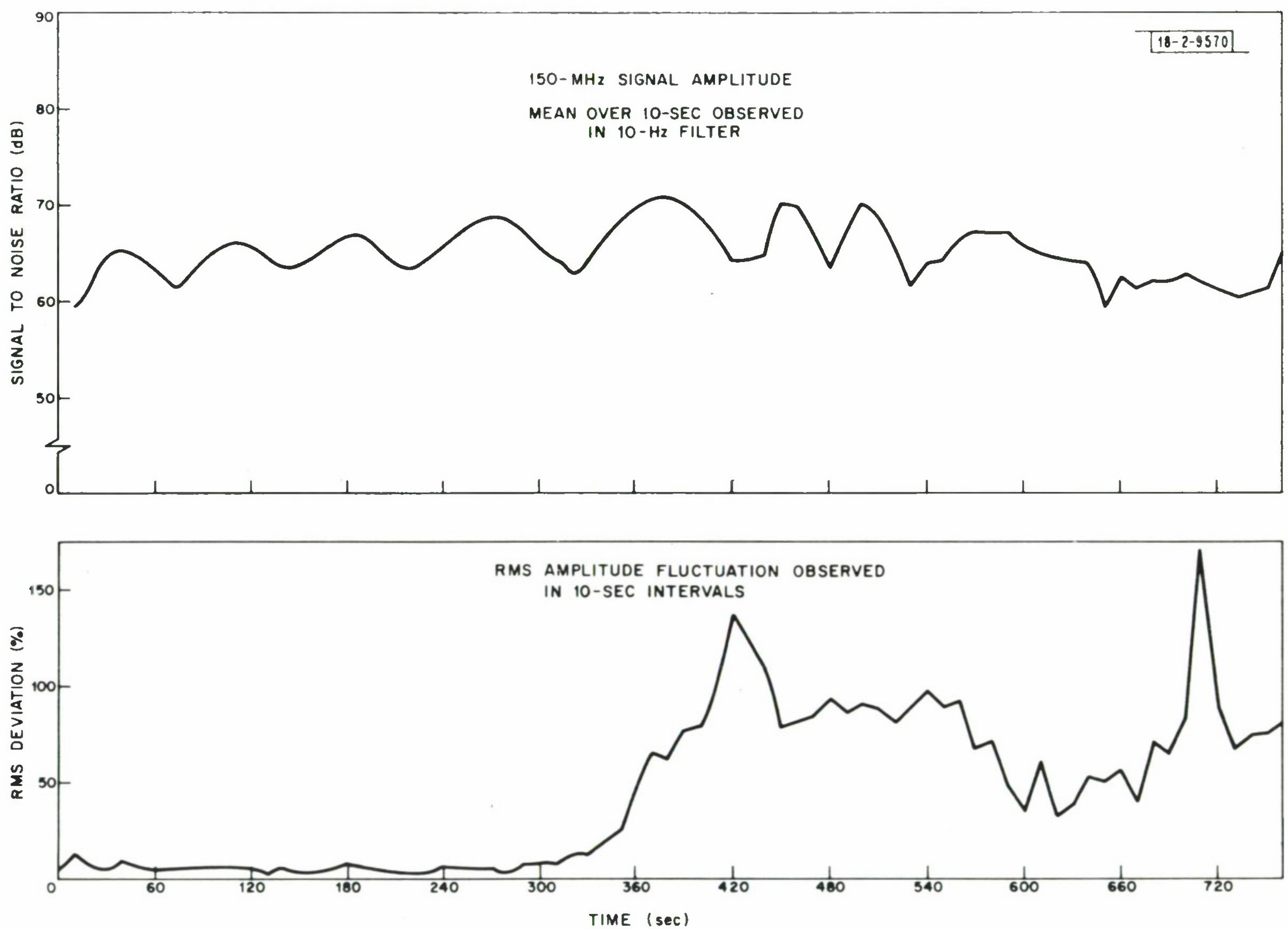

Fig. 26(a). Mean amplitude and standard deviation of 150-MHz signal received at Millstone for 10-second averages.

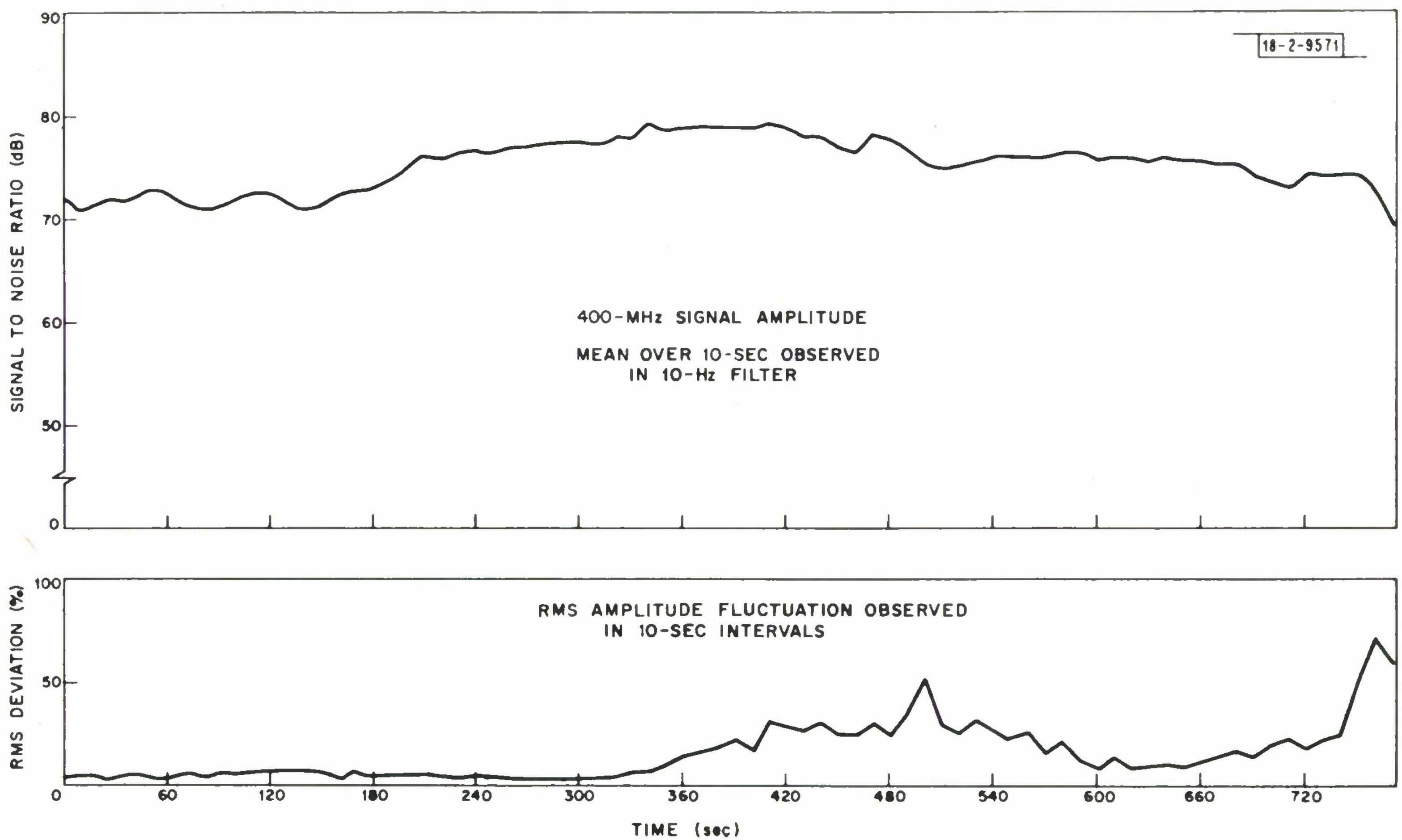

Fig. 26(b). Mean amplitude and standard deviation of 400-MHz signal received at Millstone for 10-second averages.

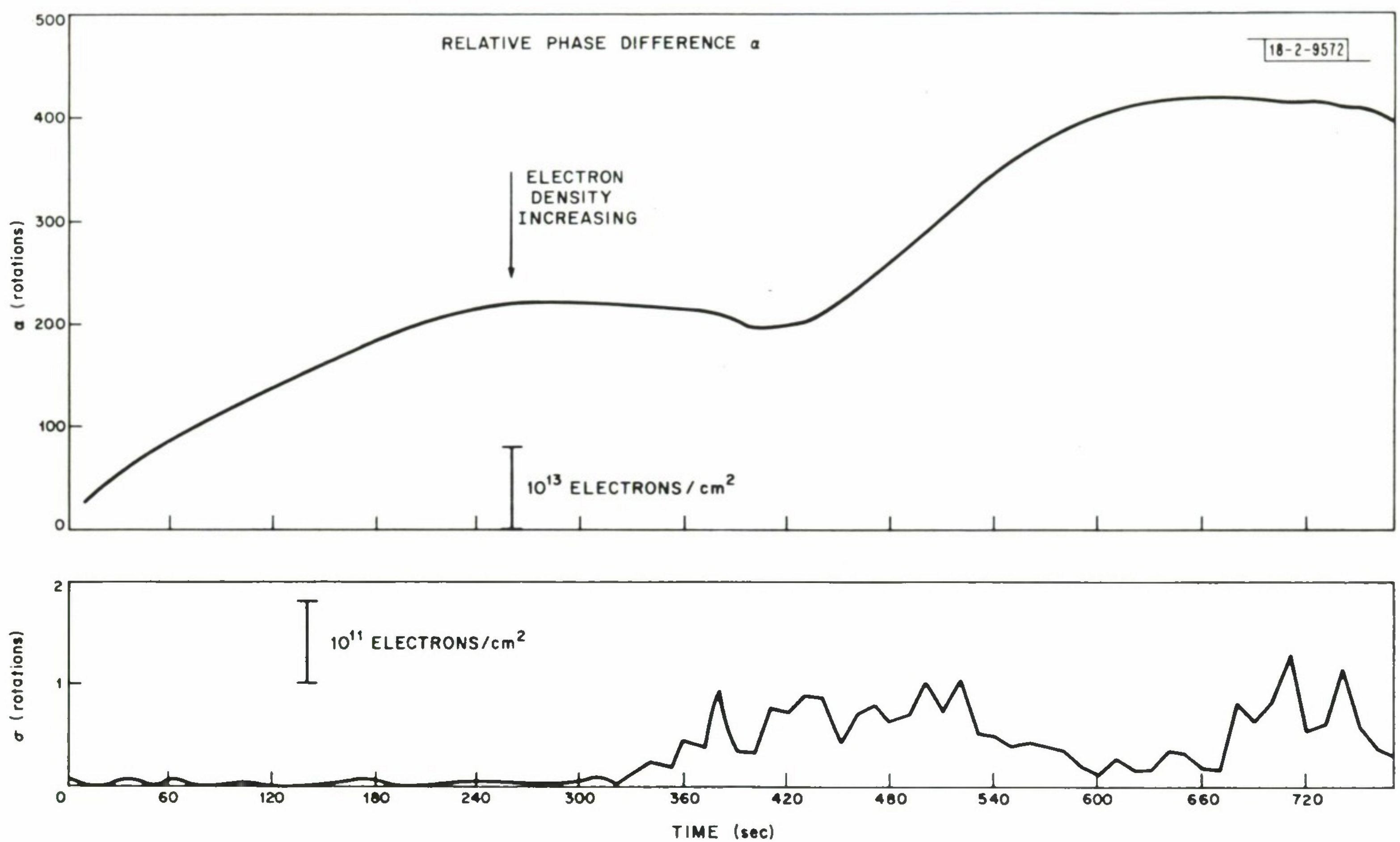

Fig. 26(c). Mean relative phase difference α and standard deviation measured at Millstone for 10-second averaging periods; α is proportional to integrated electron content. Decrease in electron content after near 400 seconds following closest approach is attributed to Ottawa trough.

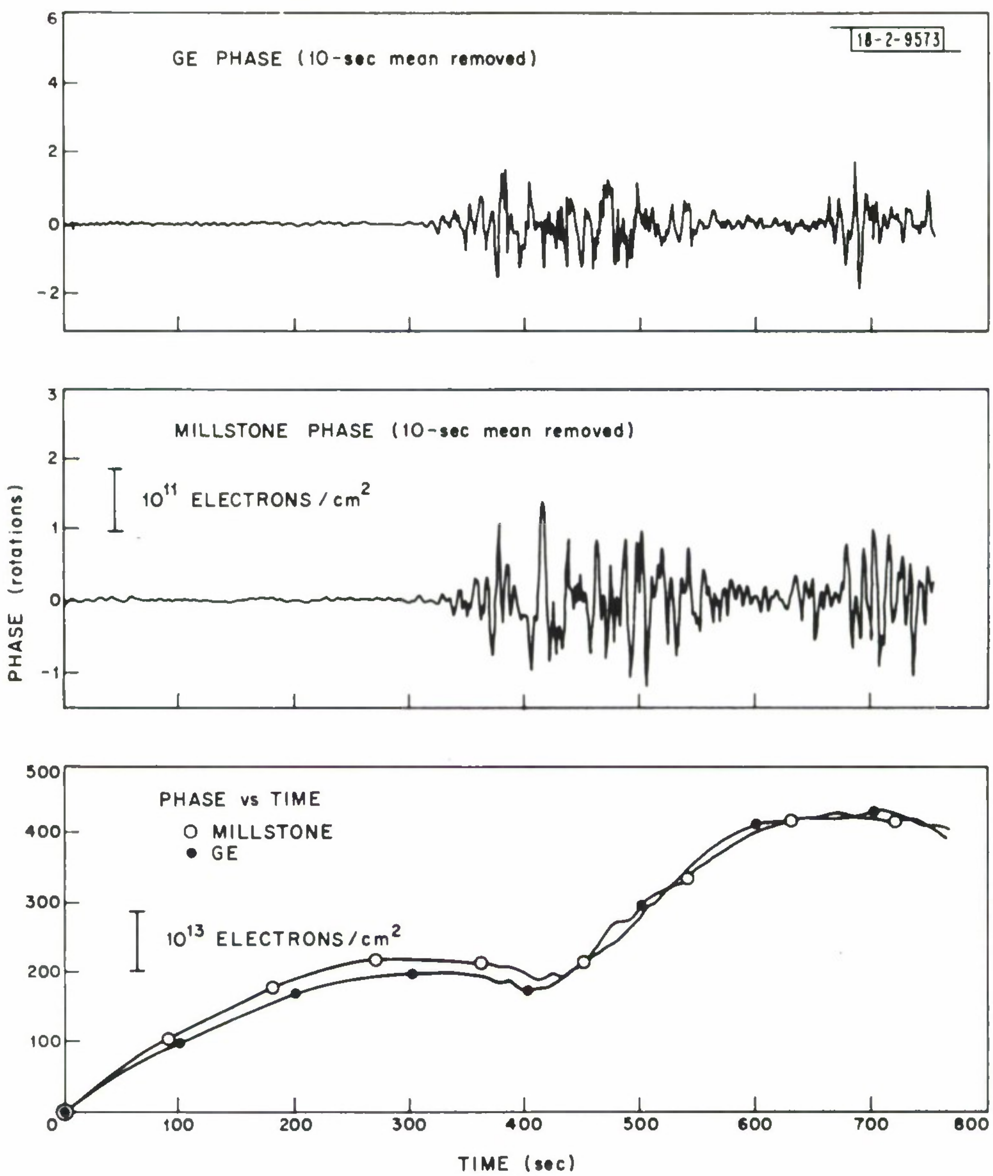

Fig. 27. Top: Relative phase, α, at GE site with 10-second running mean removed. Center: Relative phase, α, at Millstone with 10-second running mean removed. Bottom: Relative phase, α, at GE and Millstone; 10-second smoothing period.

fluctuations. The disturbances were seen at both sites at the same time in almost all cases. This indicates that the irregularities causing these disturbances are at least 200 kilometers in extent. This is not surprising in view of earlier results obtained by other workers that show that the scintillation region occupies an oval about the magnetic pole which is similar to, though somewhat different from, the auroral oval.

In Figure 28 we show a representation of the polar ionosphere taken from the paper by Andrews and Thomas (1969). The oval shaded region represents the region of greatest occurrence of visual aurora. This is also the region of greatest particle precipitation (mostly electrons). Associated F-region effects seem to be large irregular increases of electron density which are found (by the topside sounder satellites) to lie between the solid lines shown in the figure. The midlatitude ionosphere appears to terminate near 55° geomagnetic latitude and between this termination and the auroral oval is a region of low electron density often called the "trough" region. From the measurements presented here it appears that the scintillation we observe is caused by irregularities that lie near the poleward edge of the trough. To show this, we have plotted in Figure 28 several satellite tracks. The boxes represent the parts of the track when scintillations were encountered. Those shown shaded were on 24 April 1970 when the K_p index was around 2, i.e., close to the value for which Figure 28 was drawn. The tracks on 23 April were taken during a more disturbed period ($K_p = 6$) when the auroral oval and trough region would be expected to be more expanded. As can be seen, the scintillations in most cases extend to lower latitudes on this day.

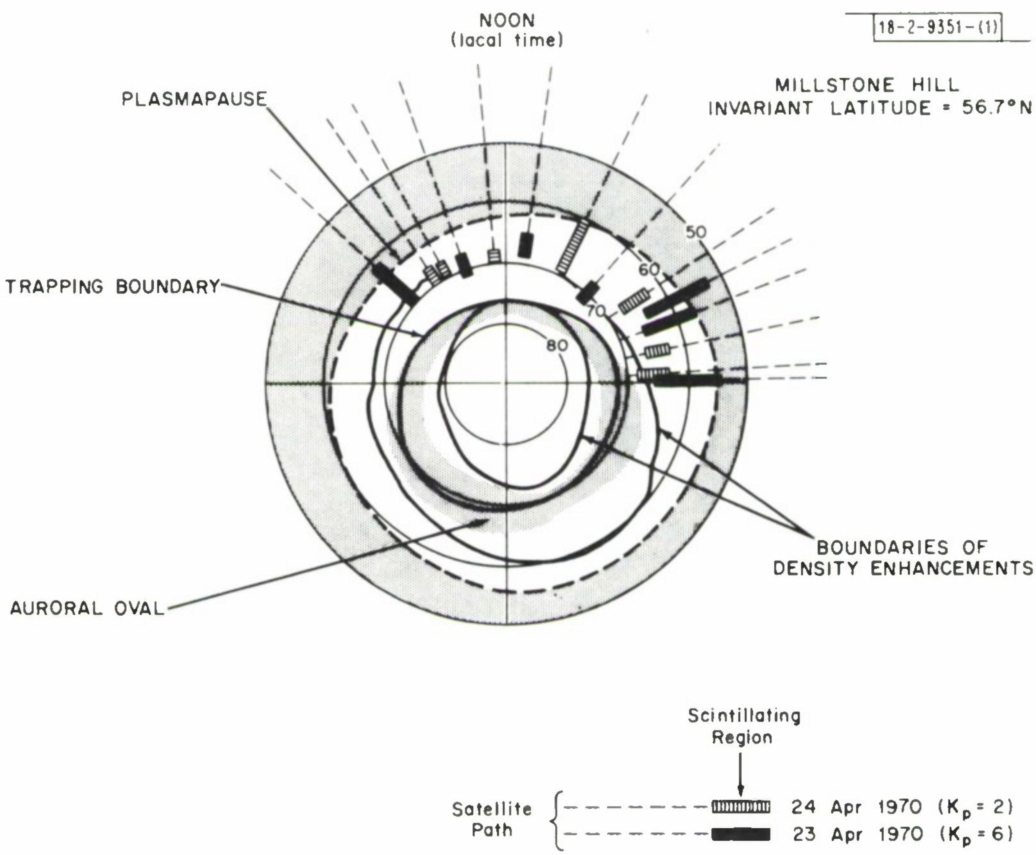

Fig. 28. View of north polar region in an invariant latitude coordinate system. Outer shaded region represents midlatitude ionosphere (corotating with the earth). Inner shaded ring is auroral oval where visual aurora are seen most often. Solid lines represent boundaries between which large irregular increases in F-region electron density are seen by topside sounder satellites. Figure was taken from paper by Andrews and Thomas (1969) and boundaries are drawn for their positions when the K_p index is 3. Superimposed on this figure are tracks of satellites observed using VHF/UHF phase-difference method. Shaded regions indicate portions of track where pronounced phase (and amplitude) fluctuations were encountered on two days in April 1970. As can be seen, irregularities seem to lie close to northern edge of trough of low density between midlatitude and auroral regions.

iii) Relationship between Scintillation and Auroral Clutter

It is of considerable interest to know if there is any relationship between the occurrence of auroral clutter echoes and scintillation. The latter is thought to be caused principally by irregularities in the F region and only under extremely disturbed conditions would it be expected that the E region would give rise to scintillation effects. Thus correlation between the occurrence of scintillation and auroral echoes would exist only if the causal mechanisms act at the same time and are therefore in some way related. One way that this could come about would be if both are produced by particle precipitation (albeit by particles of different energy). Another possible coupling mechanism might be that random variations in the strength of the horizontal electric field responsible for driving the auroral electrojet could be communicated into the F region along magnetic field lines to produce corresponding fluctuations of electron density.

In order to test the possibility that the two effects always occur together, we made a series of measurements in which satellite tracks were interspersed with searches for auroral echoes. In order to maximize our ability to detect the presence of F region irregularities that are responsible for scintillation the intensity of the VHF beacon on the satellite was monitored with analog recordings. These measurements were carried out in the evening hours in August and September and Table 7 summarizes the results obtained. Scintillation of the VHF beacon was almost always present toward the north below a certain elevation angle. By contrast the auroral returns occurred less often and in an erratic fashion. On some nights there were no auroral returns at all; on others when echoes were obtained they persisted only for very short periods. We conclude that there is no relationship between scintillation at VHF and auroral clutter detected at L-band. This may, however, merely be a manifestation of our very different sensitivity to the two effects. Possibly if both types of measurements were made at UHF some correlation would be found.

Date	VHF Scintillation Results	L-Band Aurora Results
August 5	Scintillation at VHF on three passes	No clutter echoes
August 6	Scintillation on 4 VHF passes	Trace of auroral echoes after one pass of 3133 at 0239 GMT Az 358°-too weak to record.
August 7	Scintillation on 3 passes	No recordable aurora
August 11	Scintillation observed	No recordable aurora
August 12		Failure: program not working
August 26	5 passes observed and recorded. Strongest scintillation seen so far	No trace of aurora
August 27	Weak to normal scintillation on two passes	Weak aurora seen - no direct association with scintillation
August 28	Recorded one intensely disturbed and three moderately disturbed passes	Weak auroral echoes seen and recorded - no direct association with disturbed passes
September 1	Moderately scintillating passes. No obvious detailed correlation	Weak auroral activity - data recorded and analyzed
September 8	Several moderately disturbed satellite passes	No aurora
September 9	Satellite scintillation moderate, no detailed correlation with auroral echoes	Aurora observed and recorded
September 10	Several satellite passes observed and recorded	No trace of aurora
September 11	Computer failure no data obtained	

TABLE 7 Summary of the results of operations in which the occurrence of scintillation of satellite signals was compared with the occurrence of auroral clutter.

IV. Auroral Studies

a) L-Band Backscatter Measurements

The period covered in the present report has to a large extent been devoted to developing observing and display techniques rather than conducting extensive observations. A primary reason for the lack of observations has been the limited availability of the radar caused by installing and testing the Frequency Selective Subflector.

The STARE program developed for auroral studies has been described previously (Evans 1969a). For these measurements the radar alternately transmits 50 μsec and 500 μsec pulses. The former serve to give a fairly detailed power profile, the latter a spectral resolution of 2 kHz, but with only approximately 100 km range resolution (i.e. with fairly severe range smearing). Originally it was intended that an intensity-modulated film display be produced of signal power versus range and frequency from the spectral data, and a similar display of power versus range from the range data. Work on these displays has been completed, but it was found that the processing time for each frame amounts to several seconds, and hence to display data taken with 80 msec time resolution requires extremely large amounts of computer time. These displays will therefore only be used to examine special events. A difficulty encountered with the data taken during 1969 was the apparent lack of alignment between the range assigned to the spectral and the profile data. This problem was traced to the original data-gathering (STARE) program and corrected. A frame of the film is shown in Figure 29.

A number of other display programs designed for Calcomp plots have also been developed to go with the STARE program. These can display contours of power as a function of azimuth and range for constant elevation angle or contours of power as a function of elevation and range. Other programs display the center frequency of the return against range and azimuth or the half power spectral width against the same coordinates. Several examples of such displays are shown below. No attempts have yet been made to

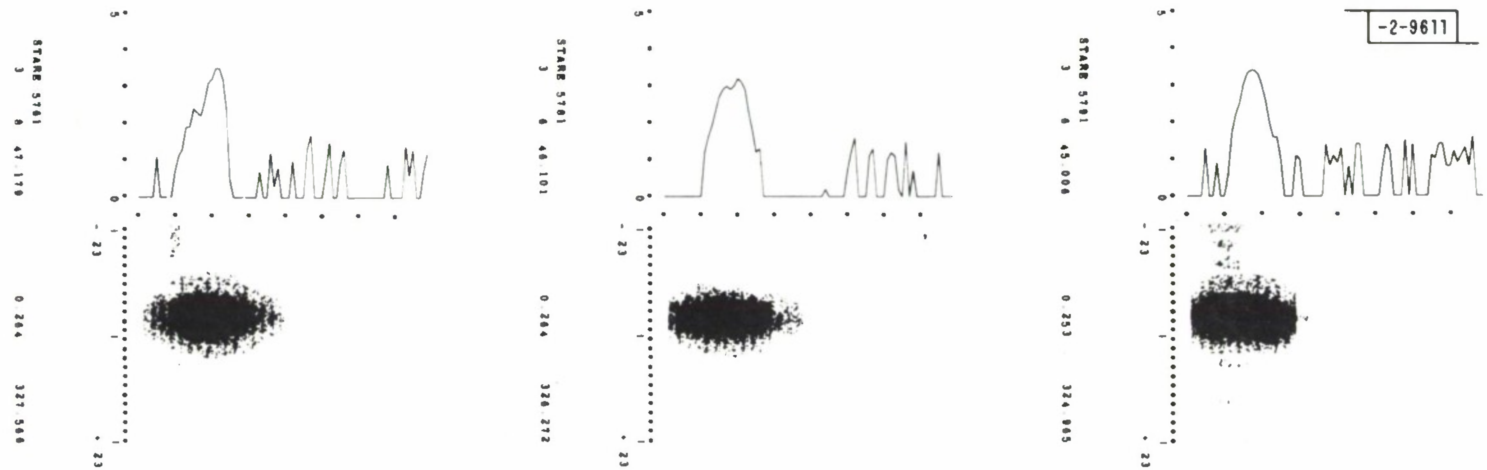

Fig. 29. Frames taken from film of computer-drawn display showing results of STARE (Short Time Analysis of Radar Echoes) program used to gather data on auroral returns. In each frame, Doppler shift of echoes is indicated from left to right over the range -23 to +23 kHz, and range is indicated by vertical distance. Intensity of echo is represented by shading. At left is a plot of total echo power (log scale) as a function of range observed with a short (50 μsec) pulse. Across the bottom are, respectively, time (hrs, min, sec, GMT), elevation (°), and azimuth (°).

remove the effect of the polar diagram and the pulse length on the results so that the true distribution of scattering cross section can be recovered automatically, though a procedure for doing so has been worked out. Grid-lines of L-shell parameters and aspect angles will also be added to the plots.

A search for auroral events with the corrected STARE program was conducted between March 24 and April 26. Altogether 15 afternoons and evenings were available for this search; auroral echoes were observed during 13 of these searches for periods which, in some cases, were quite short.

In Figure 30a-c results are shown for a particularly interesting set of azimuth scans made at true elevation angles of 0.04°, 0.58° and 1.15°, respectively. The cross section per unit volume--as indicated on the plots by log (CS)--turns out to be the same in the three plots to within less than 1 dB. From observations made both prior to and following the ones shown in Figure 30 we conclude that the time variation of the scattering cross section throughout the volume explored is very slight. The apparent altitude of the peak of the echo region in the three plots ranges from 111.6km to 112.8km. We also note that the peak echo intensity appears to fall almost exactly on the same aspect angle ($+0.5^\circ$) in the three cases. It is, therefore, strongly suspected that the magnetic field model used (Sec. IVb) predicts the direction of the magnetic field erroneously by an amount of 0.5°. Assuming this to be the case and assuming approximate spatial homogeniety, which is best justified for the intermediate elevation angle (Fig. 30b) one can deduce the variation of echo strength with off-perpendicular angle. This is obtained from the azimuth variation of echo intensity at the range of maximum return. On this basis it is concluded that for L-band echoes the scattered power falls to half its peak value at an off-perpendicular angle of 0.4°.

In a similar manner a study of the variation of echo intensity along a line of constant aspect angle can be translated to an apparent layer thickness. In this way the apparent thickness between points of half peak

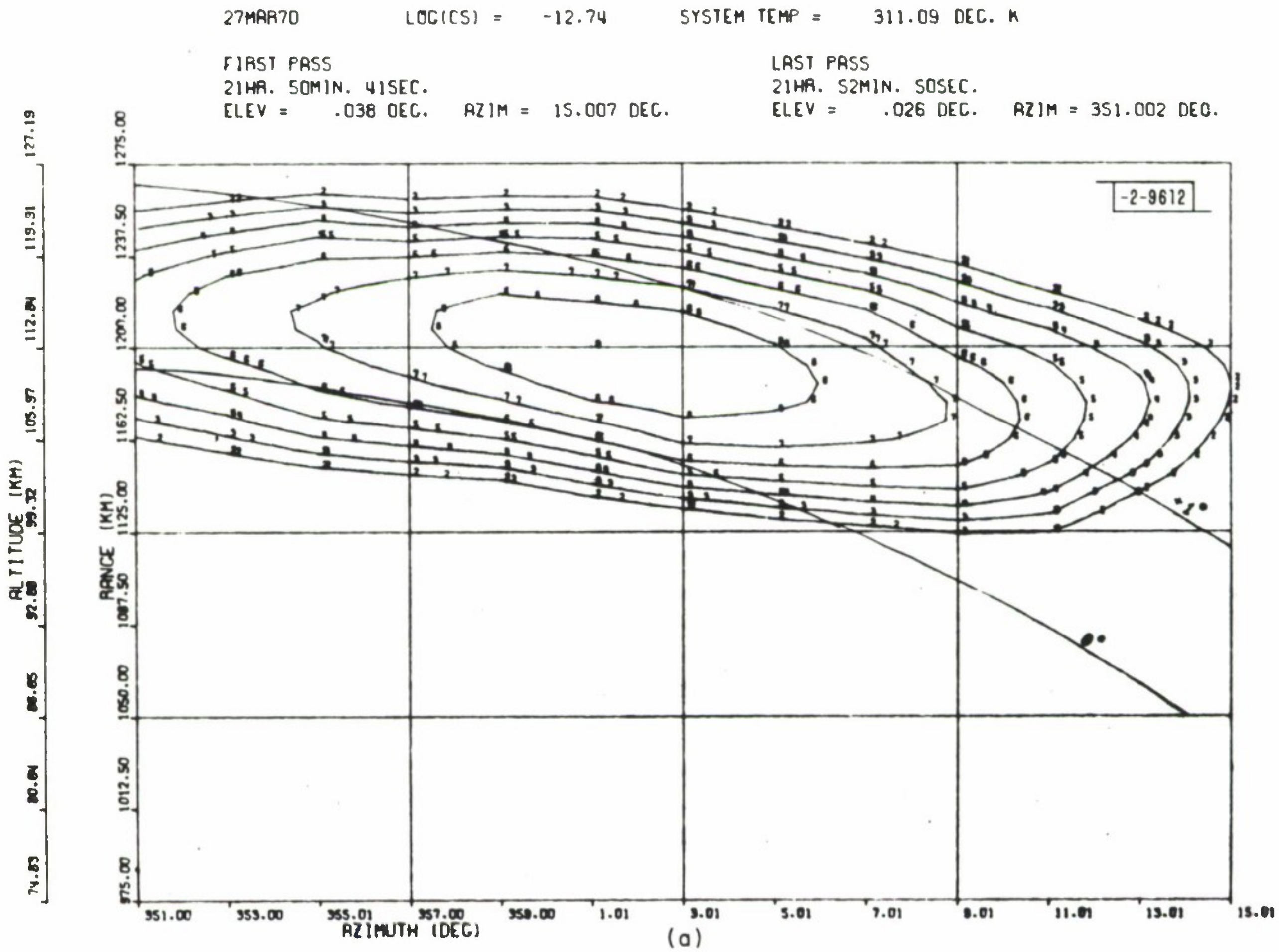

Fig. 30. Contour plots of auroral echo intensity vs range and azimuth. Each contour represents a -2 dB step from most intense echo observed. Also shown are locci for off-perpendicular angles of 0 and +1°. Height scale (at left) is for center of radar beam which is, however, about 10 km wide at these ranges. These measurements were made by integrating returns in a digital computer for a number of azimuths at fixed elevations of (a) .04°, (b) 0.6°, and (c) 1.15°.

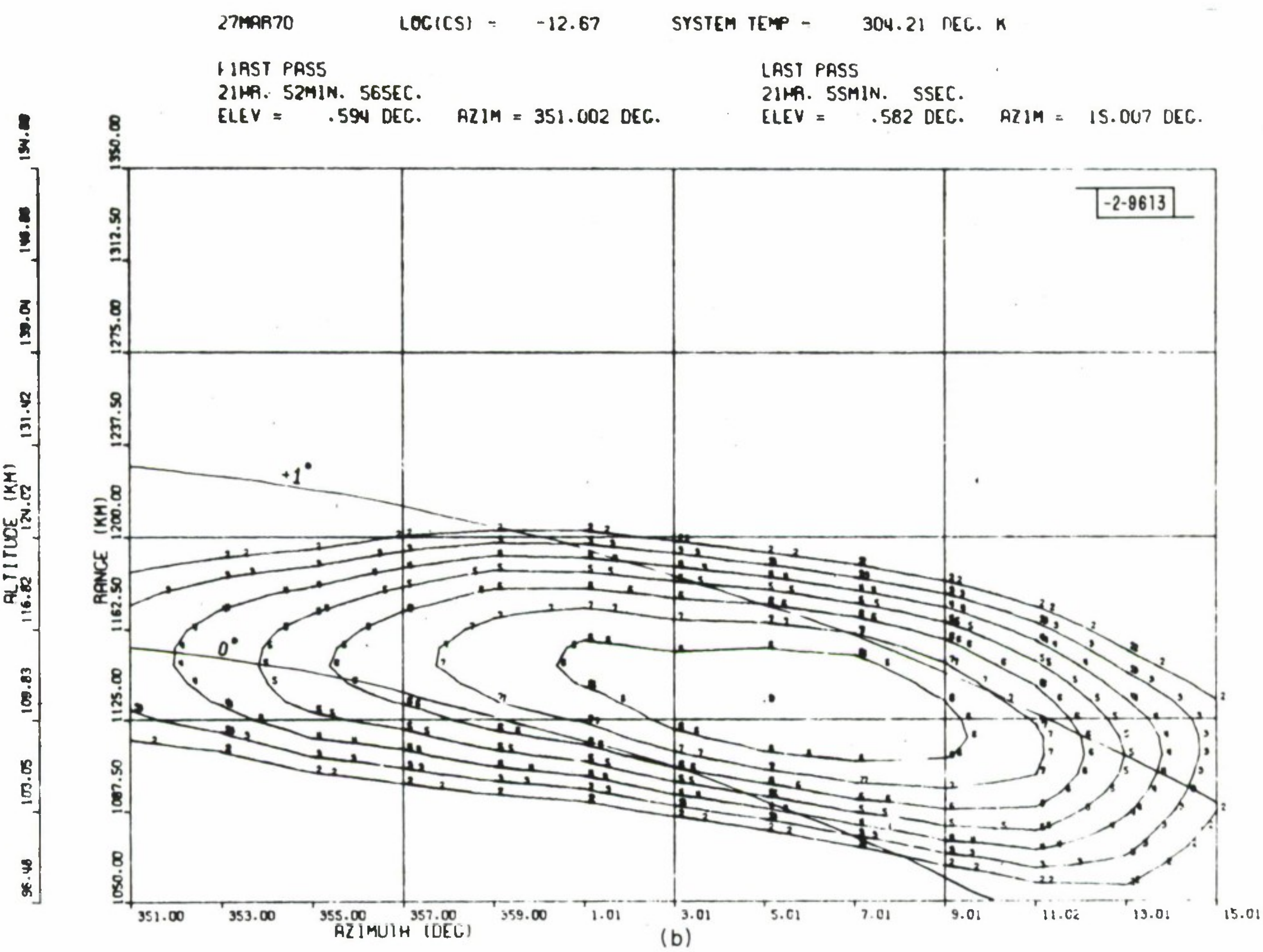

Fig. 30. Continued.

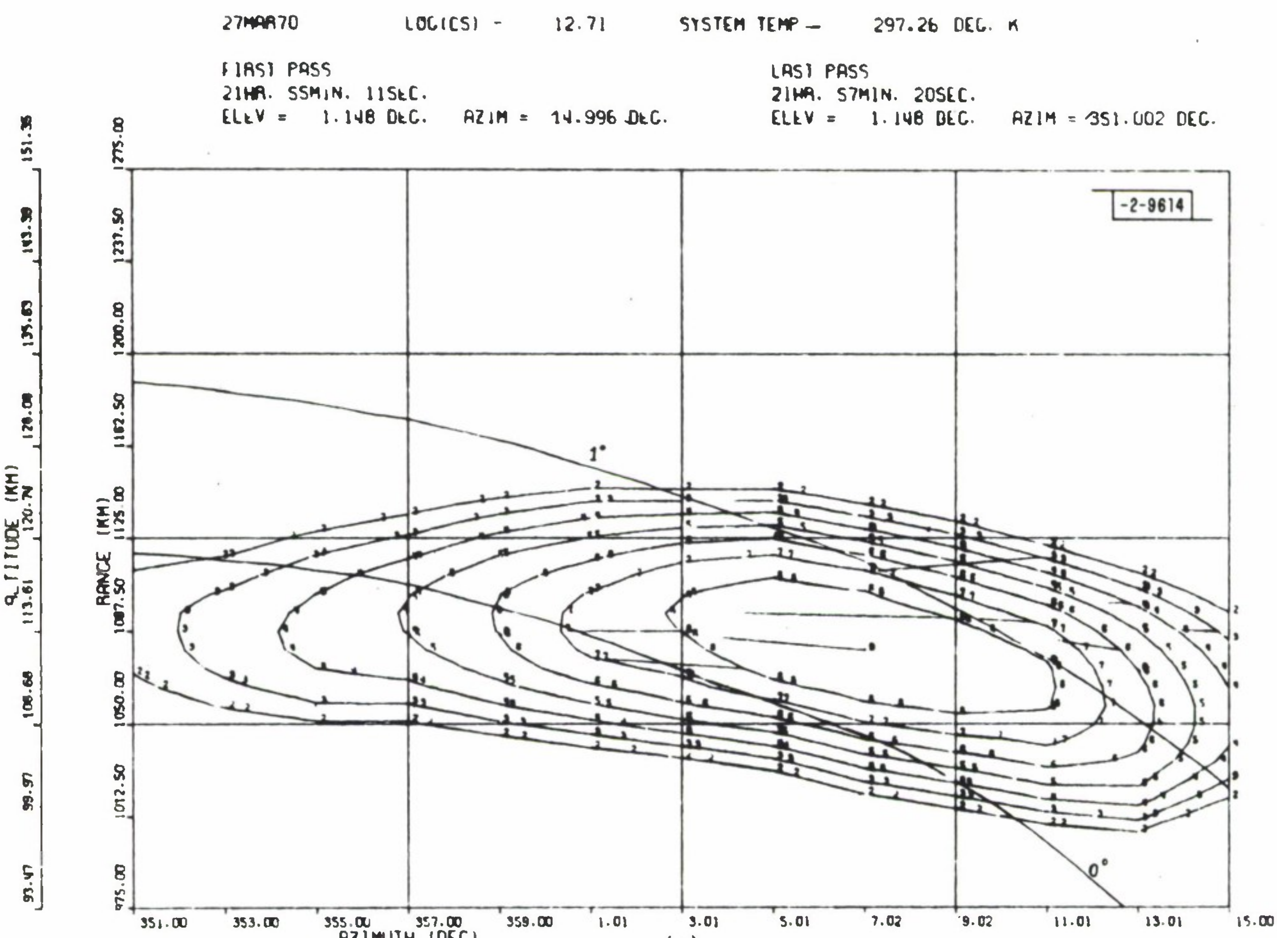

(c)

Fig. 30. Continued.

cross section is found to be 11.2km. Since the Millstone antenna beamwidth between half power points is 0.6° the true layer thickness must have been about 7 km.

The spectra associated with the three azimuth scans just discussed are relatively uninteresting. They show a frequency displacement of 2.5 kHz indicating an approaching velocity. At the same time the spectral width is about 6.5 kHz between half power points. The spectra are therefore not typical of those generated by the two-stream instability mechanism which is discussed below.

We believe that the limited range and frequency resolution available in the present STARE spectrum program makes it difficult to identify the mechanisms giving rise to the auroral echoes. For this reason a procedure used in the incoherent scatter program to obtain fine range and Doppler resolution has been modified and adapted to the auroral radar program. This procedure amounts to transmitting two successive pulses with variable separation or lag, and determining the correlation between samples of the received signal taken with the same lag. In this way, it is possible to obtain arbitrary range and frequency resolution. This increase in resolution, however, must be purchased at the cost of increased integration time.

The fine range and frequency resolution obtained in the new scheme is achieved by transmitting two pulses of 50 μsec each and stepping their spacing on the timebase from zero to some maximum shift in steps of 50 μsec. Zero shift amounts to transmitting a single pulse, 50 μsec in length, and a lag of 50 μsec corresponds to transmitting one 100 μsec pulse etc. With 32 shifts, an equivalent frequency resolution of 312 Hz is achieved, and a total frequency band of 20 kHz is covered unambiguously. At the same time a range resolution is obtained which is largely determined by the width of the pulse, i.e., for a 50 μsec pulse it is slightly more than 7.5 km depending on the receiver bandwidth. A number of observations have been made using this scheme, and three sets of spectra representing some of the results are shown in Figure 31 a-c. The altitudes indicated

in these Figures correspond to the position of the center of the beam, and the different spectra are for echoes at a range spacing of 7.5 km. Figure 31a shows a group of spectra that do not have the character that would be expected for the Farley-Buneman two-stream excitation mechanism. In fact, they are broad and the peak power has a Doppler shift that is less than that of a wave traveling at the ion acoustic velocity. By contrast, the spectra shown in Figure 31b and c are good examples of echoes expected for the two-stream excitation mechanism; they show narrow spectra centered on the expected frequency offset (given approximately by the speed of sound for the ions). We conclude from these results that at least two types of scattering mechanisms are in operation in the auroral electrojet.

b) Coordinated Satellite-Radar Observations

Radar observations made by Leadabrand and Hodges (1966) in Homer, Alaska, at frequencies of 139 and 398 MHz have suggested a close association between the presence of auroral echoes and the precipitation of electrons with energy in excess of 2 keV. Because of the limited observational material available, and also because of lack of a clear understanding of the reasons why such a relationship should exist, it was decided to coordinate some of our radar auroral observations with the passage of the satellite OV1-18. This satellite contains a number of instruments for observing precipitating electrons and protons (see previous report, Evans 1969a). In this experiment the mean orbital elements of the satellite are used to predict the occurrence of favorable passes. For these, the satellite trajectory was projected down along magnetic field lines to determine the locus of points where the radar beam from Millstone Hill intersects the field-line at right angles, or the locus of points at a height of 107 km, i.e., where auroral echo activity appears to maximize. The magnetic field model used in these projection procedures was calculated from the Hendricks and Cain multipole coefficients (see L. Coury 1968). The calculations carried out for several OV1-18 passes showed that the height to the point of perpendicular intersection of the beam and the magnetic field

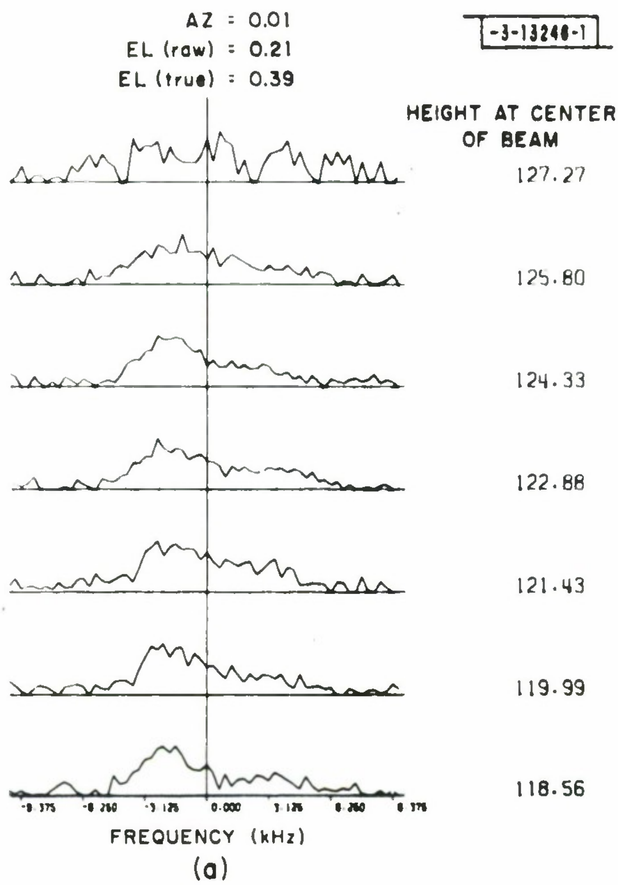

(a) An example of "drifting irregularity" type echoes.

Fig. 31. Spectra of auroral echoes observed at different ranges using double-pulse method of measurement described in text. Corresponding height of center of beam is shown at right and echo power vs range at left.

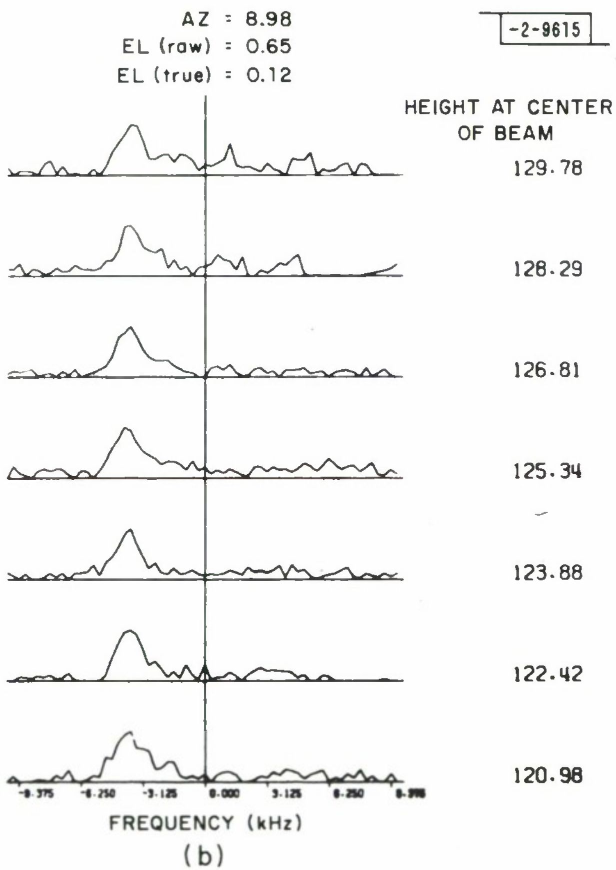

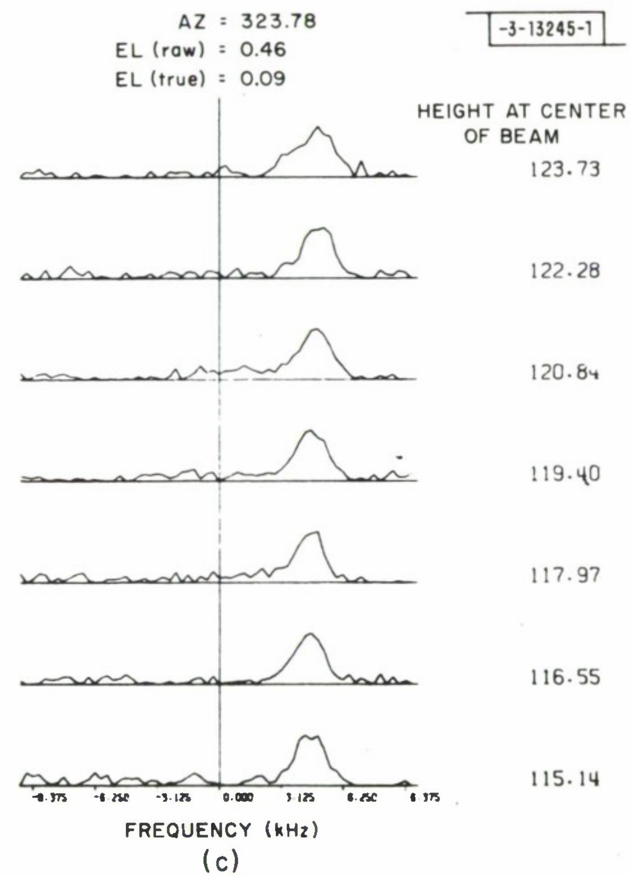

(b) Two-stream instability echoes; auroral current has component away from radar.

(c) Two-stream instability echoes; auroral current has component toward radar.

Fig. 31. Continued.

generally changed very rapidly during the pass. On the other hand, the aspect angle at a constant height remained reasonably constant and for many passes stayed within 1.5 degrees of being perpendicular to the magnetic field during the entire pass. Hence, we chose to track the projection of the satellite orbit onto a plane above ground. This procedure should serve to maximize the correlation between the events seen by the satellite and those seen by the radar. A standard refraction table was used to allow for tropospheric refraction effects.

During the time of a satellite pass, the antenna would scan along the pre-calculated trajectory of the projection point in order to determine the spatial distribution of echo intensity. Later this could be compared with the particle measurements on board the satellite. These correlative measurements were carried out at Millstone from March 27 to April 26, 1970, using the STARE mode of operation described in the previous subsection. During this period there was one particularly favorable pass of the satellite OV1-18 on revolution 6008. Fortunately, during this pass, which occurred in the early afternoon, strong auroral echoes were observed along the predicted trajectory. In what follows, we describe the results of the observations obtained during this pass.

Figure 32 shows the predicted range from Millstone and the aspect angle with respect to Millstone at an altitude of 107 km, both plotted versus Universal Time. Calculations made after the pass, based on more accurate orbit data, showed that the orbit trajectory predictions were accurate to within 2 km, but that the pass occurred 6 sec later than predicted. Because the gross spatial structure of the radar aurora changes little during such short time intervals, this time discrepancy is not significant. At $20^h\ 30^m\ 27^s$ the predicted projection point at 107 km passed below the radio horizon.

The STARE program was used with the integration time set to be 3 sec. Thus with an interpulse period of 40 msec, 75 pulses are summed into each integration period. Table 8 lists the azimuths and elevation angles for

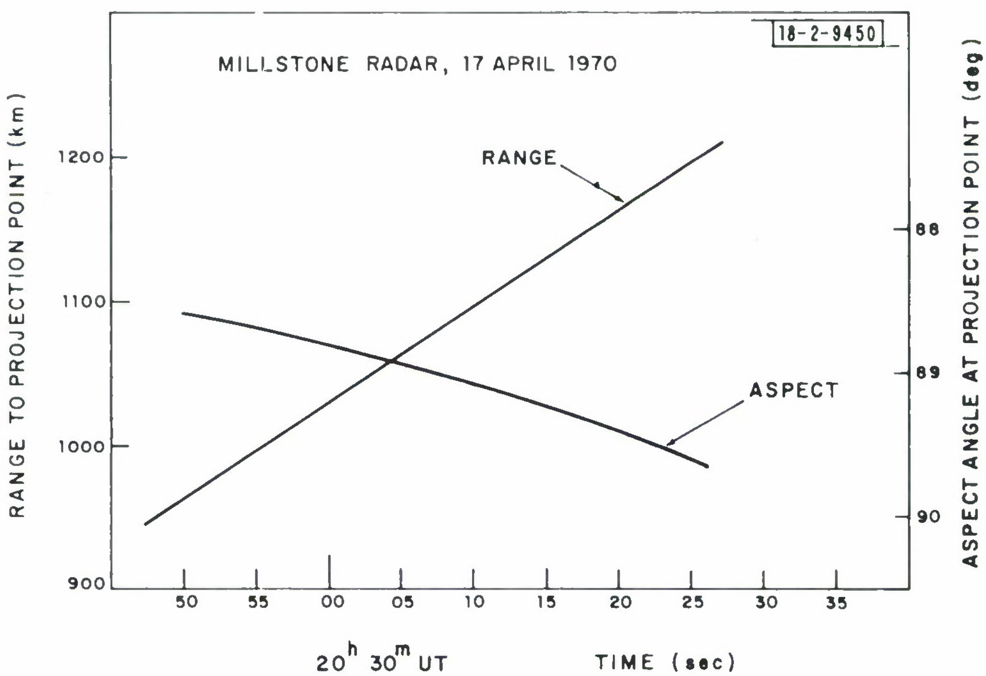

Fig. 32. Range and aspect angle to magnetic field line at 107 km altitude that connect to path of OV1-18 satellite for pass on 17 April 1970.

the six runs made during the pass. The range to the point tracked by the radar was converted to the equivalent geodetic latitude of the satellite for easy comparison with the various particle detectors on board the satellite. Figure 33 shows the radar cross section per unit volume obtained for the six runs. The pulse width used to obtain these curves was 50 μsec, the receiver bandwidth 100 kHz, and the range resolution was therefore approximately 7.5 km.

Run	Azimuth	True Elevation
I	339.77°	0.70°
II	339.79°	0.23°
III	339.85°	0.10°
IV	339.97°	-0.31°
V	339.99°	-0.49°
VI	340.04°	-0.64°

Table 8 Particulars of Radar Runs Carried Out on 17 April 1970 during a Pass of OV1-18 Satellite

If it is assumed that during the brief observation interval the scattering behavior did not change, it is possible to deduce, from the elevation angle dependence of the echo power observed at a given range, the height and the thickness of the scattering layer. In order to simplify the task, the beam pattern of the antenna was approximated by cylindrically symmetric function with a Gaussian cross section whose half power width was made 0.6°. The layer was also assumed to have a Gaussian cross section in the vertical plane. The height of the layer peak and the thickness were left free to be determined by the observations (Fig. 33). By carrying through such a fitting procedure, it was possible to construct a contour diagram of scattering cross section as a

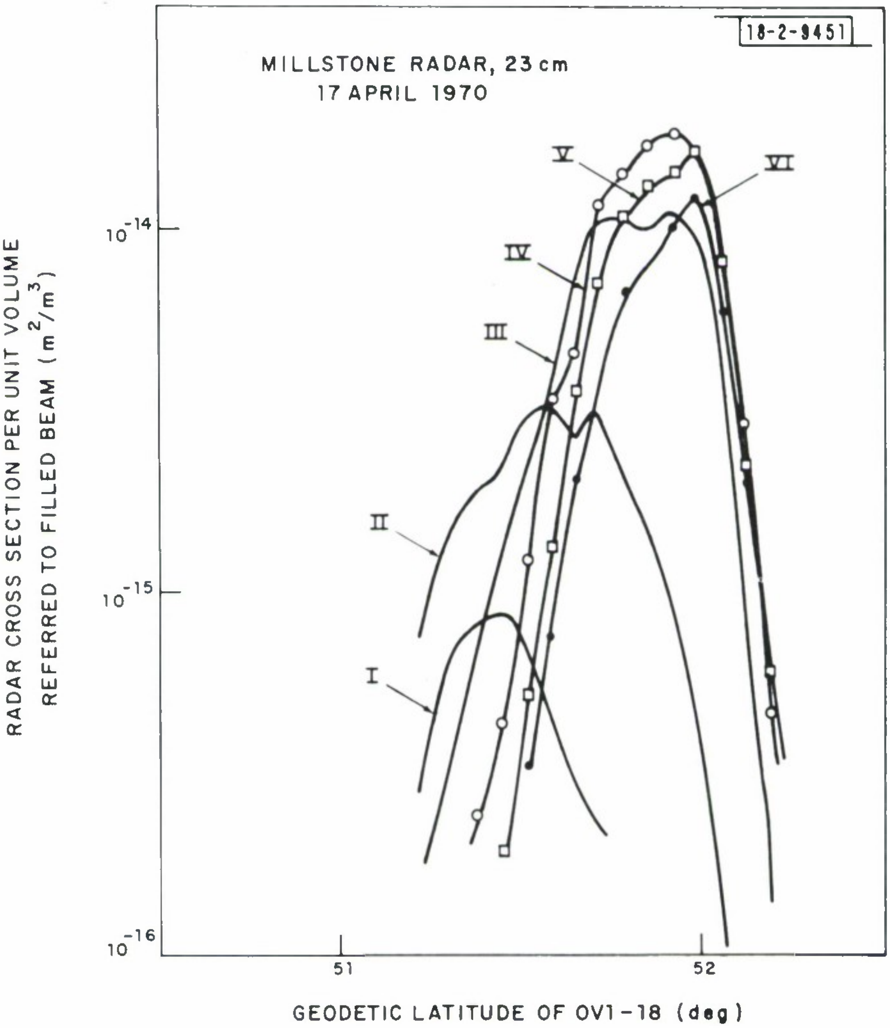

Fig. 33. Auroral radar echo cross sections vs geodetic latitude of OV1-18 satellite for measurements made at elevations and azimuths listed in Table 6.

function of height and the geodetic latitude of the satellite, as shown in Figure 34. The contour levels are in 2 dB steps and the 20 dB level corresponds to a cross section of 10^{-14} m^2/m^3. As can be seen there is a steady increase in echo intensity with latitude toward the point where the echoing region disappears below the horizon. The height of maximum intensity is at 112 km, and there is a tendency for the height to decrease somewhat with increasing latitude. This height dependence could be caused by the aspect sensitivity of the returns. The point of exact perpendicularity to the field lines lies above 112 km by an amount that is decreasing with increasing latitude. We also note that the echoes extend down to satellite latitude of 51.2°.

The frequency spectra of the returns in the six runs (Table 8) were obtained with a frequency resolution of 2 kHz over range intervals of 75 km. The results are shown in Figure 35 where it can be seen that the half power widths of the spectra are typically 5 kHz, and the center of the spectra are all displaced toward negative offsets corresponding to motion away from the observer. This is in agreement with previous measurements made by Abel and Newell at this azimuth and time of day. The negative frequency offset is approximately 1.5 kHz, and would correspond to a drift velocity of 200 m/sec. If this motion were due to an electric field applied in the east-west direction, the required strength of the field would be about 10 mV/m.

The particle detector outputs from the satellite OV1-18 were supplied by Lockheed Missiles and Space Company through the cooperation of Dr. R. D. Johnson. The outputs of three groups of electron counters and one group of proton counters were made available to us. Details of the various counter outputs are given in Table 9.

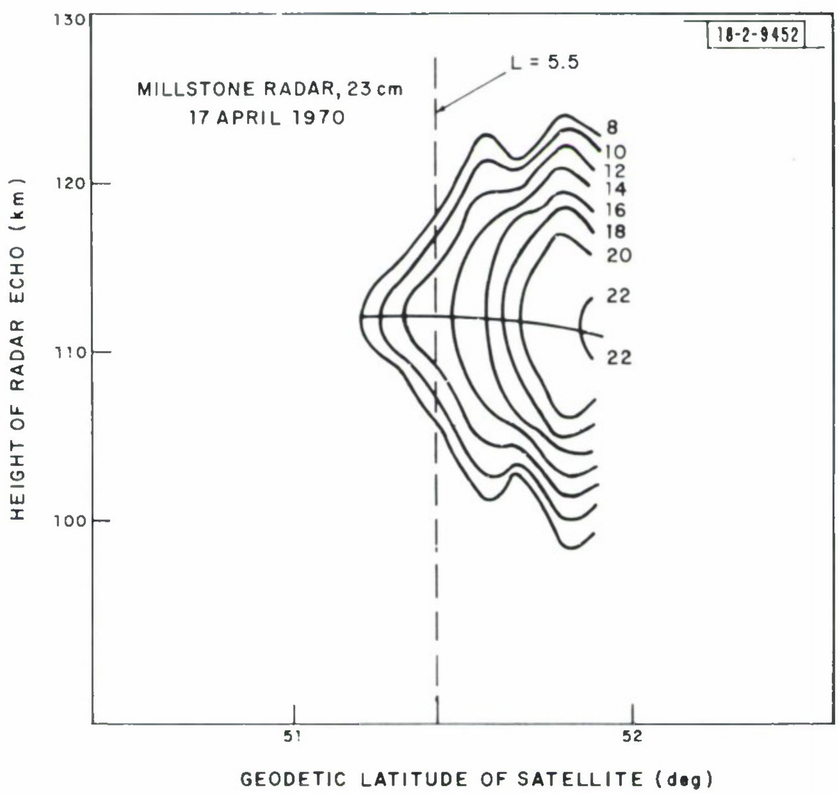

Fig. 34. Contours of constant echo cross section (in dB) as a function of height and geodetic latitude of OV1-18 satellite for observations made during pass on 17 April 1970.

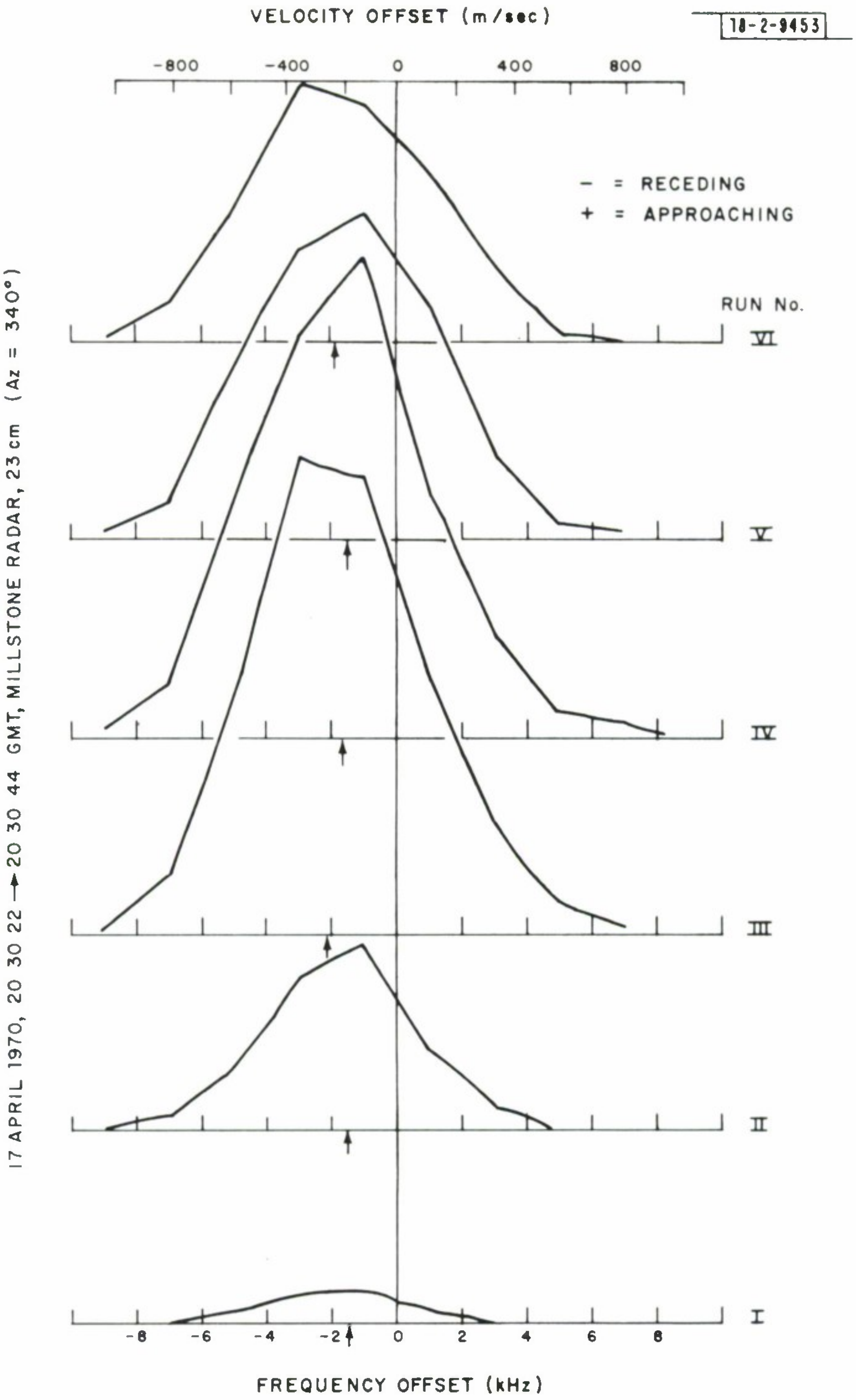

Fig. 35. Spectra of auroral echoes observed with filter bank for measurements made on 17 April 1970 during OV1-18 satellite pass at elevations and azimuths listed in Table 6.

Particle	Group	Energy
electrons	0°	1.2, 2.5, 5.4, 12.3, 27.2 keV
electrons	55°	1.2, 2.5, 5.4, 12.3, keV
electrons	90°	1.2, 2.5, 5.4, 12.3 keV
protons	55°	> 4, >10, >25, > 50 keV

Table 9 Particulars of Particle Sensors for the Observations on 17 April 1970

For the pass under discussion, the various electron counters showed pronounced precipitation at satellite geodetic latitudes between 55° and 59° but no trace of precipitation between 51° and 52° where the auroral echoes were observed (Figures 33 and 34). An example of the output of the electron sensors in one group is shown in Figure 36. Examination of the 55° proton group, however, shows significant proton precipitation in all of the three sensors with lower energy limits of 4, 10 and 25 keV as shown in Figure 37 beginning at a geodetic latitude of approximately 51.5. Unfortunately, at the present time the results have not been converted to absolute flux values. The output of the sensor with $E_p > 25$ keV was replotted from the digital printouts and carefully aligned with geodetic latitude according to the best ephemeris and the satellite clock. The result is shown, though again without absolute calibration, in Figure 38. Comparing this diagram with that of Figure 34, we observe that the southern edge of the proton precipitation peak corresponds very closely to the position of the edge of the region giving rise to auroral echoes. This close correlation of the proton peak with the position of the auroral echo region suggests an association of afternoon auroral echoes and proton precipitation. However, as long as the absolute flux calibrations are not available, it is not possible to conclude anything definite about the exact relationship of the particle precipitation and the auroral radar echoes.

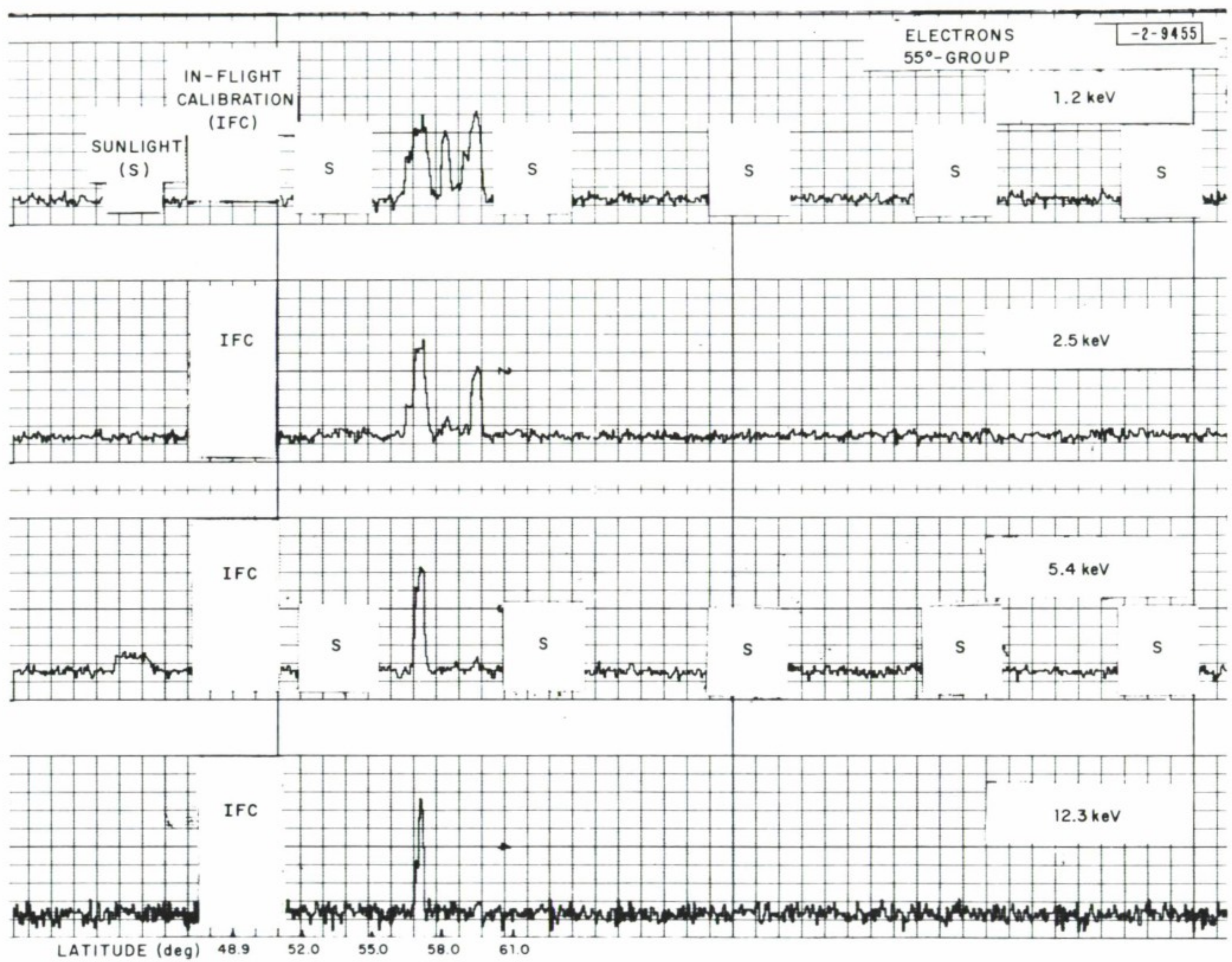

ELECTRON COUNTER OUTPUT, OV1-18, 17 APRIL 1970

Fig. 36. Records of electron analyzers on OV1-18 satellite during pass on 17 April 1970. Periods blanked and marked S were those in which sun entered sensors. No electron precipitation was recorded over latitude range where auroral echoes were observed.

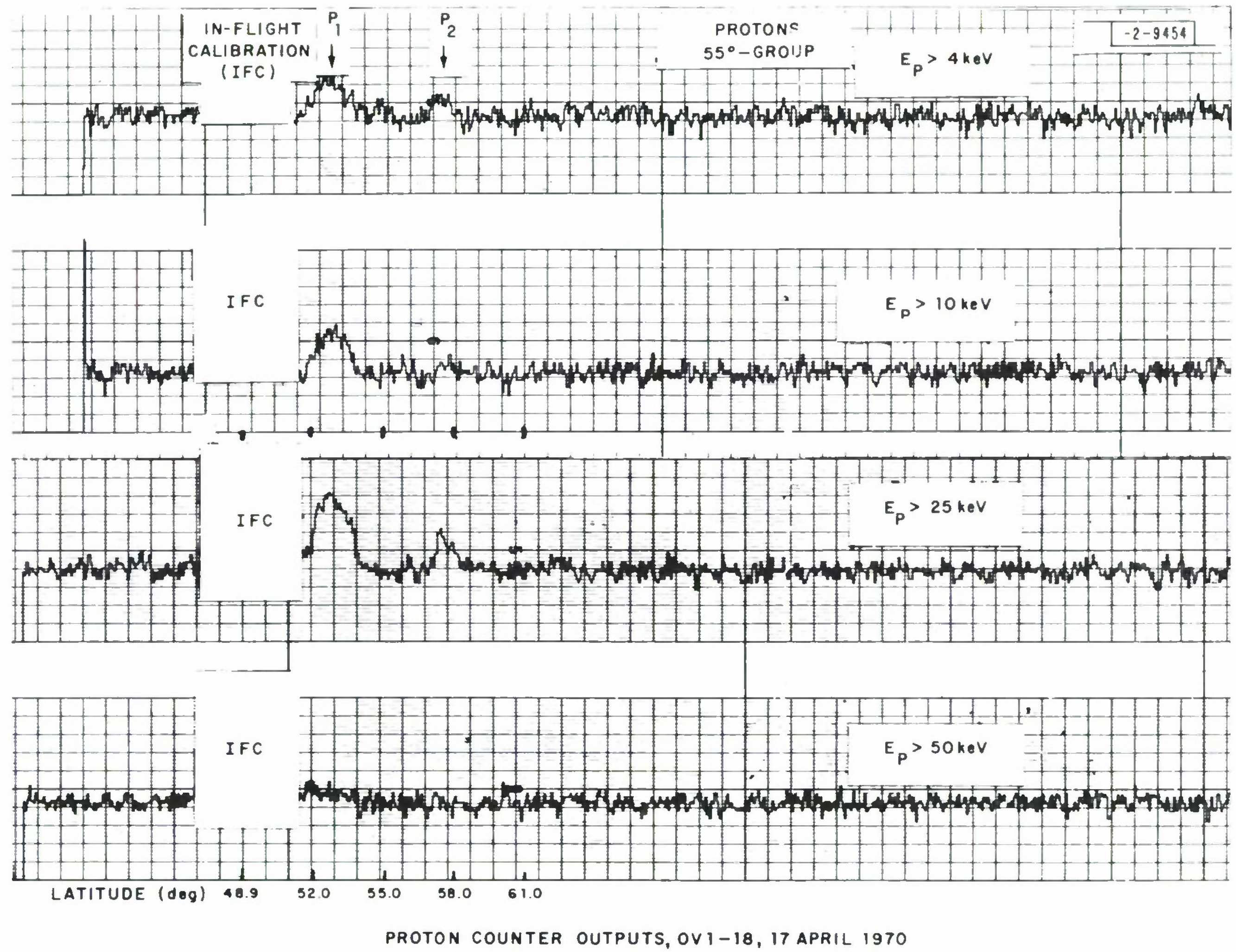

Fig. 37. Records of proton analyzers on OV1-18 satellite during pass on 17 April 1970.

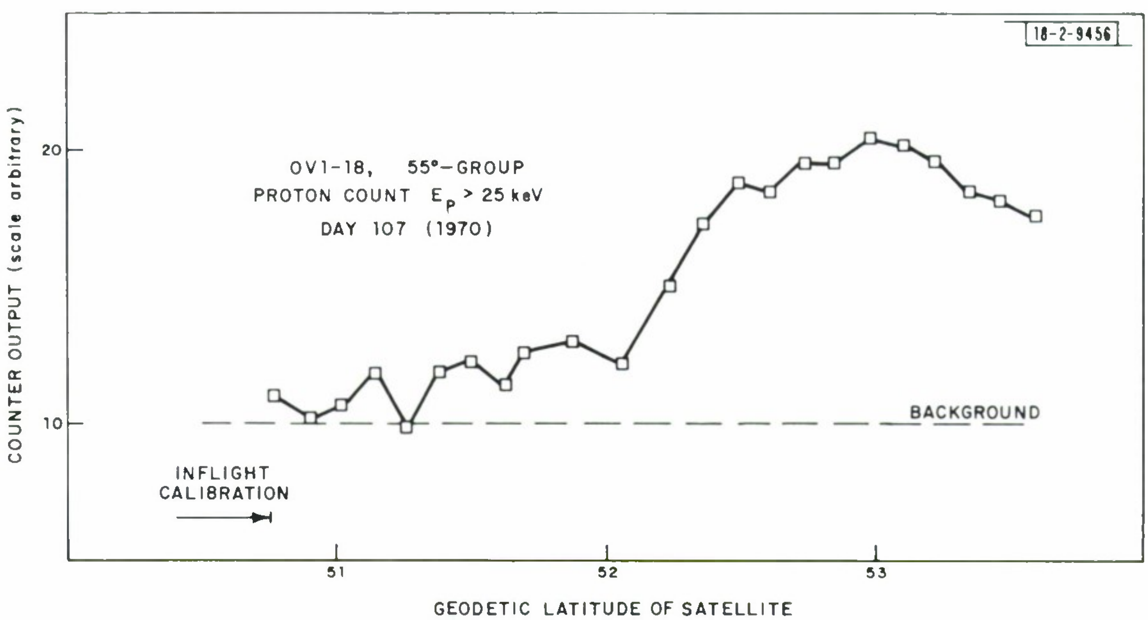

Fig. 38. Proton precipitation intensity as a function of geodetic latitude of satellite on 17 April 1970.

A hypothesis which might reconcile the previous observations which showed an association between nighttime auroral echoes and electron precipitation with the very different findings reported here for one afternoon case is needed. If the proton precipitation peak is somehow associated with an increase in electric fields, normal to the magnetic field lines, it would be possible to explain the afternoon results. Electric fields will cause the plasma density to contain small scale irregularities either through the Farley-Buneman type of microscopic resistive instability (Farley 1963), or through an instability involving a gradient in plasma density and an electric field as discussed by Cunnold (1969), Rogister and d'Angelo (1970) and others. These small scale irregularities may be detected by the radar only if the mean background density is high enough. During the daytime, the background density would probably be high enough for the irregularities to be observed but at night when Leadabrand and Hodges made their observations, additional ionization or large ionization gradients caused by electron precipitation may be required to render the density fluctuations "visible" to the radar.

Obviously further coordinated satellite - radar observations are required to test the exact relationship of particle precipitation and auroral clutter echoes. Unfortunately the OV1-18 satellite tape recorder failed during the summer of 1970, thus preventing further studies planned for the fall. At the present time there is no alternative satellite that is suitable.

c) Theoretical Studies

In order to establish the relationship between the occurrence of auroral echoes and F region refraction effects we have sought to understand the mechanism that gives rise to the echoes. From the evidence presented in Sec. IVa) it seems very probable that some (though not all) auroral irregularities are produced by the two-stream instability mechanism in the auroral electrojet. This instability mechanism is primarily responsible for irregularities of a few meters in size. At equatorial latitudes it has been noted that the two-stream instability associated with the equatorial electrojet

is apparently not the only cause of ionospheric irregularities observed there. It seems that this conclusion applies equally to auroral latitudes. Other well known instability mechanisms have been considered therefore. The $\underline{E} \times \underline{B}$ type of instability that arises because of the presence of gradients in the electron density was examined. This mechanism depends upon the plasma moving (with velocity v) perpendicular to both the density gradient and the magnetic field. However, in order for ionospheric irregularities to be produced in this way, the motion must possess a particular sign. This constraint seems in conflict with the observation that irregularities appear to be present at the Equator in the E region almost continuously. For this reason an investigation of other instability mechanisms was undertaken.

We have considered whether instabilities may arise as a result of a gradient of electron temperature. It has been determined that a low frequency mode of instability can arise in a partially ionized plasma containing an electron temperature gradient aligned perpendicular to a magnetic field. The irregularities so produced are essentially thermal in nature but are associated with related electron density fluctuations. The physical reason for the existence of instability is that the plasma is driven in the direction of the electron temperature gradient due to an induced electric field which produces an $\underline{E} \times \underline{B}$ type drift. Under certain conditions the higher temperature plasma is driven in the opposite direction from the lower temperature plasma. Instability may then result because of the existence of an electron temperature gradient. The unstable mode is found to propagate at approximately the drift velocity of the electrons in a direction which is essentially perpendicular to the magnetic field lines.

An additional requirement for this instability is that there should exist an electron density gradient having a component in the direction of and with the same sign as the electron temperature gradient. It is also necessary that the scale for the electron density variation be at least a factor 7/3 greater than the scale of the electron temperature variation. Application of this instability to the ionosphere has been considered. It is found

that the energy loss from the electron gas by virtue of collisions with ionized and neutral particles prevents the occurrence of this instability under most ionospheric conditions. If electron temperature variations on the scale of a few kilometers were to exist in the auroral ionosphere, however, field aligned irregularities of size 10-100 meters could be produced at altitudes above about 140 Km. Thus, the instability could account for auroral echoes seen at HF at altitudes above the level where most of the UHF echoes are found, but does not appear to explain the "drifting irregularity" type of echo (Fig. 31a) that we frequently observe.

V. Ionospheric Studies

a) Introduction

As discussed in Section III, it is necessary to distinguish between two types of refraction, namely, the gross bending of the rays due to the combined effects of the troposphere and the ionosphere, and a random fluctuation about this value introduced by small-scale irregular structure drifting through the ray-path. The random fluctuation, generally termed scintillation, causes the apparent position (and size) of the target to wander around its mean value with a fluctuation period of the order of a second or less. Irregularities responsible for such fluctuations appear both in the troposphere and the ionosphere in a time-varying manner. Ionospheric irregularities are almost always present in the F-region in the auroral zones, and may be caused by the precipitation of low energy particles (Cherkas 1969). Irregular scintillation is of serious concern in precise angle tracking because it places a fundamental limit on the tracking accuracy that can be achieved.

Large-scale refraction is amenable to prediction, and hence its effects on precise tracking, in principle, can be removed. On the other hand, large-scale refraction is more insidious in that there is no immediately recognizable signature to warn of its presence.

In conducting studies of these two phenomena, we are beset with measurement problems that are very different. In the case of angular scintillation, it is possible to employ the mean position of the target or source as a reference, and merely determine the extent to which the apparent position deviates from this direction. In the measurement of large-scale refraction there is no readily available reference position so that absolute measurements must be made. These require a) that the pointing control and readout system for the antenna be extremely precise, b) the gravitational deflections of the structure at different elevation angles be calibrated, and c) the extent to which wind can cause deflection be understood. In

the case of ionospheric refraction, it is possible to circumvent some of these difficulties by making use of the inverse square dependence on frequency which this obeys. Accordingly, we are making observations of the angle-of-arrival at two frequencies (UHF and L-band using the same antenna system). This scheme eliminates most problems associated with the antenna readout system, but does not entirely remove effects due to wind or gravity-induced deflections owing to the different antenna feed arrangements for the two frequencies (Figure 1).

As illustrated in Figure 39 the problem of examining large-scale refraction effects can be approached another way, namely, that of performing ray-tracing calculations for a model atmosphere. The difficulty here lies in obtaining sufficient information to develop an accurate model. Nevertheless, this approach has considerable value for the following reasons:

i) Ray tracing calculations are needed to determine the reasonableness of any large refraction effects uncovered in the observations i.e., they can act as a cross-check on the measurements.

ii) Accurate ray-tracing calculations require good models and thus in conjunction with measurements of refraction serve to indicate the number, quality and types of sensors (Fig. 39) needed to describe the real atmosphere.

iii) Some of the (worst) events occur sufficiently infrequently that the refraction effects they produce are rarely witnessed while others occurring more often tend to be short-lived. In these cases it is useful to attempt to compute the effects as a supplement to attempts to measure them directly.

Included under iii) are a number of naturally occurring phenomena as well as high altitude nuclear bursts.

In this section we describe the observations being made with the existing UHF Millstone Hill incoherent scatter radar in support of the propagation

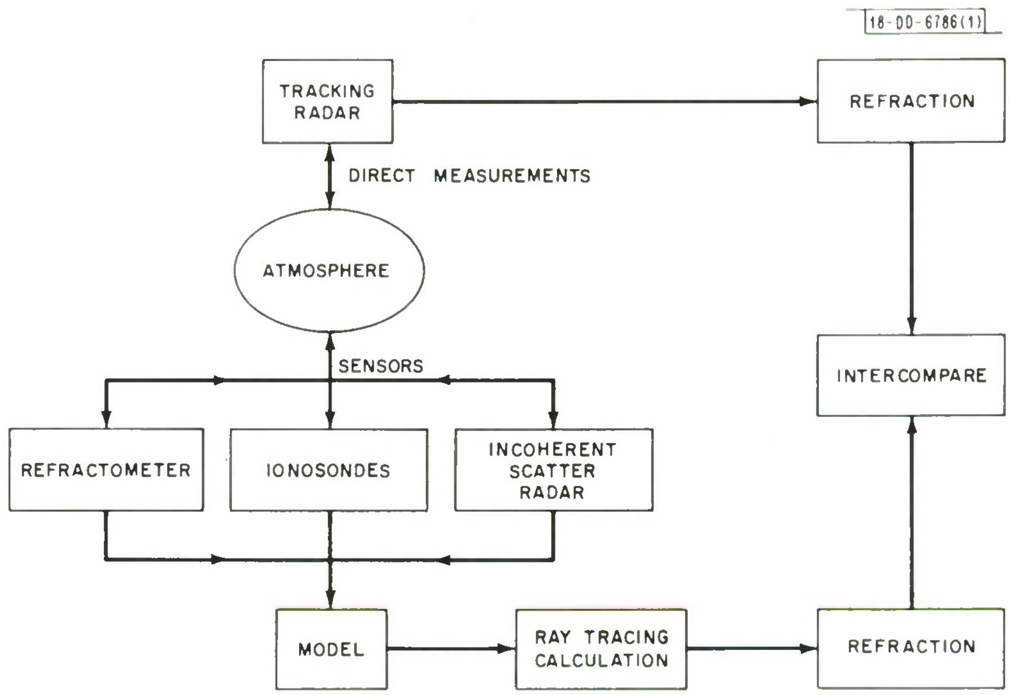

Fig. 39. Model showing means of arriving at estimates of refraction effects in atmosphere.

study program. This radar system employs a fixed 220-foot diameter vertically-directed antenna, thus limiting the observations to a region overhead. Despite this, as discussed below, measurements can be made that directly bear on a number of possible sources of ionospheric refraction that are of considerable concern in the present study. Of even greater utility would be incoherent scatter measurements made with an antenna of the same size, or larger, that could be tilted to low elevations to explore the density variation along ray paths that traverse the auroral ionosphere.

b) The Incoherent Scatter Radar

Studies of the ionosphere at Millstone Hill using the incoherent scatter technique have mostly centered around observing the behavior of the electron density N, electron and ion temperature T_e and T_i in the F2 region. For this purpose the radar is operated in a sequence of modes, each using long pulses, which together yield N, T_e and T_i over the altitude range 200-800 km. These measurements, begun near sunspot minimum, are expected to yield information on the diurnal and seasonal variations in the F2 region over almost all conditions of solar activity. Results obtained in the first years of operation are presented in a series of Technical Reports (Evans 1965, 1967, 1969b) as well as in a number of journal articles. This work originally required much tedious hand analysis of the data, but in 1968 was streamlined by the introduction of new hardware and computer software systems that make the gathering and reduction of most of the data near automatic. These improvements are described by Evans *et al* (1970).

Beginning in 1969 we have sought to extend these measurements to lower altitudes. In order to do this, two problems have had to be overcome, *viz* 1) the presence of interfering clutter echoes out to a range of 150 km and 2) the need to preserve the spectral resolution while improving the height resolution. Various modifications to the antenna to combat low angle radiation have been made, which together with digital filtering in the computer now make it possible to observe the E and F1 regions for much of

the time. New methods of operating the radar at these low altitudes have been developed that yield good height resolution (6 km in the E region) and fine frequency resolution in the spectra of the echoes (from which electron and ion temperatures are derived). These new programs are not yet developed to the point where automatic data processing is possible, but efforts are underway to write the necessary computer programs.

The F2 region measurements (200-1000 km) and the E and F1 region studies (100-300 km) each require about 30 minutes observing time to produce a profile of electron density, electron and ion temperature with the best possible resolution at each altitude. A time resolution of 30 minutes is adequate for most studies of the ionosphere, but is too long to permit rapid changes of density to be followed accurately. Rapid changes are produced by large-scale traveling waves that propagate with velocities of the order of 300 m/sec, and have wavelengths of a few hundred km. Accordingly, a new program has recently been developed that yields electron density profiles in as little as two minutes with sufficient accuracy for ray-tracing calculations. The data processing program for this new measuring technique is well advanced and, besides yielding vertical electron density profiles, provides plots of constant electron density as a function of height over the time of the observations.

In the subsections that follow, we describe the application of these various programs to gathering electron density profiles during two types of transient events, namely, active aurorae, and the overhead passage of traveling ionospheric disturbances. Currently, this work must be done at different times from refraction measurements, owing to the considerable amount of time required to change over between radar systems. Although the necessary engineering work has not been carried out, it is believed that the incoherent scatter radar could be operated to study the overhead ionosphere <u>between</u> passes of satellite observed by the tracking radar (at L-band and UHF). In order to do this, modifications are necessary to permit

a rapid changeover between transmitters and computer programs. The Millstone Hill UHF and L-band transmitters share a common power supply and water cooling arrangement. It is believed that the cooling supply could be modified to permit both transmitters to be left with their filaments on, so that only the high voltage would have to be transferred. The various computer programs could be stored on the computer's magnetic drum, and read into the main memory as needed. We would also place the data interface under control of the computer, as well as selection between the timing equipment that controls the two transmitters. It is hoped that these improvements can be made during the course of the next year's operations.

c. F Region Electron Density above Active Aurorae

Visible aurorae are thought to be produced by the precipitation of high energy particles into the earth's atmosphere. One may liken the process to a cathode-ray tube in which the atmosphere serves as the phosphor and electric fields in remote parts of the earth's magnetosphere act as the accelerating gun. Although it has not been established conclusively, it is thought that the solar wind (i.e. electrons and protons streaming from the sun) provides the source of particles.

The electrons in a primary auroral stream lose energy as they penetrate into the atmosphere by a variety of processes. Ionization of the atmospheric gases is the dominant initial loss process while production of bremsstrahlung X-rays accounts for a negligible small loss when the electrons have an initial energy of 10 keV or less. Ionization occurs into electronically excited states of the ion as well as into the ground state. This is the origin of N_2 and N_2^+ bands, various bands of O_2^+, and atomic lines originating from $O^+(^2P)$ and $O^+(^2D)$, all observable features in the visible, near-ultraviolet, and near-infrared auroral spectrum.

The primary ionizations produce secondary electrons(that may be some 100 times as abundant as the primaries) which cause additional ionization, but lose energy principally in exciting various neutral species to a host of electronic states.

In a typical aurora, peak electron production is thought to occur near 120 km i.e. substantially lower than the height of peak production in the normal ionosphere as a result of solar ultraviolet light. Despite this the F-region density is typically thought to exceed 10^6 electrons/cm^3. Unfortunately it is quite difficult to obtain electron density profiles in auroras with conventional ground-based ionosondes owing to the fact that the E region return is often so intense that it blankets the F-region and/or ionization produced in the D region gives rise to considerable absorption. Topside sounders regularly see regions of high electron density in polar regions (Andrews and Thomas 1969) that are believed to be produced by auroral precipitation. However, from topside soundings it is not possible to obtain the electron density distribution at and below the layer peak where the largest part of the refraction is introduced. Thus until recently the only direct method of obtaining electron density profiles in active auroras was to employ rocket-borne density probes. Unfortunately, such measurements are expensive to make and provide only the distribution at a given instant of time with no clue as to the degree of variability. Incoherent scatter radar measurements, on the other hand, could be used to provide almost continuous monitoring of the electron density distribution, given a suitably located radar with adequate sensitivity.

For the most of the time the Millstone Hill incoherent scatter radar is too far to the south to see auroral activity overhead. On some occasions, however, a magnetic storm may be sufficiently intense to give rise to particle precipitation over Millstone and an instance when this happened was on March 8, 1969. Being alerted to the fact that an aurora was in progress a little after 6 p.m. the radar was turned on and measurements made throughout the night until sunrise next morning with results that are shown in Figure 40.

It can be seen that the principal effect of the precipitation was to produce a layer of ionization below the normal F layer (which had a peak height much larger than normal). This additional ionization gave rise to sporadic E echoes on the ionosonde and hence in Fig. 40 has been labeled as

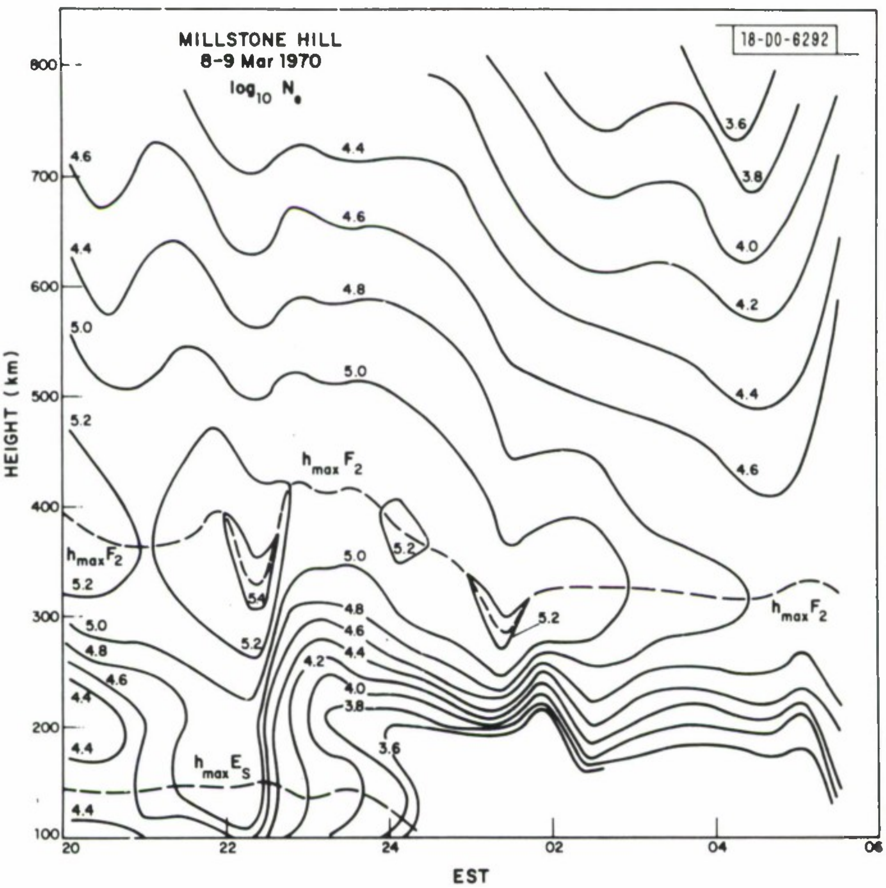

Fig. 40. Contours of electron density ($\log_{10}$) as a function of height and time observed with incoherent scatter radar at Millstone Hill during night of 8/9 March 1970 when an aurora occurred overhead.

E_s. The event appears to have ended around midnight and the layer then settled down to its regular shape but with much lower densities than normal. During the period of actual precipitation the peak F2 density was $\sim 2 \times 10^5$ el/cm^3, i.e. substantially below some values reported in the literature. This may be simply because Millstone was located on the fringe of the precipitation region and did not witness the full effects. The ability to scan the radar beam north would be of great value in deciding such questions.

d) Traveling Ionospheric Disturbances

It has long been recognized from ground-based ionosonde records that large scale waves can propagate in the earth's ionosphere. These waves have been called Traveling Ionospheric Disturbances (T.I.D.) and typically have a wavelength of several hundred km and group speed of several hundred meter/sec. It is presently thought that these waves are a manifestation of gravity waves in the neutral atmosphere, which may be thought of as a surface wave propagating at the interface between the cold denser region of the atmosphere below 100 km and the warmer lighter air above.

There are two energy sources that are known to excite gravity waves, viz. the auroral electrojet and high altitude nuclear bursts. There is also speculation that there may be other sources. At low and high altitudes in the F region the T.I.D. appears to give rise to wavelike contours in a plot of electron density vs time, but near the layer peak produces a series of compressions and rarefactions. Figure 40 provides a good example of the effects of the passage of a T.I.D. although somewhat obscured by the effects of the aurorae; i.e. the F region maxima and minima shown in Figure 40 are thought to be a consequence of the passage overhead of a traveling disturbance generated by the heating of the atmosphere produced by the auroral electrojet.

On rare occasions waves with periods of as long as 3 hours have been observed and Figure 41 gives an example of the density variations observed in such a case. However, the majority of T.I.D.'s have periods of 90

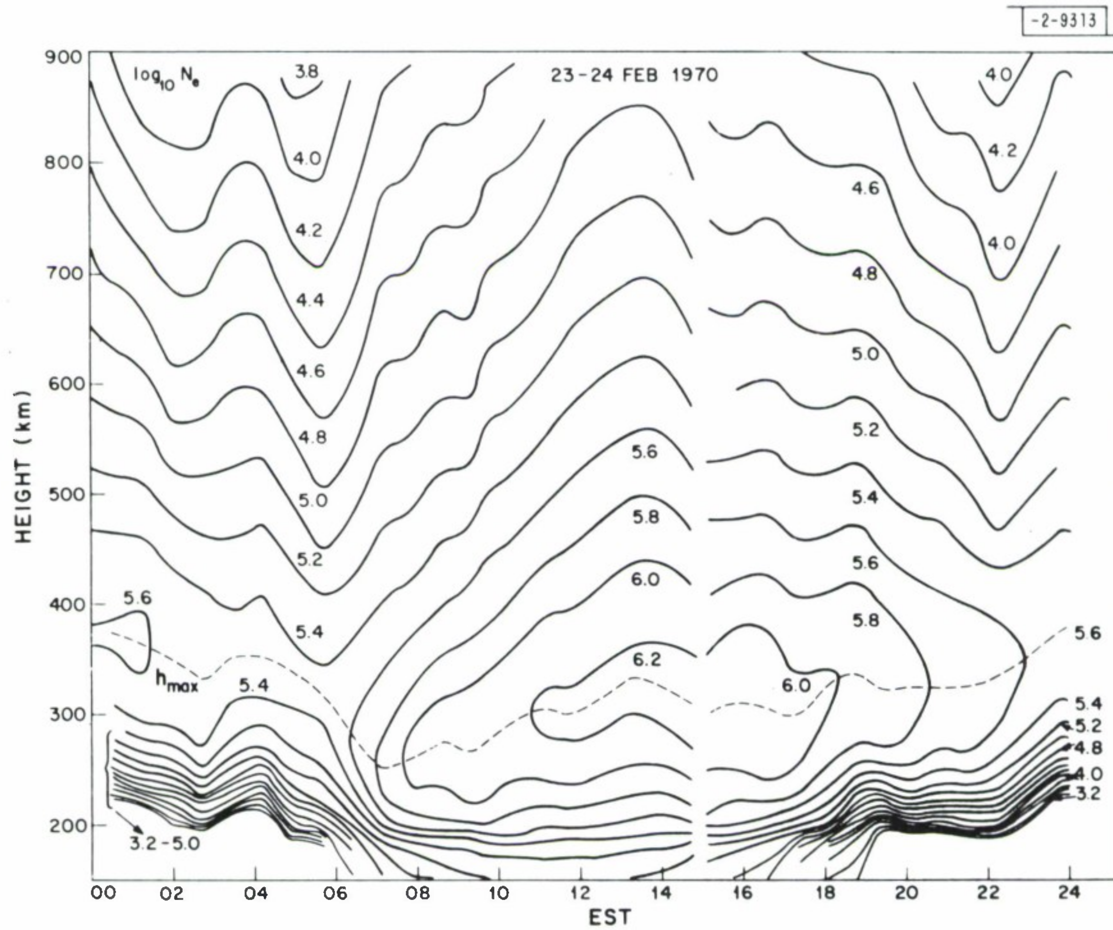

Fig. 41. Contours of constant electron density ($\log_{10}$) observed as a function of height and time for a 24-hour period on 23/24 February 1970. On this day a long period gravity wave (T.I.D.) was present and has given rise to wavelike perturbations in the contours.

minutes or less and hence are not well resolved in measurements requiring 30 minutes to obtain a complete electron density profile. In view of the fear that T.I.D.'s pose the largest source of unpredictable ionospheric refraction, we have developed a special program RASEM(RApid SEquence Mode) for obtaining electron density profiles with good time resolution.

In the rapid sequence mode measurements are made using a single short pulse (100 μsec) employing a frequency hopping scheme that yields an effective pulse repetition frequency of 250 pulses/sec. Coherent receivers are employed and data samples are collected at the output of phase detectors. These are treated in a digital computer to subtract the power associated with noise and possible clutter (i.e. coherent returns). The integration proceeds automatically for a predetermined number of minutes (usually two) at which time the results are written onto a magnetic tape and a new integration period commences. Figure 42 shows a typical electron density profile obtained in this fashion. In Fig. 42 the absolute scale has been obtained by separate measurements of f_oF2 using an ionosonde, and the data over the interval 450-750 km have been replaced by the best fit straight line to smooth out the fluctuations. The effect of the electron-to-ion temperature ratio on the scattered power has been taken into account in these data by employing a model for the variation of this ratio with altitude.

The RASEM data are normally presented as contour plots of constant electron density as a function of height and time. Various amounts of time averaging can be employed by replacing the ith electron density profile (e.g. Figure 42) by a weighted sum of itself and its neighbors before drawing the height contours. A triangular weight function W is employed where

$$W_{i \pm j} = NS + 1 - (i \pm j) \tag{6}$$

in which NS is a number defining the half width of the smoothing interval ($W \geq 0$).

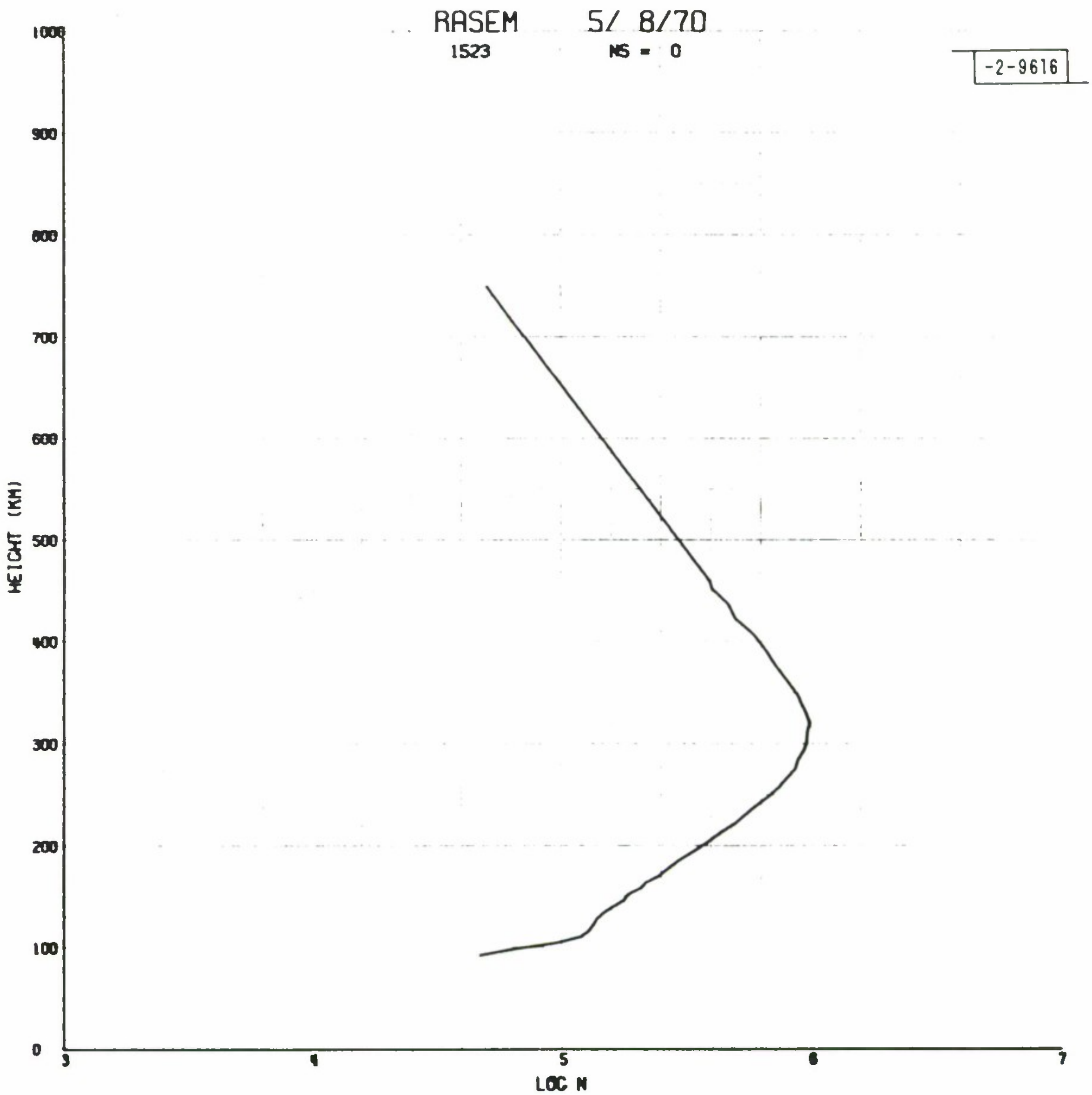

Fig. 42. An electron density profile obtained in 2 minutes using RApid SEquence Mode (RASEM) of incoherent scatter radar.

Figures 43 through 46 show computer drawn contour plots of electron density taken in the manner outlined having various amounts of smoothing applied. In the case NS = 0, each profile is employed independently and the fluctuation visible (Figure 46) is indicative of the repeatability of the measurements. The large fluctuation at all altitudes (1835 GMT) resulted from a transmitter outage. After sunset the measurements become very noisy at low altitudes owing to the very low densities then encountered.

Table 10 summarizes the days on which this type of data has been gathered thus far. These days were chosen for convenience in scheduling other site operations and without regard to likely geomagnetic disturbances. Only on one day (May 28/29) was a T.I.D. clearly observed. This day, shown in Figure 47, followed a geomagnetic storm and displayed anomalously low F2-region densities during the daytime, together with a clearly defined and separate F1 region. Unfortunately, this caused the contour plotting program some difficulty, as at only two altitudes is the density expected to be the same, whereas on this day there were times at which a given density occurred at four separate altitudes. After 1900 GMT, this problem disappeared and very clear wave pattern developed, indicating the propagation overhead of a T.I.D. In order to translate the above time variation into a spatial variation, it is necessary to obtain the velocity of the disturbance. We anticipate that it will be possible to do this from ionosonde records made at Millstone and other stations to the north and south.

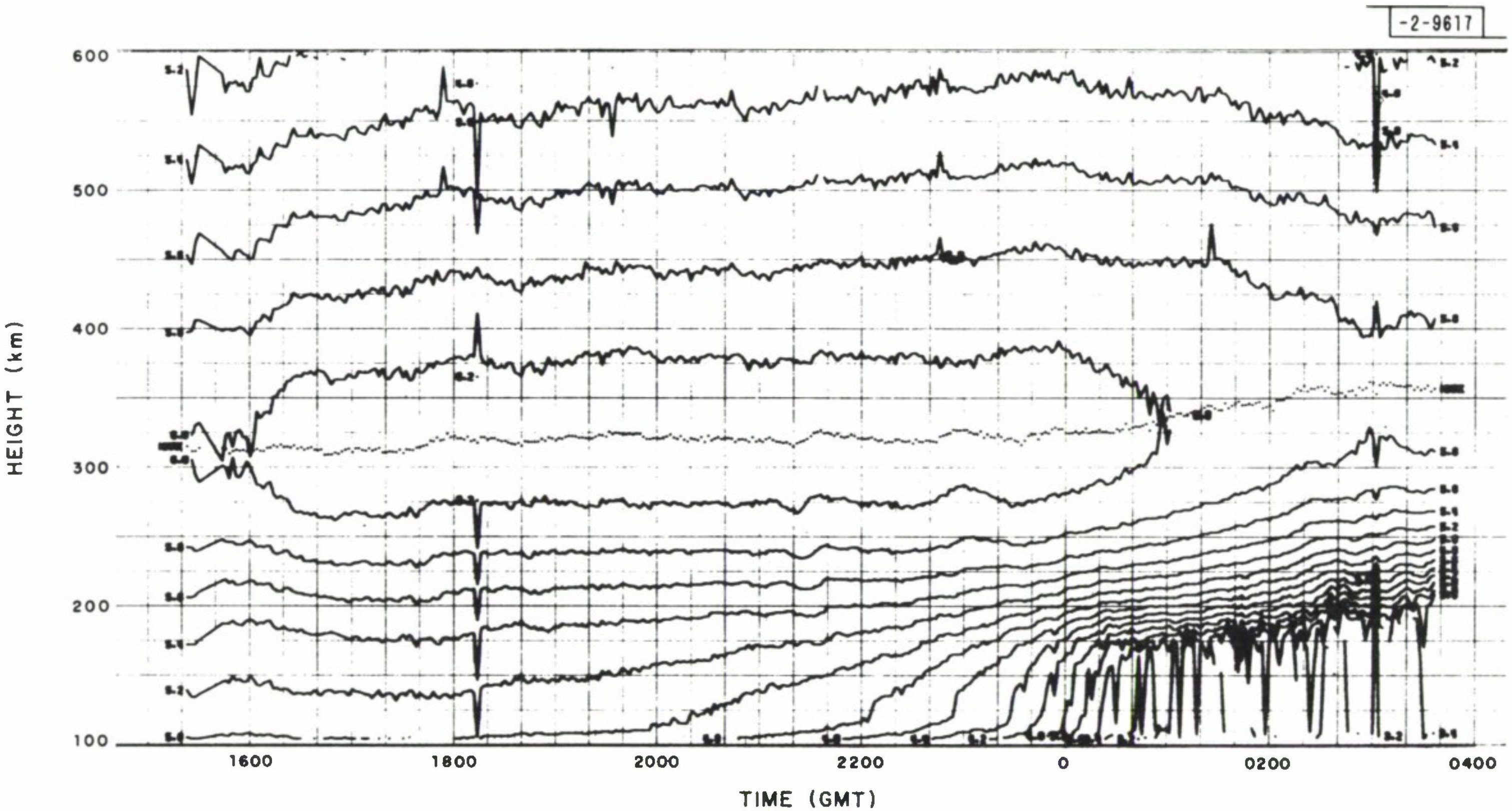

Fig. 43. Computer-drawn contours of constant electron density ($\log_{10}$) as a function of height and time on 8 May 1970. No smoothing has been applied. Break at 1820 resulted from a transmitter outage.

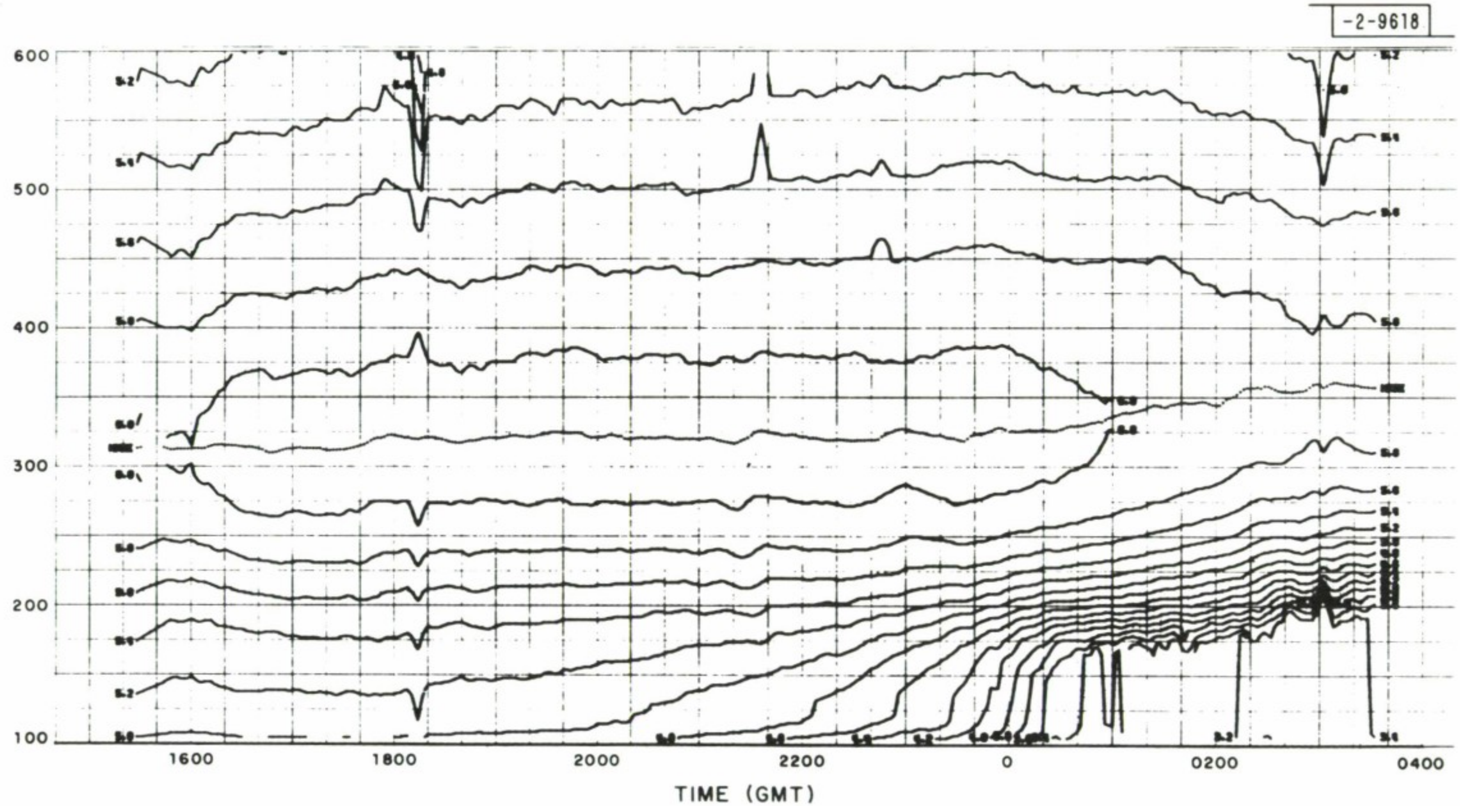

Fig. 44. Running average of data shown in Fig 43; averaging interval = 2 profiles.

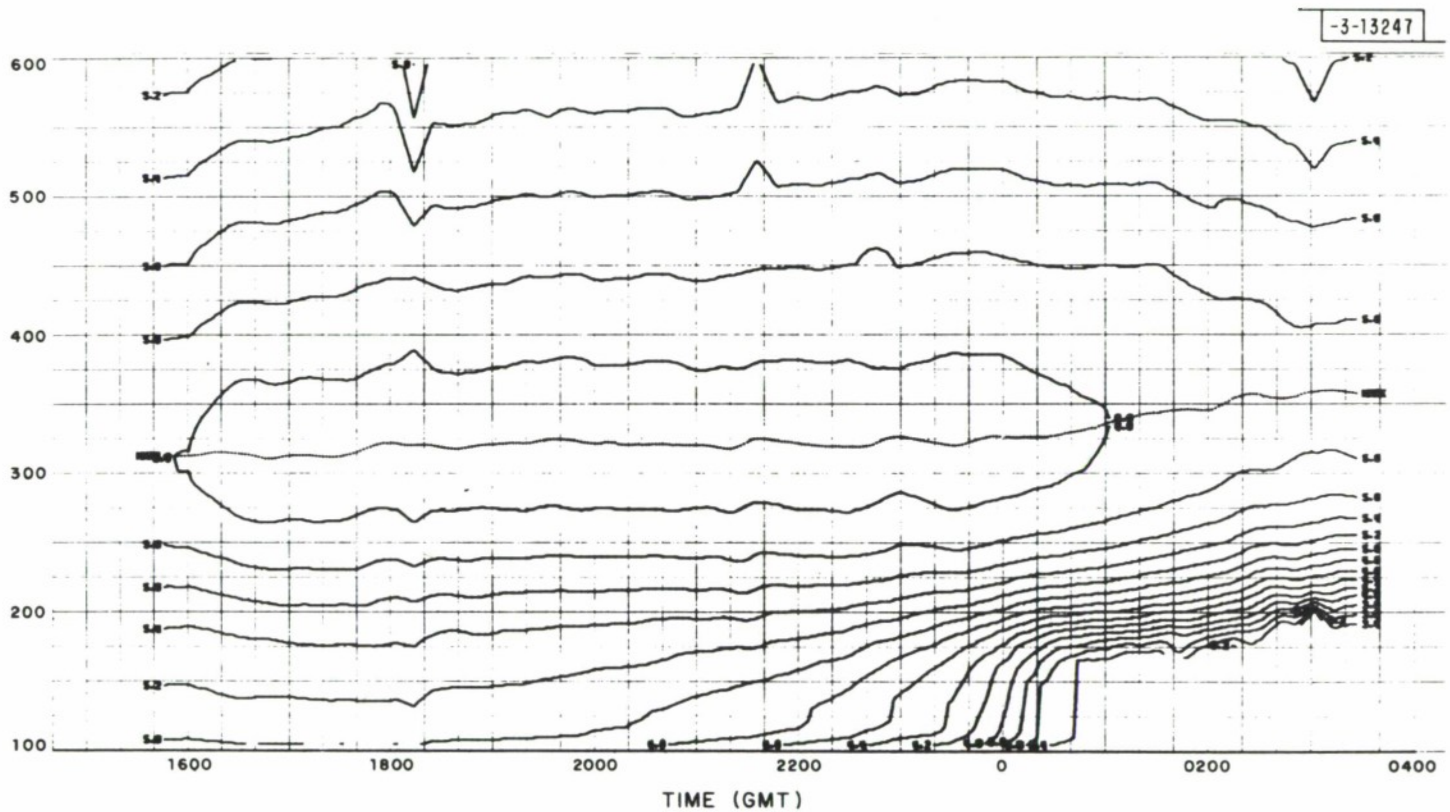

Fig. 45. Running average of data shown in Fig. 44; averaging interval = 5 profiles.

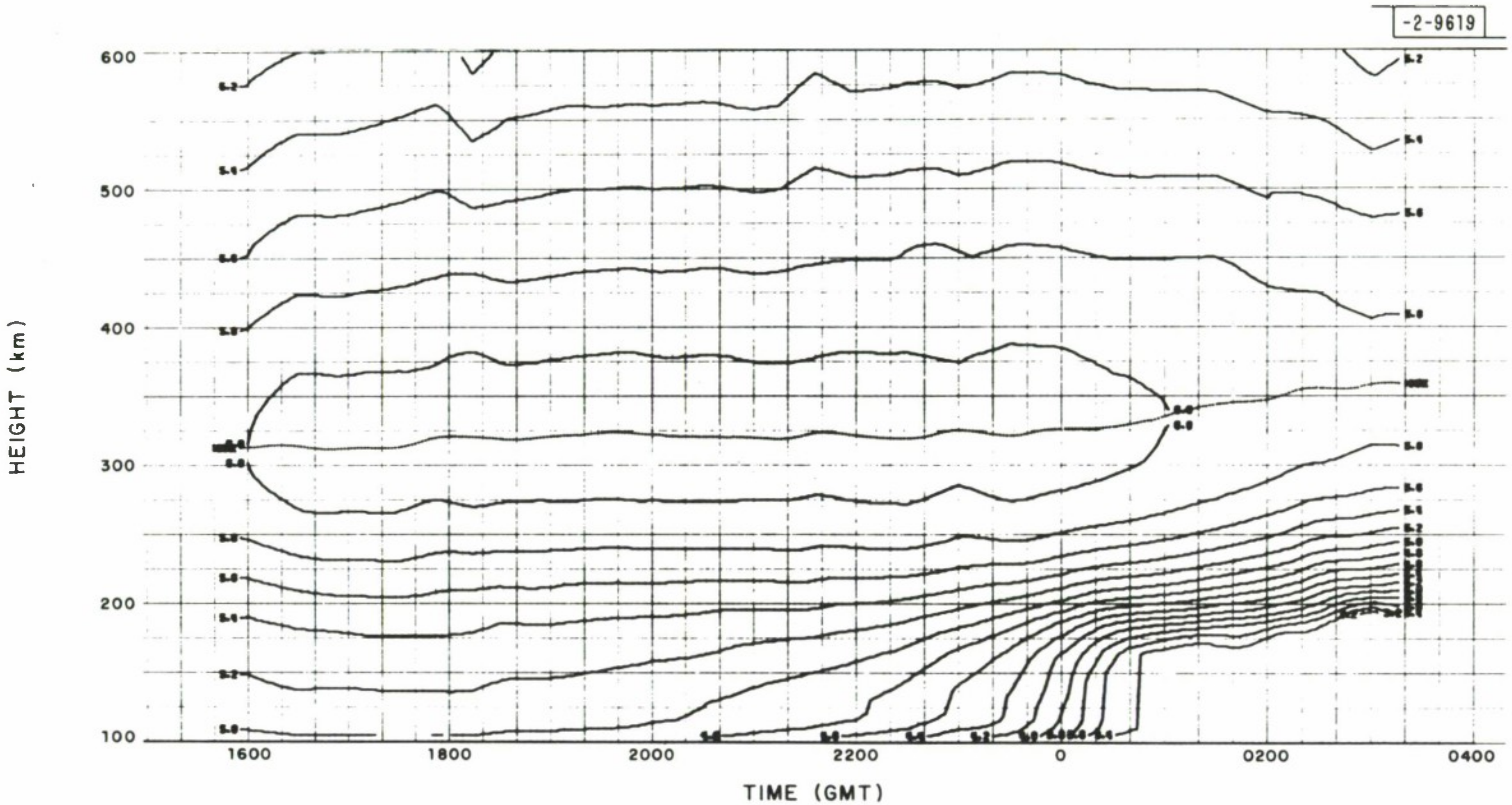

Fig. 46. Running average of data shown in Fig. 44; averaging interval = 10 profiles.

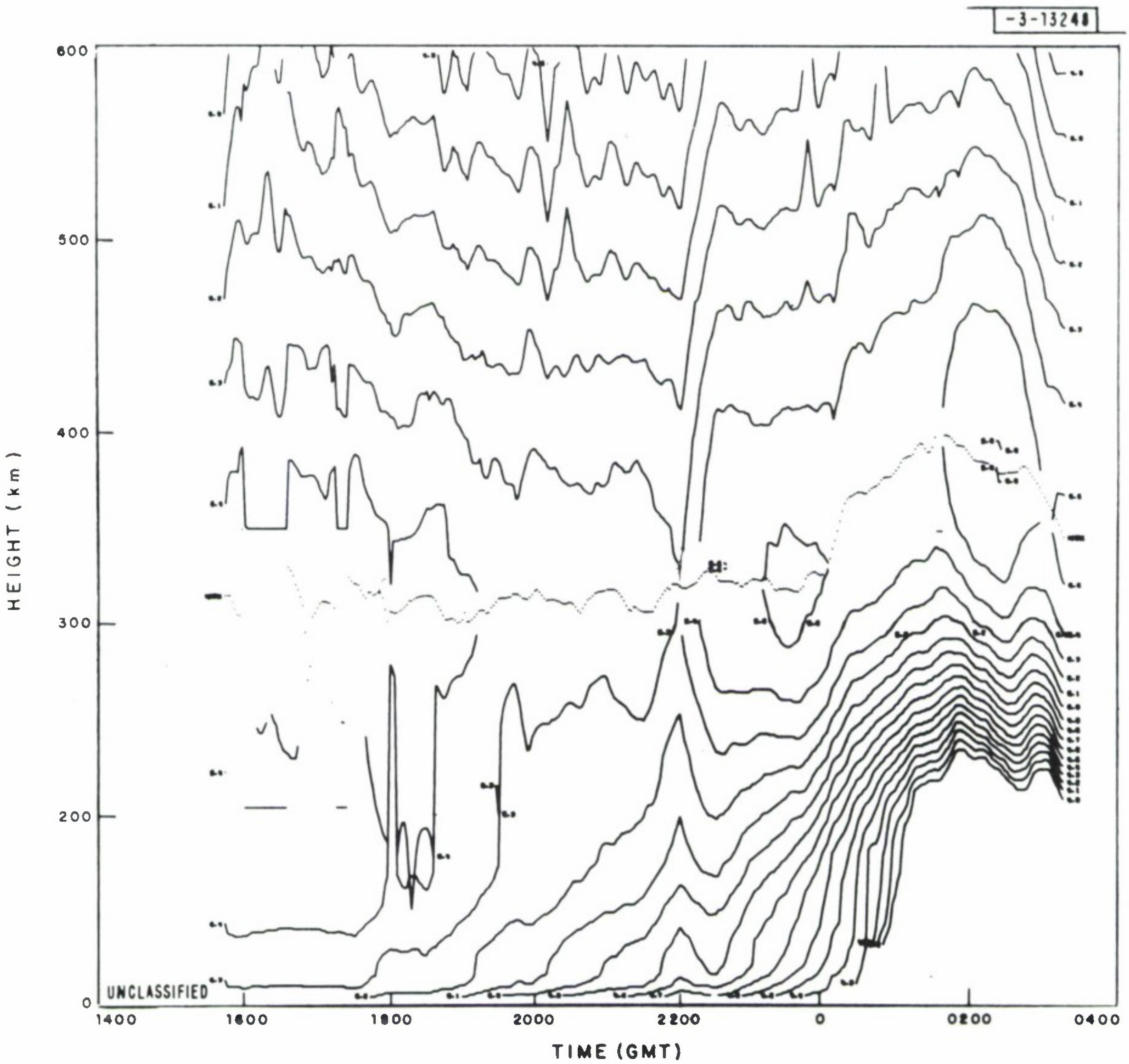

Fig. 47. Contours of constant electron density observed on 26 May 1970 with RASEM program. These data have been smoothed using a running average over 5 profiles (cf. Fig. 45). This day was magnetically disturbed and many T.I.D.'s appear to have been present. A very clear example is seen at low altitudes beginning at 0200 GMT.

Begin		End	
Time (GMT)	Date	Time (GMT)	Date
1411	10 April	2200	10 April
1528	8 May	0332	9 May
1530	15 May	0324	16 May
1700	22 May	0403	23 May
1438	28 May	0322	29 May
1746	26 July	2304	26 July
1346	8 Aug.	0023	9 Aug.
1108	26 Sept.	2334	26 Sept.

Table 10 Dates and Times of RASEM Operations in FY 1970

REFERENCES

Andrews, M. K. and J. O. Thomas, "Electron Density Distribution above the Winter Pole," Nature 221, 223-227 (1969).

Cherkas, V. I., "Ionospheric Perturbations Caused by High-Altitude Thermonuclear Explosions," Kosmicheskie Issledovaniay 7, 429-435 (1969).

Coury, L., "Program Solution to Space Science Problems," AFCRL Report 68-0046. Air Force Cambridge Research Laboratories, Bedford, Mass. (1968)

Cunnold, D. M., "Drift-dissipative Plasma Instability and Equatorial Spread F," J. Geophys. Res. 74, 5709 (1969).

Evans, J. V., "Ionospheric Backscatter Observations at Millstone Hill," Lincoln Laboratory Technical Report 374 (1965).

Evans, J. V., "Millstone Hill Thomson Scatter Results for 1964," Lincoln Laboratory Technical Report 430 (1967).

Evans, J. V., (Editor), "The Millstone Hill Propagation Study Program," Lincoln Laboratory Technical Note 1969-51, September (1969a).

Evans, J. V., "Millstone Hill Thomson Scatter Results for 1965," Lincoln Laboratory Technical Report 474 (1969b).

Evans, J. V., R. F. Julian and W. A. Reid, "Incoherent Scatter Measurements of F Region Density, Temperatures and Vertical Velocity at Millstone Hill," Lincoln Laboratory Technical Report 477 (1970).

Farley, D. T., "A Plasma Instability Resulting in Field-aligned Irregularities in the Ionosphere," J. Geophys. Res. 68, 6083 (1963).

Leadabrand, R. L. and J. C. Hodges, "Correlation of Radar Echoes from the Aurora with Satellite - Measured Auroral Particle Precipitation," J. Geophys. Res. 72, 5311-5317 (1967).

Muldrew, D. B., "F-Layer Ionization Troughs Deduced from Alouette Data", J. Geophys. Res. 70, 2635-2650, (1965).

Rogister, A. and N. D'Angelo, "Type II Irregularities in the Equatorial Electrojet," J. Geophys. Res. 75, 3874-3887 (1970).

Appendix A

The Effect of Phase and Amplitude Error in a Monopulse Feed System

Assume for the sake of the present analysis that the main lobes combined to give the monopulse pattern may be represented by a cosine function:

$$f(\theta) = \cos\frac{\pi}{2}\theta \qquad \text{A.1)}$$

where θ is the normalized angular offset from the center of the beam, i.e. the true angular offset θ' is given by:

$$\theta' = \theta_o \cdot \theta \qquad \text{A.2)}$$

The feed displacement causes the two individual beams combined to give the monopulse response to be displaced to either side of the boresight axis by a normalized angular offset α. The effective monopulse sum and difference responses Σ and Δ may be represented as:

$$\left.\begin{matrix}\Sigma\\ \Delta\end{matrix}\right\} = e^{-\frac{1}{2}(\delta+i\psi)}\cos\frac{\pi}{2}(\theta+\alpha) \pm e^{+\frac{1}{2}(\delta+i\psi)}\cos\frac{\pi}{2}(\theta-\alpha) \qquad \text{A.3)}$$

$$= e^{-\frac{1}{2}(\delta+i\psi)}\cos(+) \pm e^{+\frac{1}{2}(\delta+i\psi)}\cos(-) \qquad \text{A.4)}$$

where

δ = fractional amplitude error

ψ = phase error

In the course of conversion and IF amplification of the Σ and the Δ signals separately a relative phase shift may be introduced. The phase-amplitude processor which determines the monopulse tracking error actually senses the quantity:

$$\mathrm{Re}(\Delta\Sigma^* e^{i\phi}) \qquad \text{A.5)}$$

The nominal boresight direction is assigned to the direction which renders this quantity zero. Carrying out the arithmetic one obtains:

$$\frac{\cos^2\left(\frac{\pi}{2}\,(\theta+\alpha)\right)}{\cos^2\left(\frac{\pi}{2}\,(\theta-\alpha)\right)} = e^{2\delta} + 2e^{\delta} \cdot \sin\psi \cdot \tan\phi \qquad \text{A.6)}$$

If we introduce:

$$y = \tan\frac{\pi}{2}\theta \cdot \tan\frac{\pi}{2}\alpha$$

$$\beta = e^{2\delta} + 2e^{\delta} \sin\psi \cdot \tan\phi$$

The equation for the boresight error becomes:

$$1 - 2y + y^2 = \beta(1 + 2y + y^2) \qquad \text{A.7)}$$

Solving this equation, selecting the valid root and reintroducing the expressions for y and β, assuming θ to be small we obtain:

$$\theta = \frac{\Delta\theta}{\theta_o} = \frac{2}{\pi\cdot\tan\frac{\pi}{2}\alpha} \cdot \frac{\sqrt{e^{2\delta}+2e^{\delta}\sin\psi\tan\phi} - 1}{\sqrt{e^{2\delta}+2e^{\delta}\sin\psi\tan\phi} + 1} \qquad \text{A.8)}$$

For the special case where either the precomparator or the post-comparator phase error is zero and the amplitude error is small one obtains:

$$\theta_A = \frac{\delta}{\pi\cdot\tan\frac{\pi}{2}\alpha} \qquad \text{A.9)}$$

When there is no amplitude error, but phase errors occur and these are assumed to be small, one obtains:

$$\theta_P = \frac{\sin\psi \cdot \tan\phi}{\pi \cdot \tan\frac{\pi}{2}\alpha} \qquad \text{A.10)}$$

In the Millstone UHF system we have $\alpha = 0.68$. Hence we obtain:

$$\Delta\theta = 0.185 \cdot \theta_o \cdot \sin\psi \cdot \tan\phi \qquad \text{A.11)}$$

DOCUMENT CONTROL DATA - R&D

(Security classification of title, body of abstract and indexing annotation must be entered when the overall report is classified)

1. ORIGINATING ACTIVITY *(Corporate author)* Lincoln Laboratory, M.I.T.	2a. REPORT SECURITY CLASSIFICATION Unclassified 2b. GROUP None
3. REPORT TITLE The Millstone Hill Propagation Study: Progress in FY 1970	
4. DESCRIPTIVE NOTES *(Type of report and inclusive dates)* Technical Note	
5. AUTHOR(S) *(Last name, first name, initial)* Evans, J.V.	
6. REPORT DATE 2 December 1970	7a. TOTAL NO. OF PAGES 114 — 7b. NO. OF REFS 13
8a. CONTRACT OR GRANT NO. F 19628-70-C-0230 b. PROJECT NO. 7X263304D215 c. d.	9a. ORIGINATOR'S REPORT NUMBER(S) Technical Note 1970-20 9b. OTHER REPORT NO(S) *(Any other numbers that may be assigned this report)* ESD-TR-70-357
10. AVAILABILITY/LIMITATION NOTICES This document has been approved for public release and sale; its distribution is unlimited.	
11. SUPPLEMENTARY NOTES None	12. SPONSORING MILITARY ACTIVITY Department of the Army

13. ABSTRACT

This report summarizes the work carried out during the period 1 September 1969 through 31 August 1970 as part of the propagation studies being conducted jointly by the Bell Telephone Laboratories and the Lincoln Laboratory for the Advanced Ballistic Missile Defense Agency. These studies are centered on the Millstone Hill Field Station where an 84' fully steerable parabolic reflector is to be employed for simultaneous angle-of-arrival measurements of signals at UHF and L-band. These measurements are expected to permit refraction effects introduced by the auroral regions of the ionosphere to be investigated.

Work to date has largely been concerned with modifying the equipment in order to undertake the observations. A limited number of tracking observations have been carried out which yield useful measurements of angular scintillation. Additional measurements to study the extent and cause of auroral clutter have been undertaken. The Millstone Hill Thomson Scatter radar has also been employed to study F-region irregular behavior assoicated with auroral precipitation and the presence of Traveling Ionospheric Disturbances.

14. KEY WORDS

UHF	ionospheric disturbances	scintillation
L-band	aurorae	auroral clutter
F-region		